CORA Cork Open Research Archive
Cartlann Taighde Oscailte Chorcaí

Title	Evaluation and properties of site-controlled pyramidal quantum dots for quantum information processing
Authors	Ranjbar Jahromi, Iman
Publication date	2023
Original Citation	Ranjbar Jahromi, I. 2023. Evaluation and properties of site-controlled pyramidal quantum dots for quantum information processing. PhD Thesis, University College Cork.
Type of publication	Doctoral thesis
Rights	© 2023, Iman Ranjbar Jahromi. - https://creativecommons.org/licenses/by-nc-nd/4.0/
Download date	2026-11-07 04:56:03
Item downloaded from	https://hdl.handle.net/10468/15964



UCC
University College Cork, Ireland
Coláiste na hOllscoile Corcaigh

Evaluation and Properties of Site-Controlled Pyramidal Quantum Dots for Quantum Information Processing

By

Iman Ranjbar Jahromi

A THESIS SUBMITTED TO
THE NATIONAL UNIVERSITY OF IRELAND, CORK
FOR THE DEGREE OF

DOCTOR OF PHYLOSOPHY



School of Physics
University College Cork
Republic of Ireland

Head of School: Professor Paul Callanan

Supervisor: Dr. Emanuele Pelucchi
Co-supervisor: Professor Paul Townsend

November 2023

Contents

Abstract **vi**

Acknowledgment **viii**

Publications & Presentations **ix**

1 Introduction **1**
1.1 Quantum Information 1
1.2 Single Photon and Entangled Photon Pair Sources 4
1.2.1 Probabilistic Photon Generation 5
1.2.2 On-Demand Photon Generation 8
1.3 QD growth 12
1.4 Physics of QD 17
1.4.1 Excitonic complexes 17
1.4.2 Fine-Structure of the Exciton 18
1.5 Entangled Photon Pairs from QDs 22
1.5.1 FSS and Entanglement 24
1.6 Characterization of QDs 30
1.6.1 Cryogenics Photoluminescence 30
1.6.2 Polarization-Resolved Spectroscopy 32
1.6.3 Time-Resolved Spectroscopy 34
1.7 Summary and Conclusion 37
Bibliography 38

2 InGaAs QDs **47**
2.1 The Anti-Binding Biexciton 47
2.2 Experimetal Conditions 50
2.3 Experimental Results 50

2.3.1 Two Photon Resonant Excitation (TPE) . . . 51
2.3.2 Rabi Oscillations . . . 52
2.3.3 Auto-correlation . . . 54
2.4 Summary and Conclusions . . . 64
Bibliography . . . 66

3 GaAs QDs 71
3.1 The Binding Biexciton . . . 71
3.2 Growth . . . 73
3.2.1 Growth Model . . . 73
3.2.2 Sample Fabrication and Growth Configurations . . . 75
3.3 Experimental Conditions . . . 79
3.4 Experimental Results . . . 80
3.4.1 Spectral Uniformity of Excitonic Complex . . . 80
3.4.2 Fine Structure Splitting Correction . . . 82
3.4.3 Polarization-Entanglement Distribution . . . 85
3.4.4 Two-Photon Resonant Excitation (TPE) . . . 86
3.5 Summary and Conclusions . . . 89
Bibliography . . . 90

4 Tuning QD excitonic states: the case of Iron Doped GaAs QDs and strain tuning 93
4.1 Introduction and Motivation . . . 93
4.2 Theoretical Background . . . 94
4.2.1 Carrier Concentrations . . . 94
4.3 Experimental Results . . . 100
4.3.1 Iron Doped QD TPE . . . 108
4.4 GaAs QDs on Piezo-Crystals: another perspective . . . 108
4.4.1 Experimental Condition . . . 109
4.4.2 FSS correction . . . 109
4.4.3 GaAs QD TPE at Different Charging: preliminary results . 110
4.5 Summary and Conclusions . . . 113
Bibliography . . . 114

5 Summary and Conclusions 117
5.1 Summary . . . 117
5.2 Future Works . . . 119
Bibliography . . . 122

Declaration

This is to certify that the work I am submitting is my own and has not been submitted for another degree, either at University College Cork or elsewhere. All external references and sources are clearly acknowledged and identified within the contents. I have read and understood the regulations of University College Cork concerning plagiarism and intellectual property.

Iman Ranjbar Jahromi
Tyndall National Institute
University College Cork
May 2024

Abstract

Semiconductor quantum dots (QDs) are a promising platform for optical quantum information processing (QIP) due to their unique optoelectronic properties, such as their discrete energy levels and strong light-matter interactions. These properties allow for the manipulation and control of the optical and spin states of individual QDs, making them suitable for applications such as quantum cryptography, quantum computing, and quantum simulation.

One of the key advantages of QDs for QIP is, aside of being embedded in a semiconductor matrix, their small size, which allows for the confinement of carriers within a few nanometers. This results in a discrete energy spectrum and a strong confinement of the carrier wavefunctions, which leads to a strong light-matter interaction. This strong interaction allows for the manipulation of the optical and spin states of individual QDs, enabling the implementation of quantum gates and other quantum operations.

In particular, site-controlled pyramidal QDs have emerged as a promising candidate for optical quantum information processing, due to their unique structural and optical properties. Pyramidal QDs are formed by patterning a semiconductor material into a pyramid shape recesses, which results in a confinement of the electronic and optical states in the inverted pyramid apex. This confinement allows for a high level of control over the electronic and optical properties of the dot, such as the energy level spacing and the optical transition dipole moment. Furthermore, pyramidal QDs (intrinsically) could exhibit a high degree of symmetry, which makes them well suited for implementing various quantum operations.

One of the key advantages of pyramidal QDs is their ability to achieve high

optical quality, which is crucial for implementing high-fidelity quantum operations. In addition, pyramidal QDs can be integrated with other semiconductor technologies, such as waveguides and electro-optic modulators, which allows for the implementation of more complex quantum operations. This integration can be done using various techniques such as epitaxial growth, nano-fabrication and transfer printing or other heterogeneous integration techniques.

Overall, site-controlled pyramidal quantum dots have emerged as a promising candidate for optical quantum information processing, due to their unique structural and optical properties, which allow for high-fidelity quantum operations and the integration with other semiconductor technologies. This research field is still in the early stage and a lot of work is currently ongoing to improve the performance and scalability of pyramidal QD devices.

In this work, we evaluate and optimize some features of this specific type of QDs for optical quantum information processing. One of the main prominent factor/feature, called fine structure splitting (FSS), which is detrimental to the quality of entanglement (essential to quantum information processing), is widely studied and different strategies are discussed to minimize its pernicious effect in the GaAs QD family. Resonant excitation of anti-binding InGaAs QDs, binding GaAs QDs and charge distribution of GaAs QDs sandwiched between super-lattice structure are other topics covered in this work.

Acknowledgment

During these five years at Tyndall National Institute, University College Cork, I had such a great opportunity to meet several great researchers from all over the world in a leading institute bringing cutting edge technologies and facilities from different disciplines under the same roof.

My gratitude to my supervisor Prof. Emanuele Pelucchi, who offered me this PhD, supervised me and taught me without any hesitation, is beyond words. I will always be grateful for his help, advice and interesting discussions not only limited to Physics.

I would like to sincerely thank Dr. Gediminas Juska for his great helping, collaboration and mentoring me during my experiments at the microphotoluminescence lab at the Tyndall National Institute, and also Dr. Agnieska Gocalinska for the growth of almost all of the samples that I used for this work.

I would like to thank Dr. Simone Varo, Dr. John O'Hara, Dr. Stefano Moroni and Francesco Mattana who shared valuable knowledge and experiences with me during the experiments.

I am deeply grateful and filled with appreciation for the unwavering support of my parents and siblings throughout this journey, despite the physical distance that separates us. Their constant encouragement has been invaluable.

I would like to dedicate this thesis to the love of my life, my eternal companion, my dearest friend and my wife, Talie.

Publications & Presentations

Publications

[1] **I. Ranjbar Jahromi**, G. Juska, S. Varo, F. Basso Basset, F. Salusti, R. Trotta, A. Gocalinska, F. Mattana, and E. Pelucchi, "Optical properties and symmetry optimization of spectrally (excitonically) uniform site-controlled gaas pyramidal quantum dots," *Applied Physics Letters*, vol. 118, no. 7, p. 073103, 2021.

[2] G. Juska, **I. Ranjbar Jahromi**, F. Mattana, S. Varo, V. Dimastrodonato, and E. Pelucchi, "Biexciton initialization by two-photon excitation in site-controlled quantum dots: The complexity of the antibinding state case," *Applied Physics Letters*, vol. 117, no. 13, p. 134001, 2020.

[3] F. Mattana, **I. Ranjbar Jahromi**, G. Ronco, M. Rota, F. B. Basset, R. Trotta, E. Pelucchi, and G. Juska, "Gaas site-controlled pyramidal quantum dots as spin qubit sources for a photonic cluster state construction: the role of light-hole-like excited states," in *2023 Conference on Lasers and Electro-Optics (CLEO)*, pp. 1–2, 2023.

[4] H. McAleese, G. Juska, **I. Ranjbar Jahromi**, E. Pelucchi, A. Ferraro, and M. Paternostro, "Distributing entanglement with separable states: assessment of encoding and decoding imperfections," *Quantum Information Processing*, vol. 20, p. 210, Jun 2021.

[5] S. Varo, G. Juska, **I. Ranjbar Jahromi**, S. T. Moroni, A. Gocalinska, and E. Pelucchi, "Engineering site-controlled quantum dots for optical quantum information processing," in *Low-Dimensional Materials and Devices 2019* (N. P. Kobayashi, A. A. Talin, and A. V. Davydov, eds.), vol. 11085, p. 1108507, International Society for Optics and Photonics, SPIE, 2019.

[6] S. Varo, X. Li, G. Juska, **I. Ranjbar Jahromi**, A. M. Gocalinska, A. Di Falco, and E. Pelucchi, "Planar semiconductor membranes with brightness enhanced embedded quantum dots via electron beam induced deposition of 3d nanostructures: Implications for solid state lighting," *ACS Applied Nano Materials*, vol. 3, no. 12, pp. 12401–12407, 2020.

Presentations

[1] **IoP PHOTON Nottingham,UK, 2022**, Title: *GaAs Site-Controlled Pyramidal Quantum Dots: A Spectrally Uniform Source of Single and Entangled Photon Pairs*, **Oral Presentation**

[2] **Quantum Dot Day QDD, Hybrid Conference, UK, 2022**, Title: *GaAs Site Controlled Pyramidal Quantum Dots (QDs): A Spectrally Uniform source of Single photon and Entangled Photon Pairs*, **Poster Presentation**

[3] **EQTC21, Virtual Conference, Ireland, 2021**, Title: *GaAs Site Controlled Pyramidal Quantum Dots (QDs): Towards a Promising Candidate for On-Demand Single and Entangled Photon Source*, **Poster Presentation**

[4] **QD2020, Munich, Germany, 2020**, Title: *Spectral Uniformity and Symmetry of a New Generation of GaAs Site-Controlled Pyramidal QDs*, **Poster Presentation**

[5] **Summer School on Quantum Devices for Non-Classical Light Generation and Maniulation, Erice, Italy, 2019** Title: *Towards Resonant Excitation of Site-Controlled Pyramidal QDs*, **Poster Presentation**

Chapter 1

Introduction

In this chapter, we provide a concise overview of fundamental concepts and terminologies. Our aim is to provide the foundational information/knowledge required to effectively understand the subsequent chapters.

1.1 Quantum Information

Classically, information is carried by "bit" (a contraction of **Binary Digit**), which can be in either of two macroscopic states denoted by 0 and 1 [1]. These elements of classical information (sometimes referred to as Shannon information) are translated into electrical signal in traditional computers. For example, high voltage can represent 1 and low voltage can represent 0. There are other possibilities like two states of a flip-flop, two positions of an electrical switch, two distinct current levels in circuit, etc. In Quantum Information, however, bits are replaced by "Qubits"(a contraction of **Quantum Bit**) and in quantum computers they are translated into two distinct states of a quantum element, e.g., the spin of an electron or the polarization of a photon. Spin up (vertical polarization) corresponds to 1 and spin down (horizontal polarization) refers to 0. More fundamentally speaking, the difference between the classical and quantum information units stems from the

difference between postulates of classical physics and quantum physics. In classical world the states are defined with absolute certainty. The logic state is either in 1 *or* 0. But in contrast to the classical world, quantum physics allows for and actually, in general, implies the superposition of all possible states that a system can take. In the case of binary digits, the two level information carrier system (electron, photon,...) is simultaneously in states 0 *and* 1, or better said, in a superposition of 0 *and* 1 (with specific weighting of each contribution).

In order to express the quantum logic states, we can use the Dirac notation. We denote a state $|\psi\rangle$ as the quantum state of a qubit being in the superposition of states $|0\rangle$ and $|1\rangle$.

$$|\psi\rangle = \alpha\,|0\rangle + \beta\,|1\rangle \tag{1.1}$$

where α and β are imaginary probability amplitudes giving a norm equal to 1.

$$|\alpha|^2 + |\beta|^2 = 1 \tag{1.2}$$

A possible visual representation for a qubit is the Bloch sphere representation. It stems from the possibility of writing [2] the probability amplitudes α and β in the following form:

$$|\psi\rangle = cos\left(\frac{\theta}{2}\right)|0\rangle + sin\left(\frac{\theta}{2}\right)e^{i\varphi}\,|1\rangle \tag{1.3}$$

where θ and φ are specific angles in the Bloch sphere with the simple states $|0\rangle$ and $|1\rangle$ at the poles of the sphere. See Figure 1.1.

In the case of two qubits, the generic basis state for the combined system is given by the tensor product of the basis states of the individual qubits, resulting in a four basis state $|00\rangle, |01\rangle, |10\rangle$ and $|11\rangle$. e.g. $|\psi\rangle = \alpha\,|00\rangle + \beta\,|01\rangle + \gamma\,|10\rangle + \delta\,|11\rangle$. In some specific cases, for qubits A and B, one can write the quantum state as

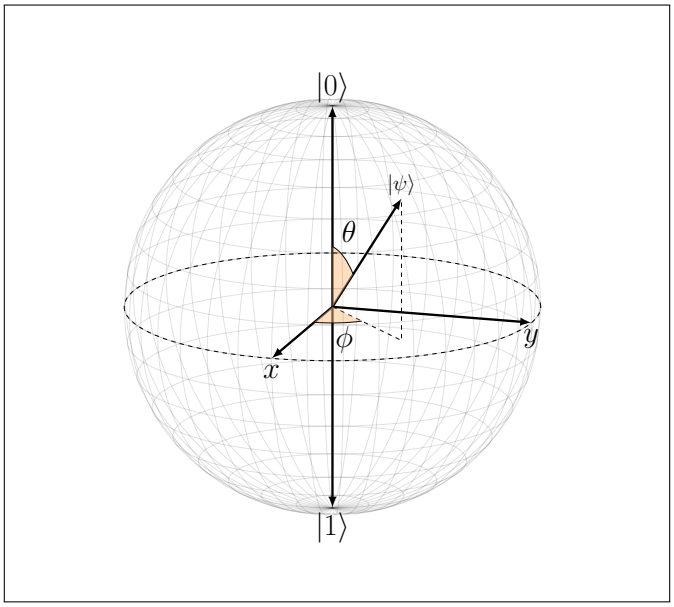


Figure 1.1: Block sphere, a graphical representation of a single state for two-level quantum system.

follows:

$$|\psi\rangle = cos\left(\frac{\theta}{2}\right)|0\rangle_{\mathrm{A}}|1\rangle_{\mathrm{B}} + sin\left(\frac{\theta}{2}\right)e^{i\varphi}|1\rangle_{\mathrm{A}}|0\rangle_{\mathrm{B}} \tag{1.4}$$

or in short

$$|\psi\rangle = cos\left(\frac{\theta}{2}\right)|01\rangle + sin\left(\frac{\theta}{2}\right)e^{i\varphi}|10\rangle \tag{1.5}$$

There is an even more special case in which the probability and phase coefficients are reduced to:

$$|\psi\rangle_{\pm} = \frac{1}{\sqrt{2}}\Big(|01\rangle \pm |10\rangle\Big) \tag{1.6}$$

or in other combination:

$$|\phi\rangle_{\pm} = \frac{1}{\sqrt{2}}\Big(|00\rangle \pm |11\rangle\Big) \tag{1.7}$$

The states in Equation 1.6 and Equation 1.7 are so-called Bell's states after John

Bell provided an experimentally verifiable "path" to entanglement interpretation in his paper "On the Einestein-Podolsky-Rosen Paradox" [3]. Depending on the system being studied, the Bell state will be written in various forms/degrees of freedom. For example for two photons one can have $\frac{1}{\sqrt{2}}\big(|\mathrm{RL}\rangle \pm |\mathrm{LR}\rangle\big)$ or $\frac{1}{\sqrt{2}}\big(|\mathrm{RR}\rangle \pm |\mathrm{LL}\rangle\big)$, R and L being right- and left-handed circular polarization respectively.

We limit ourselves to the photon case and from now on we will consider photons as the carriers of quantum information. There are various sources of photons available. They can either emit single photons (emitting light as single particles and in a discrete time interval in contradiction to thermal or coherent light sources) or entangled photon pairs. In the following we briefly discuss some of these sources.

1.2 Single Photon and Entangled Photon Pair Sources

Ideally, we would require a photon source to emit on demand, with high collection efficiency (bright), high repetition rate (GHz), preferably at room temperature with definite polarization. These sources could be triggered either optically or electrically. We expect high quantum yield (ideally 100%) meaning that each trigger leads to a photon (or entangled photon pair) generation. We also expect that each photon wave-packet should be created identical to the predecessor and successor meaning the spectra, polarization and spatial distribution are identical. This is called indistinguishability and is crucial to photon interference required for quantum information processing [4]. Single photon or entangled photon sources can emit light in a probabilistic (e.g. spontaneous parametric down conversion (SPDC) or four-wave mixing in nonlinear crystals or deterministic (on-demand e.g. in single neutral atoms, single ions, single molecules, semiconductor quantum dots (QDs)) mode [5]. They can operate at room temperatures or cryogenic temperatures.

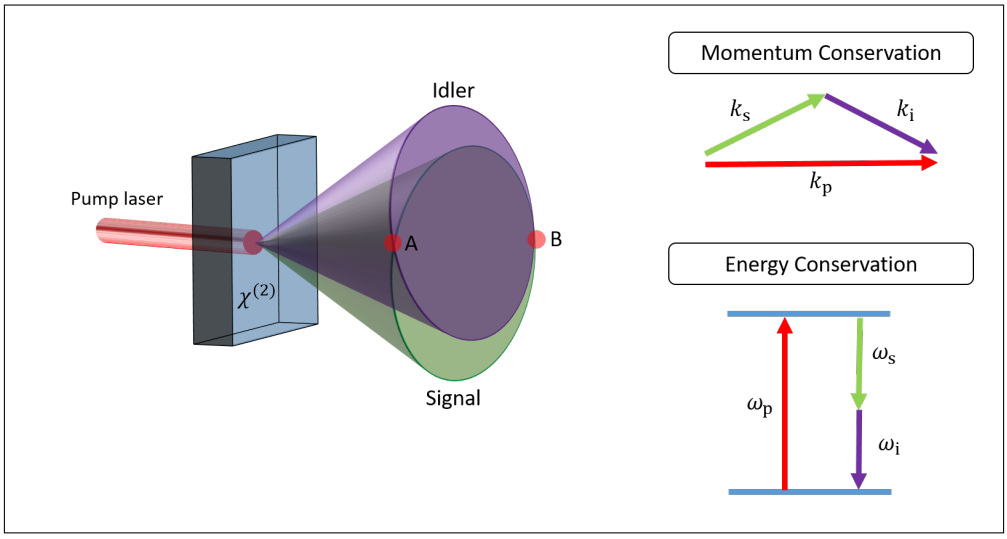


Figure 1.2: SPDC schematics with phase matching condition. This process is a probabilistic photon pair/single photon generation.

There is no photon source gathering all of the above mentioned ideal features simultaneously. Each source has its own pros and cons. We will name a few with a short and essential discussion over their properties.

1.2.1 Probabilistic Photon Generation

Spontaneous Parametric Down Conversion (SPDC)

This process is a probabilistic photon pair/single photon generation. In this process, a photon with higher energy (pump photon) is converted to two photons with lower energy, namely Signal and Idler in accordance with conservation of energy and momentum. In SPDC, a material with a $\chi^{(2)}$ optical nonlinearity is illuminated with a pump laser and two highly directional down converted signal and idler photons are generated. Due to the change of refractive index with respect to frequency (dispersion), only certain triplets of frequencies $(\omega_p, \omega_s, \omega_i)$ with their corresponding momentum (k_p, k_s, k_i) can co-exist, so-called phase matched [6,7], so that the energy and momentum are simultaneously conserved. See Figure 1.2. Phase matching

condition is achieved using birefringent nonlinear materials (refractive index changes by polarization). There are, therefore, different categories of SPDC dependant on the polarization of pump laser, signal and idler [6].

- **Type-0**: Pump, signal and idler share the same polarization.
- **Type-I**: Signal and idler share the same polarization but orthogonal to the pump.
- **Type-II**: Signal and idler have perpendicular polarization.

Referring to Figure 1.2, a type-II SPDC process can be used to produce polarization-entangled photons. These photons are emitted along conical surfaces that intersect in two directions (red highlighted points A and B in Figure 1.2). The energy and momentum conservation laws apply to both the signal (H) and idler (V) photons, so if one is detected along direction A, the other must be detected along direction B and vice versa. This indistinguishability leads to the photons being polarization-entangled. So the state function would be as follows (subscripts A and B in the formula below denote to directions A and B at the intersection of the conic surfaces before discussed):

$$|\psi\rangle = \frac{1}{\sqrt{2}}\Big(|\mathrm{HV}\rangle_{\mathrm{AB}} + e^{i\theta}\,|\mathrm{VH}\rangle_{\mathrm{AB}}\Big) \tag{1.8}$$

Post-Selective Entanglement Generation

The way that one observes these photons, dictates the state to be entangled. In fact, observing the photons at the intersection of signal and idler cones in Figure 1.2 allows the superposition of two orthogonal polarizations. If the the photon pair generation in SPDC process is of type-I, then the signal and idler cones are fully overlapped and have the same polarization. In order to have orthogonal entangled polarization state, one can, for example, perform a so-called post-selective polarization entanglement generation with the help of a rotator and non-polarizing

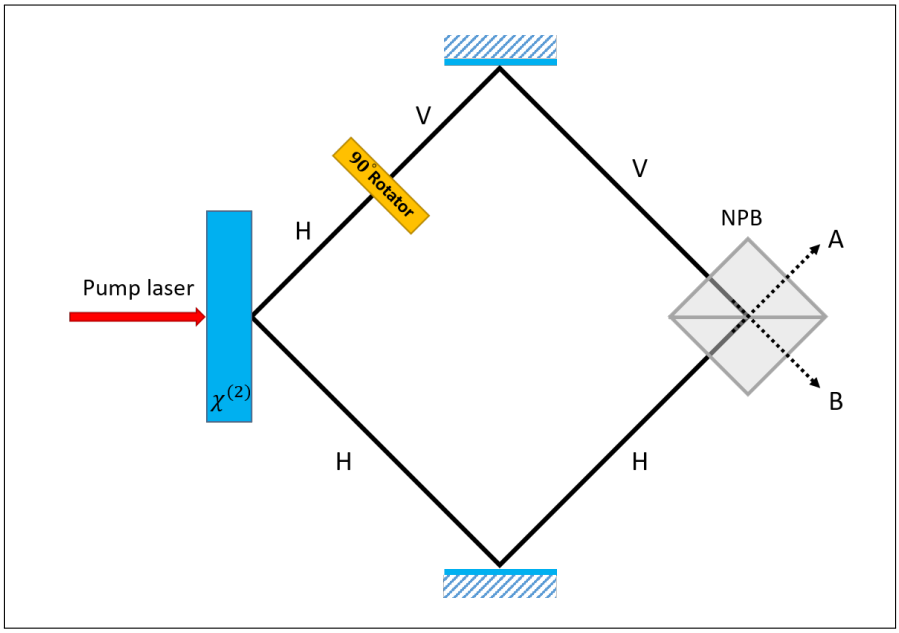


Figure 1.3: Post-selective entanglement generation with type-I photon pair generation

beam splitter (NPB) as depicted in Figure 1.3 [8, 9]. When photons with different polarizations hit the beam splitter, the states afterwards would be $\frac{1}{\sqrt{2}}\left(|\mathrm{H}\rangle_A + i\,|\mathrm{H}\rangle_B\right)$ and $\left(|\mathrm{V}\rangle_A + i\,|\mathrm{V}\rangle_B\right)$, i being the π phase shift due to reflection from the BS. The two photon final state would be a tensor product of the photon sub-states. The eventual state therefor is (here the subscripts A and B denote to output ports A and B of the beam splitter as in Figure 1.3):

$$|\psi\rangle = \frac{1}{\sqrt{2}}\Big(|\mathrm{H_A V_B}\rangle - |\mathrm{V_A H_B}\rangle + i\,|\mathrm{H_A V_A}\rangle + i\,|\mathrm{H_B V_B}\rangle\Big) \tag{1.9}$$

The final state is a product state and can be separated to two states of the composing subsystems (photons), thus they are not entangled. However, with an appropriate *post-selection* procedure it is possible to select detection events that indicate polarization-entangled state. Typically such scheme is realised by selecting photons that only simultaneously are detected at separate output ports A and B.

The two-photon polarization state is then:

$$|\psi\rangle = \frac{1}{\sqrt{2}}\Big(|\mathrm{H_A V_B}\rangle - |\mathrm{V_A H_B}\rangle\Big) \tag{1.10}$$

Good to mention that photons are bosons meaning that their state function should be symmetric. Although equation 1.10 is antisymmetric, the position degree of freedom of the two-photon state is antisymmetric as well as ensuring the overall state function, which is the multiplication of polarization and position degrees of freedom remains symmetric [10]. This is a room temperature process which is advantageous to its counterparts like semiconductor QDs requiring cryogenic temperature. On the other hand, due to its probabilistic nature, the photon generation is not on demand meaning that the photon pair it is not precisely generated when ever required (or also that there is always a non null probability of multiple events).

There are also other probabilistic photon pair generation methods like four-wave mixing in which two pump photons are converted into two correlated photons in a centro-symmetric material such as glass that do not allow $\chi^{(2)}$ nonlinearity but the $\chi^{(3)}$. Although the $\chi^{(3)}$ is small for glass, in optical fibers with long interaction length, experiments have demonstrated creation of correlated photon pairs in a single spatial mode with four-wave mixing in single-mode optical fibers [11–17].

1.2.2 On-Demand Photon Generation

As mentioned above, there are some other sources implementing two- or three-level systems to create an on-demand single photon or an entangled photon pair. In the following we review some of these sources.

Single Neutral Atoms

The first experimental realization of particle entanglement was achieved with single atoms [18–20]. A Calcium atom was used to generate entangled photon pairs. In Aspect et al. work [20] a single atom in a nonlinear two-photon absorption process was selectively excited from its ground state $4s^2\,{}^1S_0$ to the excited state $4p^2\,{}^1S_0$. (Reminder: spectroscopic notation ${}^{2S+1}L_J$ where S is the total spin number of electrons, L is total orbital angular momentum (L = 0, 1, 2, 3,... with corresponding Symbol= S, P, D, F,...) an J is total angular momentum. In this case for both ground and excited states J=0). According to selection rules, J=0↮0 (meaning that a transition from a state with total angular momentum 0 to an other state with total angular momentum 0 is forbidden). The single photon excitation process that is normally not allowed due to selection rules can be achieved through the use of nonlinear excitation with two lasers with different wavelengths (406nm and 581nm). The excited state involves two electrons in a 4p subshell, and is a singlet state with opposite spins, as indicated by the term symbol ${}^1S_0$. This means that the same energy level is occupied by two electrons that have opposite spins, but are otherwise indistinguishable. This is an indistinguishable two-body system suggesting entangled spin states. With the very same logic of J=0↮0, the excited state $4p^2\,{}^1S_0$ can not decay to $4s^2\,{}^1S_0$ as emission of a single photon requires change in angular momenta of ±1. The relaxation, however, can take place through an intermediate state $4s^1 4p^1\,{}^1P_1$ (J=1) by emitting two consecutive photons having the total angular momenta equal to 0 (conservation of momentum). If the photons are emitted along the quantization axis (e.g. z), two degenerate states with magnetic quantum numbers m = +1 and m = -1 exist (see Figure 1.4). The polarization of photons could be determined based on the constriction of the total angular momentum of photons emitted in the recombination cascade: the first circularly polarized (either left- or right-hand) photon is followed by a photon of the same

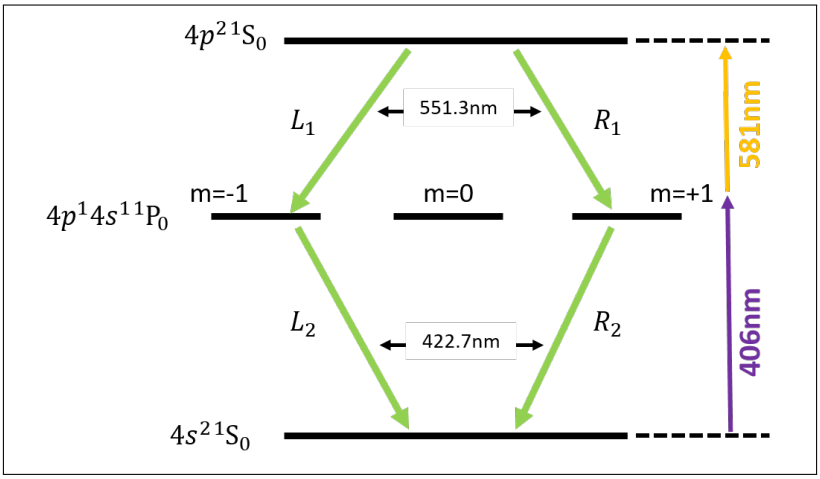


Figure 1.4: Polarization-entangled photon emission from a single atom via recombination cascade

polarization, provided that their emission direction is opposite (to maintain J=0). In summary the scenario is as follows. The two-electron spin states are entangled. The first photon is emitted via the decay to the intermediate state. Photon and atom stay entangled until the second electron is decayed to the ground state. The entanglement is then fully transferred to the polarization state of photons. The entangled states is:

$$|\psi\rangle = \frac{1}{\sqrt{2}}\Big(|\mathrm{R_1R_2}\rangle + |\mathrm{L_1L_2}\rangle\Big) \tag{1.11}$$

Realization of such a system with alkali atoms such as Cs and Rb have been demonstrated as well [21–26]. There are other systems like Single Molecules [27, 28] and Single Ions (which recently became of a great interest) [29–33] that are used to generate single and entangled photon pairs.

Color Centers

A nitrogen-vacancy (NV) color center is a point defect in the diamond lattice. It consists the nearest-neighbour pair of nitrogen atom which substitutes for a carbon

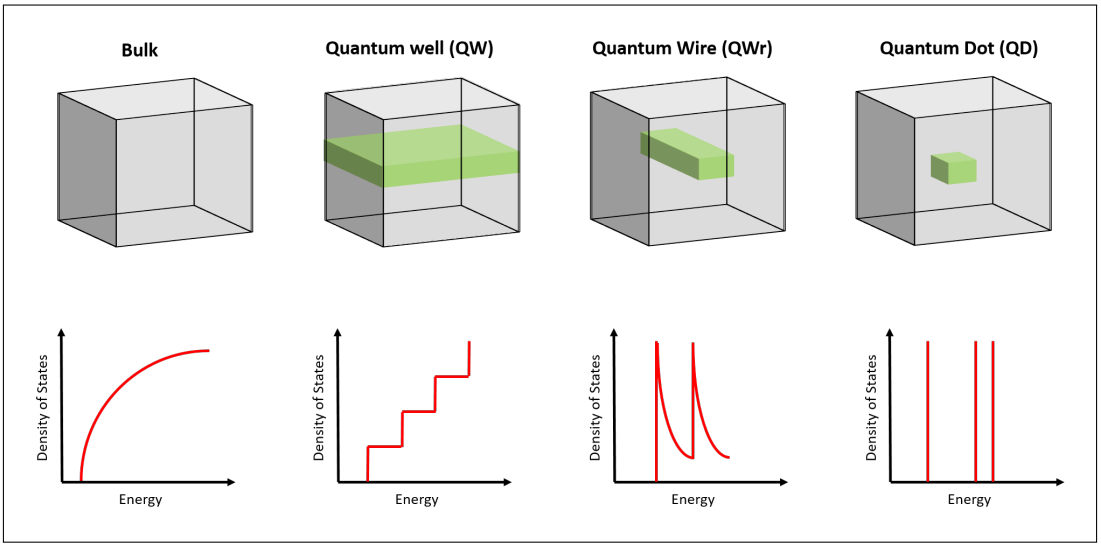


Figure 1.5: Energy of an electron in different confinements. From left to right: In bulk material, quantum well, quantum wire and quantum dot respectively.

atom and a lattice vacancy [34, 35]. The optical transition of NV centers can be modeled by a three-level energy system. The ground state is denoted as $|g\rangle$ and excited state as $|e\rangle$, where $|e\rangle$ is also thermally coupled to a meta stable state called $|s\rangle$ [5]. The excited state $|e\rangle$ can decay to the ground state $|g\rangle$ and emit a single photon. Thermally coupling between the meta stable $|s\rangle$ and $|e\rangle$ is also possible. This state is usually referred to as a "shelving" state, because while in that state, the $|e\rangle$ to $|g\rangle$ emission terminates. The long lifetime of this shelving state $|s\rangle$ results in a decrease in the single-photon emission rate and also causes photon bunching when looking at time intervals longer than the color center's main transition lifetime. For the nitrogen-vacancy center the emission line is at 637nm with a spectrum broader than 100nm.

Semiconductor Quantum Dots (QDs)

Before jumping into QDs as single photon sources, it is good to address a small summary of quantum confinement types. When the electron (or electron-hole pair

as a quasi-particle) is confined in a potential with dimensions near the De Broglie wavelength of the electron (for an electron with KE = 1eV and rest mass energy 0.511MeV, the associated De Broglie wavelength is 1.23nm), the energy profile that an electron can occupy contains discrete levels rather than a continuum of levels as for electron in free space or bulk material (and e.g. effective masses are not the same as the free electron mass). This confinement could be in one, two or three dimension. See Figure 1.5.

- **1D confinement**: A Quantum Well (QW) in which the electron is free to move in a 2D plane.
- **2D confinement**: A Quantum Wire (QWr) in which the electron is free to move in 1 dimension only.
- **3D confinement**: A Quantum Dot (QD) in which the energy of the electron or electron-hole is discrete in all three dimensions. QDs are referred as artificial atoms.

In the case of semiconductors, one can sandwich a lower bandgap material like GaAs between a higher bandgap material like AlGaAs. The geometry of this confinement could tell what structure (QW, QWr or QD) we are looking at. For QDs, there are different methods to create such a confinement. But before we start discussing the QD growth, we first review the physics of QDs and challenges arising with this semiconductor structure.

1.3 QD growth

The emergence of "small" semiconductor confined structures has generated significant interest due to their unique physical properties and potential applications. This interest was closely linked to the technological advancements that made it

possible to actually construct such structures [36]. The concept of discrete energy levels in confined structures was well-established in quantum mechanics, but it wasn't until the 1960s and 1970s that there was significant literature on the importance of quantum confinement generally referred as *quantum size effects* (QSE) in applications. One notable result was the invention of the quantum well (QW) laser [37–40]. However, specific quantum-mechanical problems still needed to be addressed in the 1970s, such as the simple harmonic oscillator confined in a box [41].

It is worth noting that even though one-dimensional confined structures were quickly labeled as quantum wells, it took until the 1990s for there to be an agreed-upon labeling system for lower dimensionality structures. The development of applications for confined structures was made possible by relevant advances in semiconductor technologies. Molecular beam epitaxy (MBE) and metalorganic vapour phase epitaxy (coming with different names such as MOVPE, MOCVD, OMVPE, OMCVD, CVD) were consecrated during the 1970s and became available to research groups as industrial products during the early 1980s [42–47]. These techniques replaced less versatile "growth" techniques. The invention of the atomic force microscope (AFM) [48], following the Scanning Tunneling microscope (STM), was not industrially available to several research groups until the early 1990s. Early publications in the field relied mainly on electron microscopy in the form of Tunneling Electron Microscopy (TEM) and Scanning Elecotron Microscopy (SEM) for structural feedback, along with in-situ diffraction techniques such as low energy electron diffraction (LEED).

Furthermore, recent advances in "quantum light" were made possible by the broader availability of more advanced and cost-effective laser sources, such as the (mode-locked) Ti-Sapphire laser in the late 1980s and early 1990s, and more recently, significantly improved single-photon detectors based on various technologies. Therefore, it is important to note that technological advancements in both semiconductor

growth techniques and microscopy/characterization tools have played a critical role in the development of applications for confined structures.

The 1982 manuscript by Arakawa et al [49] is considered a significant paper for the development of quantum dot technologies. It provided a theoretical analysis that proposed the use of quantum dot lasers for more efficient and temperature-stable laser structures. At the time, obtaining such structures with semiconductors was not possible in a controllable way. However, self-assembled processes used to create quantum dot structures result in a distribution of sizes that limit their maximum performance. The choice of terminology used in the manuscript is also worth noting. Quantum dot structures are referred to as "*3D-QW*" rather than zero-dimensional (0D) structures, indicating that there was no agreement on how to label nano-structures in 1982. During the 1980s and early 1990s, other notations, such as QW wires and boxes, were also used. These notations later evolved into quantum islands, boxes, dots, and the contemporary approach.

The above mentioned nano-structures can come in many different forms, for example by top-down lithographic approaches. The development of nano-structures began in the early 1980s through both top-down and bottom-up approaches. The scientific community initially focused on top-down approaches, such as patterning semiconductors, to achieve low-dimensional structures in the micron or nanometer range. However, researchers seeking optical effects quickly realized that these methods could result in distributed defects that affected the optical properties, uniformity, and control of the structures [50–58]. This led to a shift towards bottom-up "self-assembled" structures, which showed greater promise and had already been explored in the early 1980s.

It is worth noting that self-assembled structures were sometimes discovered by chance, such as the case with quantum dots. Quantum dots were initially discovered as a byproduct of the research on heteroepitaxy, and their unique optical

properties were quickly recognized. Although the formation of quantum dots comes with a distribution of sizes due to the self-assembly process, they offer a better temperature response and have become a commercial reality.

Stranski-Krastanov

The concept of semiconductor self-assembly is not a new one, as surface scientists have been exploring the growth processes of deposited monolayers (MLs) of material A on crystalline material B since the 1960s. This research initially focused on metal on metal and metals on semiconductors, and later expanded to include more exotic compounds. The interpretation of this research often relied on photoemission spectroscopy and interference technologies, such as LEED.

The growth modes of epitaxial growth were discussed in a theoretical classification as early as 1958 [59, 60] This classification identified three different growth mechanisms, including growth atom-layer by atom-layer through surface nucleation (FRANK-VAN DER MERWE mechanism) for growth on material of the same composition, and the growth on a different material occurring through the original formation of a mono- or poly-molecular layer without nucleation, which then leads to the formation of three-dimensional nuclei (STRANSKI-KRASTANOV mechanism), or through the formation of three-dimensional nuclei directly on the foreign substrate (VOLMER-WEBER mechanism).

Some of the original manuscript discussing the growth modes was mostly written in German and appeared as early as in the 1920s and 1930s. Initially, the classification did not have widespread use, but by the early 1970s, it was commonly utilized by the growing surface science community. By the late 1970s, it had become the dominant description used in publications.

The Stranski-Krastanov (SK) classification is particularly interesting as it is almost exclusively used in relation to quantum dots today. Volmer-Weber quantum

dots are possible, but the success story of quantum dots is primarily linked to SK dots. The original SK growth mode description deviates significantly from the current utilization. The original proposal related to a layer by layer growth which would then turn 3D due to impurities or dislocations, forming islands as a form of energy minimization. The breach of crystal perfection was nearly intrinsic to the original description.

Currently, a few-layer growth followed by 3D growth is labeled as SK, regardless of the specific driving mechanism. It is important to note that defect-induced 3D nucleation is today not generally described as a Stranski-Krastanov process, unless it is useful for future developments. Today, 3D formation in semiconductor quantum dots is mainly associated with a specific energy minimization mechanism. The increase in surface energy of the system is outweighed by the reduction in strain energy due to lateral relaxation during 3D growth.

In summary, the growth modes of epitaxial growth have been studied by surface scientists for many years. The theoretical classification from the late 1950s is still widely used today. The Stranski-Krastanov classification is interesting because it is primarily associated with quantum dots. The current usage of SK nomenclature primarily relates to a specific energy minimization mechanism, which reduces strain energy during 3D growth.

Droplet Epitaxy

Droplet epitaxy (DE) [61] is an other method used to grow QDs by depositing group III elements (such as Ga, In, or Al) onto a substrate at a temperature above their melting point. This causes the elements to segregate into droplets of nanometer-sized dimensions. The droplets are then exposed to a flux of group V elements, leading to the crystallization of the droplets into III-V QDs. This growth method can be used to produce both strain-free QDs (such as GaAs/AlGaAs) and

strained QDs (such as InAs/GaAs).

Local Droplet Etch Epitaxy

Defects can have subtle effects on the properties of QDs, such as causing the spectral diffusion of QD exciton states [62], which is detrimental to quantum applications. These effects are typically more pronounced in DE QDs compared to "strain-induced" SK QDs. However, a recent development called local droplet etching (LDE) [61,63] has been successful in overcoming this limitation in DE QDs.

1.4 Physics of QD

So far, we have reviewed some candidates of single photon and entangled photon pairs. We leave more details regarding the epitaxial growth, features appearing and the general structure of QDs for now and we'll come back to it later. We first review the general physics behind QDs, which is not dependent on the way they are grown or their specific structure. As mentioned above, QDs are often called "artificial atoms" because they have properties similar to those of individual atoms (discrete energy levels) and they exhibit similar optical effects. Therefore, it could be expected that the basic concept of generating polarization-entangled photons with quantum dots is similar to the approach used with single atoms [64]. The specific details of generating entangled photons with quantum dots, along with a general introduction to these structures, will be discussed in more detail later on.

1.4.1 Excitonic complexes

An exciton is a pair consisting of an electron and a hole that are attracted to each other by the Coulomb force [65]. An other important factor for this binding between electron and hole is strong confinement when 3D confined structures are

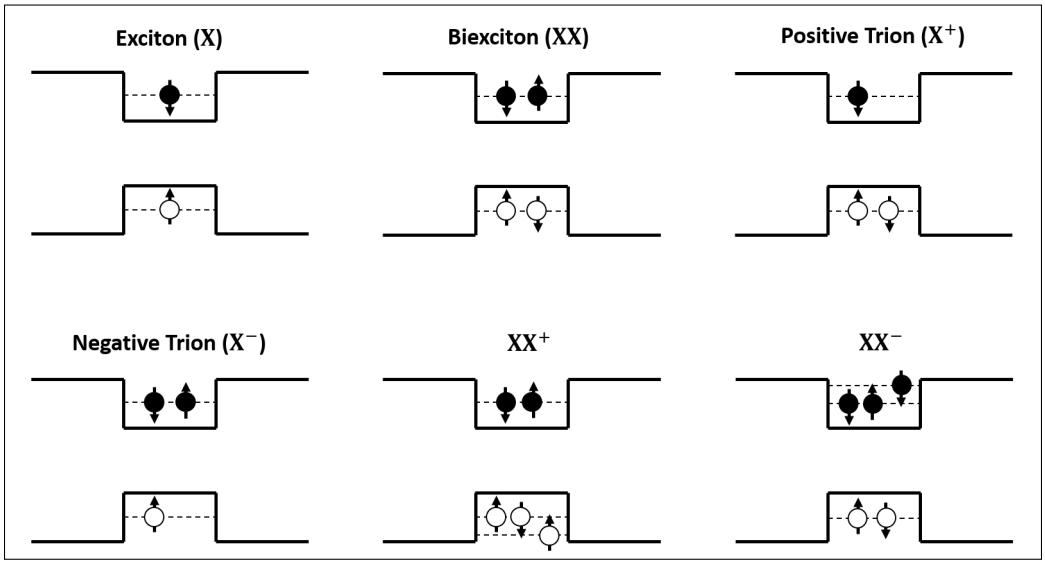


Figure 1.6: Name and structure of different excitonic complexes forming inside the QD.

considered. These quasi-particles could be generated from the vicinity of the QD and injected into it or could be directly generated inside the QD. If there are multiple electrons or holes, various excitonic complexes may form. Figure 1.6 shows the name and structure of few excitonic complexes. Ideally, a QD is excited from its ground state to the excited state, then spontaneously decays to the ground state (electron and hole recombine) and emits a single photon. Then the system could be reinitialized to the excited state and the process repeats. This ensures the single photon emission. Statistically speaking, photons are emitted with a sub-Poissonian distribution at variance to coherent laser light with a Poissonian, or thermal light with a super-Poissonian distribution [66]. If two electrons recombine with holes consecutively, we would have a *recombination cascade*.

1.4.2 Fine-Structure of the Exciton

Each of the excitonic energy levels is made up of a group of states corresponding to different spin configurations of the carriers. This multiplet exhibits a fine

structure splitting that is caused by two factors. **I.** The "exchange interaction" which couples the spins of electron and hole. **II.** The Zeeman interaction routing from an interaction with an external or internal magnetic field. We limit our study to the case of exchange interaction. In its general form, the exchange energy has the following integral form [67]:

$$\mathcal{H}_{exchange} \propto \iint \frac{\mathbf{\Psi}_{\mathrm{X}}^{*}(\mathbf{r_e}=\mathbf{r_1},\mathbf{r_h}=\mathbf{r_2}) \times \mathbf{\Psi}_{\mathrm{X}}(\mathbf{r_e}=\mathbf{r_2},\mathbf{r_h}=\mathbf{r_1})}{|\mathbf{r_1}-\mathbf{r_2}|}\, d^3r_1 d^3r_2 \tag{1.12}$$

where $\mathbf{\Psi}_X$ is the exciton wave function with $\mathbf{r_{e,h}}$ being the electron and hole coordinates respectively. When calculating the exchange, the integral separates into two parts in real space called short- and long-ranged. The short-ranged is when e-h pair are in the same Wigner-Seitz unit cell and long-ranged is when each falls into a separate cell (a Wigner–Seitz cell is an example of a primitive cell, which is a unit cell containing exactly one lattice point). Here, we focus on the short-ranged interaction. The full picture should also consider the long-ranged and interaction of carrier spins with the spins of the lattice nuclei known as Overhauser shift of the exciton energy [68]. In the short-ranged regime, the general form of e-h spin interaction with the electron spin S_e and hole spin J_h is [69]:

$$\mathcal{H}_{exchange} = -\sum_{i=x,y,z} \left(a_i J_{h,i} S_{e,i} + b_i J_{h,i}^3 S_{e,i}\right) \tag{1.13}$$

where a_i and b_i are spin-spin coupling constants. As we will later see, our QDs are self-assembled QDs ensuring the heavy and light hole energies are well separated by orders of meV's due to the existing strain. This splitting is considerably larger than the fine-structure interaction energies and can be safely neglected. The heavy-hole spin is therefore $J_h = 3/2$, $J_{h,z} = \pm 3/2$ and the electron spin is $S_e = 1/2$, $S_{e,z} = \pm 1/2$. Given this, there could be 4 possible spin configurations.

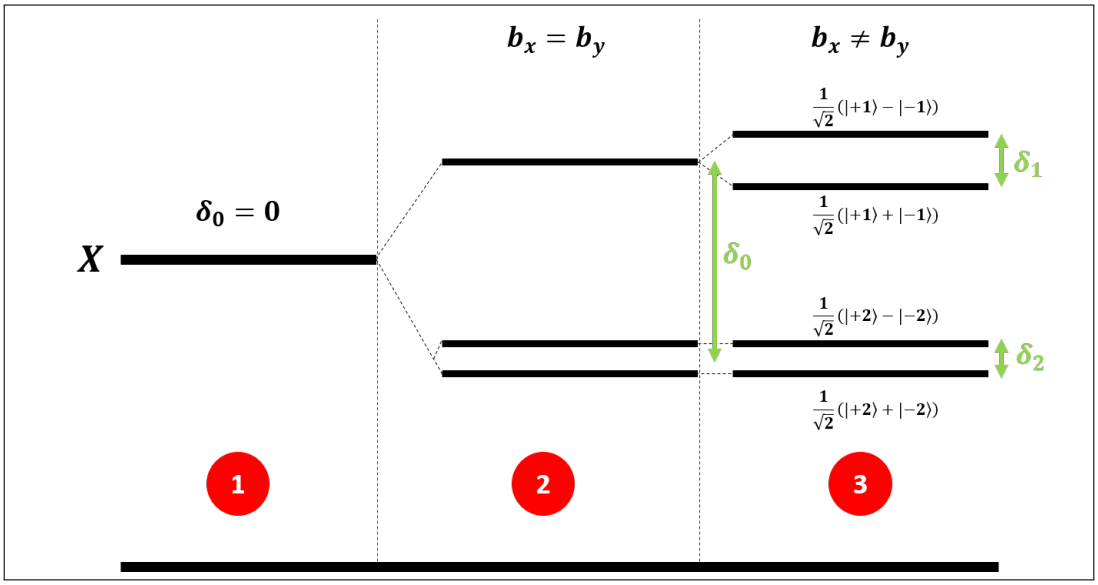


Figure 1.7: The schematics of "standard" exciton fine structure. The panel 1 shows neglecting the heavy and light hole splitting. Panel 2 showing the presence of splitting of heavy and light holes due to strain in self-assembled QDs. And panel 3 indicating the presence of fine structure splitting.

We summarize these spin configurations/states as $M = J_{h,z} + S_{e,z}$. If we omit the exchange interaction and adopt a simple picture, these states are four fold degenerate. Otherwise we would label each state by their spin configuration as $|+1\rangle$, $|-1\rangle$, $|+2\rangle$ and $|-2\rangle$ respectively. By writing the exchange interaction Hamiltonian 1.13 on the basis of these states, the matrix representation would be:

$$\mathcal{H}_{exchange} = \begin{pmatrix} +\delta_0 & +\delta_1 & 0 & 0 \\ +\delta_1 & +\delta_0 & 0 & 0 \\ 0 & 0 & -\delta_0 & +\delta_2 \\ 0 & 0 & +\delta_2 & -\delta_0 \end{pmatrix} \tag{1.14}$$

The following abbreviations have been introduced: $\delta_0 = 1.5(a_z + 2.25b_z)$, $\delta_1 = 0.75(b_x - b_y)$ and $\delta_2 = 0.75(b_x + b_y)$. The first term in equation 1.13 gives the diagonal elements of the matrix and the second term leads to off-diagonal elements.

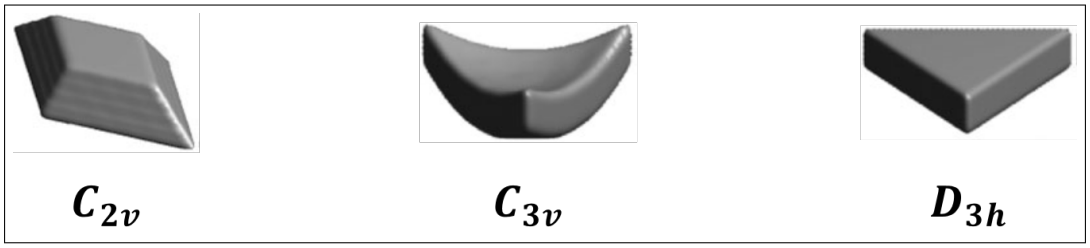


Figure 1.8: Different symmetries of QDs. C_{2v} (C_{3v}) symmetry has a two-fold (three-fold) rotation axis and two (three) vertical mirror planes containing the rotation axis. D_{3h} symmetry has a three-fold rotation axis, 3 two-fold rotation axes perpendicular to the first rotation axis and a horizontal mirror plane.The figure is taken from M. A. Dupertuis et al., Phys. Rev. Lett. 107, 127403 (2011).

As the matrix 1.14 has a block diagram form, the bright and dark excitons do not mix with each other and they are separated by the value of δ_0. In general and in realistic systems, due to the presence of off-diagonal matrix elements in the relevant subblocks, the excitons with each $|\mathrm{M}| = 1$ and $|\mathrm{M}| = 2$ are hybridized. It means that heavy holes and light holes states are actually mixed i.e. can be written as superposition of different bases which contain both, and not separated. Rotational symmetry implies $b_x = b_y$ so the states $|+1\rangle$ and $|-1\rangle$ are eigenstates of the exchange interaction. If the rotational symmetry is broken ($b_x \neq b_y$), then $\delta_0 \neq 0$ so the states $|+1\rangle$ and $|-1\rangle$ are mixed. The eigenstates are $\frac{1}{\sqrt{2}}\big(|+1\rangle \pm |-1\rangle\big)$ separated by δ_1. Dark excitons are always mixed ($\delta_2 \neq 0$) regardless of rotational symmetry. The eigenstates are $\frac{1}{\sqrt{2}}\big(|+2\rangle \pm |-2\rangle\big)$ which are separated by δ_2 with the relative energy of $\frac{1}{\sqrt{2}}(-\delta_0 \pm \delta_2)$. See Figure 1.7.

When a QD is completely asymmetric, the previous explanation is not applicable because all four excitonic states become mixed. They are all partially allowed and can be seen in the optical spectrum. In the case of a charged exciton, when two particles of the same type are at the same ground level, a spin singlet state is formed and thus there is no exchange interaction between the electron and hole. The simplified explanation of the exciton fine-structure presented here is generally

valid for most QDs that have been studied experimentally, which typically have low symmetry of C_{2v} (Figure 1.8), resulting in fine-structure splitting and dark states. However, the spin interaction can be significantly different in QDs with other specific symmetries. For example, theoretical calculations based on group theory suggest that QDs with rotational symmetry of C_{3v}, which is of particular importance in the context of this work, should not have dark states [70,71]. Instead, they should be composed of two pairs of bright degenerate states. The paucity of experimental reports for this scenario can be explained by the fact that many high symmetry dots tend to have D_{3h} symmetry. Some spin-spin interaction characteristics of C_{3v} symmetry nanostructures have been experimentally revealed with the help of a magnetic field [72, 73]. It was shown that the magnetic field can easily mix hole states $J = +\frac{3}{2}$ and $J = -\frac{3}{2}$ resulting in significantly different Zeeman interactions when compared to C_{2v} systems.

1.5 Entangled Photon Pairs from QDs

As mentioned in section 1.2, there are various methods to generate entangled photons. Researchers have achieved post-selective production of polarization-entangled photons from single photons by QDs interfering on a beam-splitter with high single photon purity and indistinguishability [74]. Additionally, time-bin entanglement has been shown using exciton and biexciton transitions [75]. However, one of the most promising ways to generate entangled photons is through the biexciton-exciton recombination cascade. The idea, first proposed by Benson et al. [64], is similar to methods used in single atoms. By exciting an empty QD to the biexciton state, which is composed of two excitons, the electrons and holes composing the biexciton have opposite spins due to the Pauli exclusion principle, resulting in a net spin of zero. The biexciton state is a single, non-degenerate state,

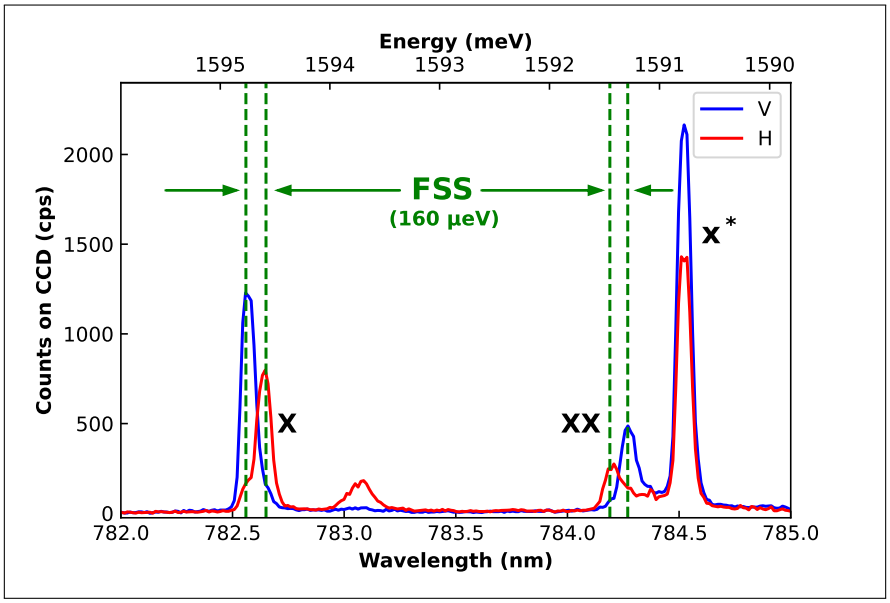


Figure 1.9: FSS phenomenology as a function of polarization. Different polarizations are well separated energetically from each other. X* represents a charged transition which does not show any splitting due to its singlet spin state. The difference between counts of H and V polarizations is due to the CCD polarization-wavelength response difference.

and it can only relax to the ground state by changing its angular momentum value by ±1 (selection rules are between p type and s type levels). The intermediate state is a neutral exciton, with two degenerate states with M=±1, provided that the QD is symmetric. During recombination to the state with M=-1(+1), a right-(left-)hand circularly polarized photon is emitted. Due to the total angular momentum constraint, further recombination results in the emission of a left-(right-)hand circularly polarized photon, given the emission of both successive photons are in the same direction. The superposition of these two possible photon emission is:

$$|\psi\rangle = \frac{1}{\sqrt{2}}\Big(|\mathrm{R_{XX}L_X}\rangle \pm |\mathrm{L_{XX}R_X}\rangle\Big) \tag{1.15}$$

1.5.1 FSS and Entanglement

The proposed method for generating polarization entanglement is a scenario that is not commonly observed in real quantum dots. The advantage of this method is that it relies on the degeneracy of the exciton level. However, in most QD systems, the degeneracy of the exciton level is lifted due to the electron-hole exchange interaction we discussed, when the confinement potential symmetry is low. This symmetry can be lowered due to various factors such as QD elongation [76, 77], strain [78], random alloy segregation [79], etc. In this case, the non-degenerate exciton levels are separated in energy by an amount equal to the FSS. Both levels are mixed and the optical selection rules that apply to linear polarization are valid. Thus, in general, a pair of emitted photons is colinearly polarized. Consider now the equations in 1.16 and 1.17 below (Jones matrix transformations).

$$|\mathrm{H}\rangle = \begin{bmatrix} 1 \\ 0 \end{bmatrix} \ , \ |\mathrm{V}\rangle = \begin{bmatrix} 0 \\ 1 \end{bmatrix} \ , \ |\mathrm{R}\rangle = \frac{1}{\sqrt{2}} \begin{bmatrix} 1 \\ -i \end{bmatrix} \ , \ |\mathrm{L}\rangle = \frac{1}{\sqrt{2}} \begin{bmatrix} 1 \\ +i \end{bmatrix} \tag{1.16}$$

$$|\mathrm{R}\rangle = \frac{1}{\sqrt{2}}\Big(|\mathrm{H}\rangle - i\,|\mathrm{V}\rangle\Big) \ , \ |\mathrm{L}\rangle = \frac{1}{\sqrt{2}}\Big(|\mathrm{H}\rangle + i\,|\mathrm{V}\rangle\Big) \tag{1.17}$$

By simply using Jones matrix transformations as indicated in equations 1.16 and 1.17, one can rewrite equation 1.15 in linear basis. A phase term would appear in the corresponding linear representation of entanglement which we will detail in the following. Since the biexciton is a spin singlet state without electron-hole exchange interaction, its level is a single degenerate state [80]. However, its ground state is the exciton, so the FSS is reflected in both transitions. See Figure 1.9 and Figure 1.10. Just like in the ideal scenario without FSS, a QD is initially populated by two particles (excitons) that create a spin singlet state, which can then be detected through the cascaded recombination process. Despite the FSS,

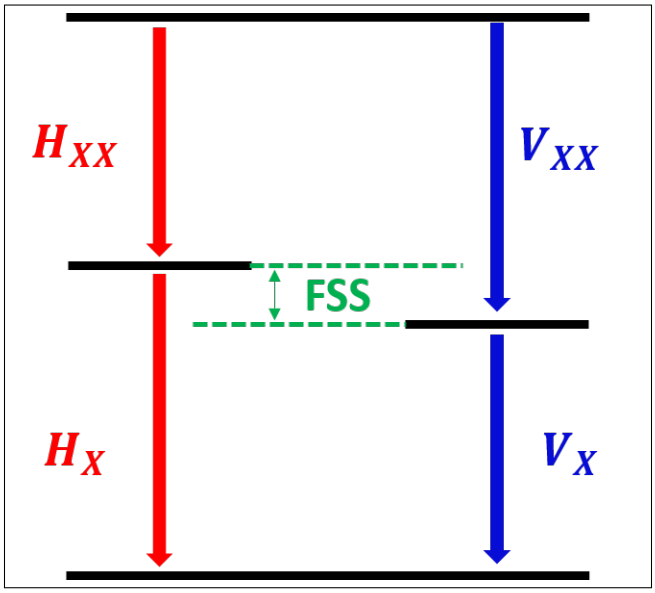


Figure 1.10: Schematics of excitonic complex of a QD energy levels with the presence of FSS

this process maintains the entangled nature of the original state [81]. However, the final entangled two-photon polarization state is affected by the FSS. So the modification of the entangled state occurs as follows: initially, a stationary biexciton state is created:

$$|\Psi\rangle = \frac{1}{\sqrt{2}}\Big(|\mathrm{XX_H} \otimes \mathrm{X_H}\rangle + |\mathrm{XX_V} \otimes \mathrm{X_V}\rangle\Big) \tag{1.18}$$

Once the first XX photon is emitted (H or V), the system is in an entangled photon-exciton state.

$$|\Psi\rangle = \frac{1}{\sqrt{2}}\Big(|\mathrm{H_{XX}} \otimes \mathrm{X_H}\rangle + |\mathrm{V_{XX}} \otimes \mathrm{X_V}\rangle\Big) \tag{1.19}$$

Since the non-degenerate exciton states have different energy levels, they evolve at different rates, which results in the emergence of an evolving phase term in the

state.

$$|\Psi\rangle = \frac{1}{\sqrt{2}}\Big(|\mathrm{H_{XX}} \otimes \mathrm{X_H}\rangle + e^{\frac{\mathrm{i.FSS.t}}{\hbar}} |\mathrm{V_{XX}} \otimes \mathrm{X_V}\rangle\Big) \tag{1.20}$$

After the emission of the second photon (X), the entanglement state is fully transferred from spin state to the photon polarization state. As the emission of the exciton is spontaneous, the phase term continues to evolve until the exciton photon is emitted, so we can replace t with τ_{X} as the exciton lifetime:

$$|\Psi\rangle = \frac{1}{\sqrt{2}}\Big(|\mathrm{H_{XX}} \otimes \mathrm{H_X}\rangle + e^{\frac{\mathrm{i.FSS.}\tau_{\mathrm{X}}}{\hbar}} |\mathrm{V_{XX}} \otimes \mathrm{V_X}\rangle\Big) \tag{1.21}$$

Equation 1.21 is a state that has a fixed phase term but doesn't change over time. However, due to the varying lifetime τ_{X} of individual excitons, the phase term values differ in the corresponding two-photon polarization states. The problem arising experimentally is that entanglement is ideally evaluated by using a statistical ensemble of identically prepared particles. This implies that, in the case of non-zero FSS, entanglement is practically evaluated for an ensemble containing a variety of different states, which makes the overall state mixed, and thus with reduced or absent entanglement. In other words, each recombination cascade (each two consecutive photons) emitted is entangled, however, it is different from the previous or next recombination. The final two-photon polarization state suggests that entanglement can be observed when either the FSS is very small, ideally zero, or photons for entanglement tests are selected with the same τ_X. The latter method of selecting photons with the same lifetime for entanglement tests can be used to create different types of entangled states, like $\frac{1}{\sqrt{2}}\big(|\mathrm{HH}\rangle - |\mathrm{VV}\rangle\big)$ or $\frac{1}{\sqrt{2}}\big(|\mathrm{HH}\rangle + i|\mathrm{VV}\rangle\big)$, but it comes with the cost of a less bright photon source, as a strong selection/filter is applied. QDs with no FSS and emitting all photons in a maximally entangled state $\frac{1}{\sqrt{2}}\big(|\mathrm{HH}\rangle + |\mathrm{VV}\rangle\big)$ would be advantageous in any practical application.

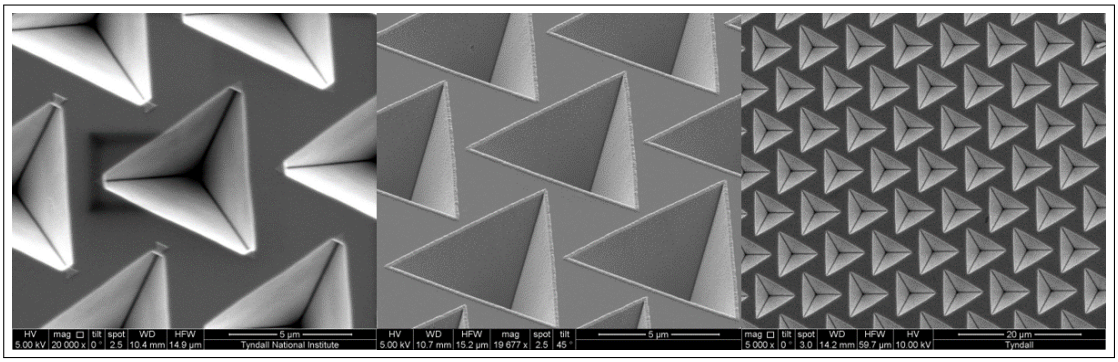


Figure 1.11: Inverted tetrahedral pyramidal recesses for epitaxial growth of QDs.

Pyramidal Quantum Dots

Over the past two decades, advances in semiconductor fabrication and a greater understanding of epitaxial growth have allowed for greater control over the epitaxial growth of QDs. In our group (Epitaxy and Physics of Nanostructures) we work on a specific type of self-assembled QDs. QDs are grown on a pre-patterned tetrahedral pyramidal recesses (see Figure 1.11). This growth, in contradiction to other growth techniques, lets the *nucleation* take place on arbitrarily defined *sites* (inverted pyramids). The term *Site-Controlled* Pyramidal QDs originates from this.

The complex growth scenario of epitaxial material on non-planar substrates, where surface kinetics and chemistry vary across different exposed crystallographic facets, is utilized to produce site-controlled quantum dots in pyramidal recesses. The process is driven by the so called "*self-limited*" growth mechanism that occurs in V-grooves [82] and tetrahedron templates [83] and results from a balance of two factors: **(1)** an anisotropic growth rate on the exposed side facets and **(2)** the influence of capillarity effects. See Figure 1.12. The reason for the anisotropic growth rate can be attributed to the varying properties of different surfaces. The pyramid sidewalls that are exposed are aligned along (111)A (Figure 1.12), which are terminated by Ga atoms. If the structures are grown under certain growth

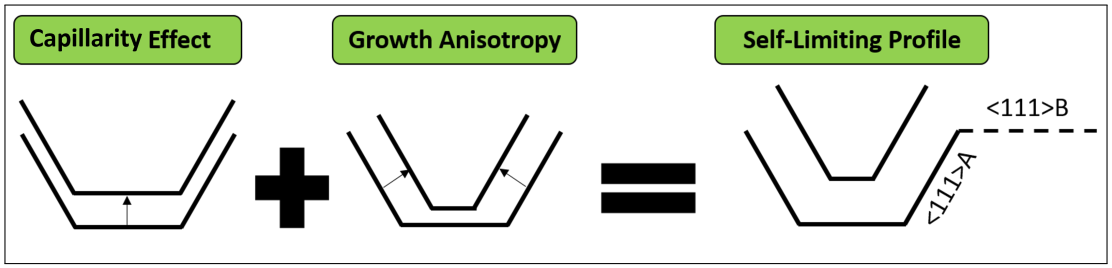


Figure 1.12: The self-limiting profile which is a balance between the capillary effect and anistropic growth for non planar facets.

conditions, there exists a higher concentration of precursor decomposition sites on the (111)A sidewalls. This results in a noticeable difference in the rate of decomposition, leading to a faster growth of the crystal on the sidewalls. The capillarity effect, in which adatoms move to reduce surface energy by making the surface more planar, can be explained by considering the shape of a pyramidal recess. The adatoms tend to flow to the bottom of the pyramid. If they are close enough to the bottom, within a few hundred nanometers, they can easily reach it, causing an increase in the growth rate at the bottom. This also tends to make the base of the pyramid wider along the (111)B direction. As QD growth incorporates growth of different layers of III-V semiconductors with different alloy compositions, alloy segregation which stems from difference in diffusion rate of different elements in such a tetrahedron structure is unavoidable. Thus, different features other than the QD will form during the growth process. These features are Vertical Quantum Wire (VQWr), Vertical Quantum Well (VQW), lateral QWr and lateral QW. VQWr is detrimental to the quality of entanglement as it alters the symmetry of confining potential of the QD. These features are sketched and detailed in chapter 3 as they are more relevant to the chapter discussion.

The Growth and post-growth process (as in this thesis) flow is schematically depicted in Figure 1.13. It is as follows:

1. The tetrahedral puramidal recess is patterned on <111>B GaAs wafer with

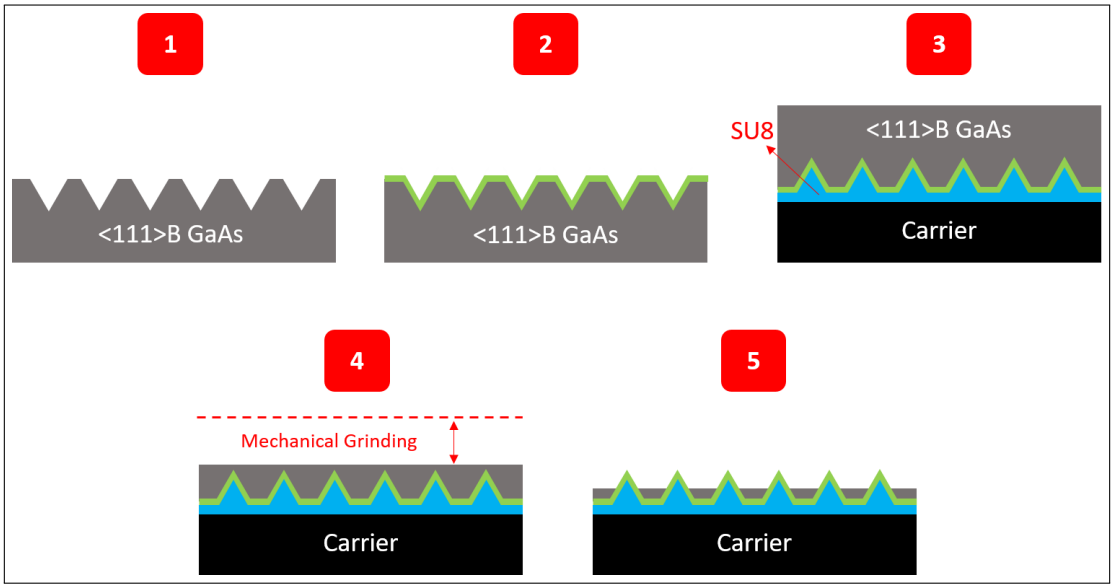


Figure 1.13: The Growth and post-growth process flow. **(1)** Tetrahedral pyramidal recesses are patterned on <111>B GaAs wafer. **(2)** The QD heterostructure is grown in the MOVPE reactor. **(3)** As-grown sample is flipped and attached to a carrier with, for example, SU8(photoresist) for mechanical grinding. **(4)** Sample is ground until ∼30μm of GaAs wafer is left. **(5)** Sample is then immersed into etching solution until pyramid's tips are exposed(chemical back-etching).

pholollithography process. Pyramid pitches are usually 7.5μm, 10μm or 12.5μm. See Figure 1.11.

2. QDs are grown in the MOVPE reactor. See Figure 1.14 as grown and as grown cross section insets. The layer sequence appears similar to that of a quantum well sample.

3. The as grown sample is attached to a carrier (typically <100> GaAs wafer) with the help of a photoresist (SU8) hard baked at the temperature of 150°C for 10 minutes.

4. As-grown sample is then mechanically ground (from 360μm to ∼30μm).

5. The sample-carrier bundle is then immersed into the etching solution (NH_4OH + H_2O_2 with the PH of 2.7) until the pyramids are exposed (this method is

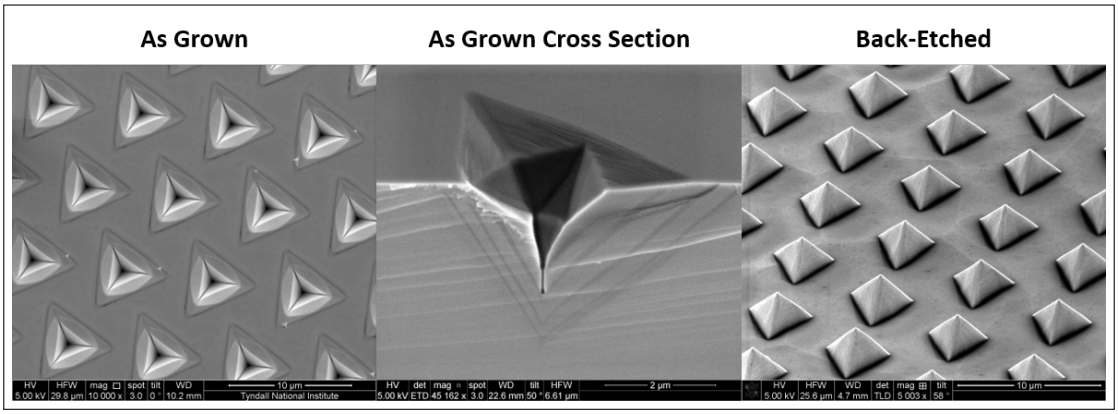


Figure 1.14: As grown (top view and cross-section) and back-etched pyramids.

called Chemical Back-Etching. see Figure 1.14 Back-Etched inset).

1.6 Characterization of QDs

In this section, we will review some experimental techniques we used to characterize QDs. This includes cryogenics photoluminescence, polarization resolved spectroscopy and Time-Resolved spectroscopy.

1.6.1 Cryogenics Photoluminescence

Why cryogenic photoluminescence measurements?

Enhanced emission properties: Cooling the QDs to cryogenic temperatures, typically below 10 Kelvin, helps to suppress non-radiative recombination channels and enhances radiative processes. This leads to improved photon emission efficiency, reduced background noise, and higher purity of the emitted single photons.

Reduction of phonon interactions: Cryogenic temperatures significantly reduce the thermal energy and phonon population in the material. Phonons can interact with the quantum dot exciton states and cause decoherence or non-

radiative relaxation. Cooling the QDs to cryogenic temperatures minimizes phonon interactions, enhancing the coherence properties of the quantum dot excitons and improving the single photon emission purity.

Elimination of charge fluctuations: At room temperature, quantum dots can experience charge fluctuations due to thermal energy and interactions with the surrounding environment and phonons. These fluctuations can cause variations in the emission properties and hinder the generation of single photons. By cooling the QDs to cryogenic temperatures, the charge fluctuations (and phonons too) are reduced, providing a more stable and well-defined emission from the quantum dot, enabling better control over single photon generation.

Suppression of Auger recombination: Auger recombination is a non-radiative process that can occur in quantum dots, particularly at higher temperatures. It involves the energy transfer from an exciton to an additional carrier, leading to the non-radiative decay of the exciton state. Cryogenic temperatures help to suppress Auger recombination, allowing for a higher probability of radiative recombination and increasing the efficiency of single photon emission.

After the as grown sample is processed, it is mounted on the copper/gold stage of our ARS closed helium cycle cryostat. The sample is cooled down to $\sim$6 Kelvins in about 2 hours and 30 mins. The sample temperature can be checked by the bulk GaAs emission at low temperature (820nm). The 630nm laser is illuminated to the sample for above band excitation to create excitonic complexes around QD or resonantly directly inside the QD. A Long Pass (LP) filter is introduced to the optical path to block the laser emission and send the QD emission to the monochromator. The spectrum is then monitored by a custom made computer software. This techniques is often called micro-photoluminescence (μPL) since it combines photoluminescence with spatially resolved measurements at a microscale level. It enables the investigation of the local optical properties of a material (in this

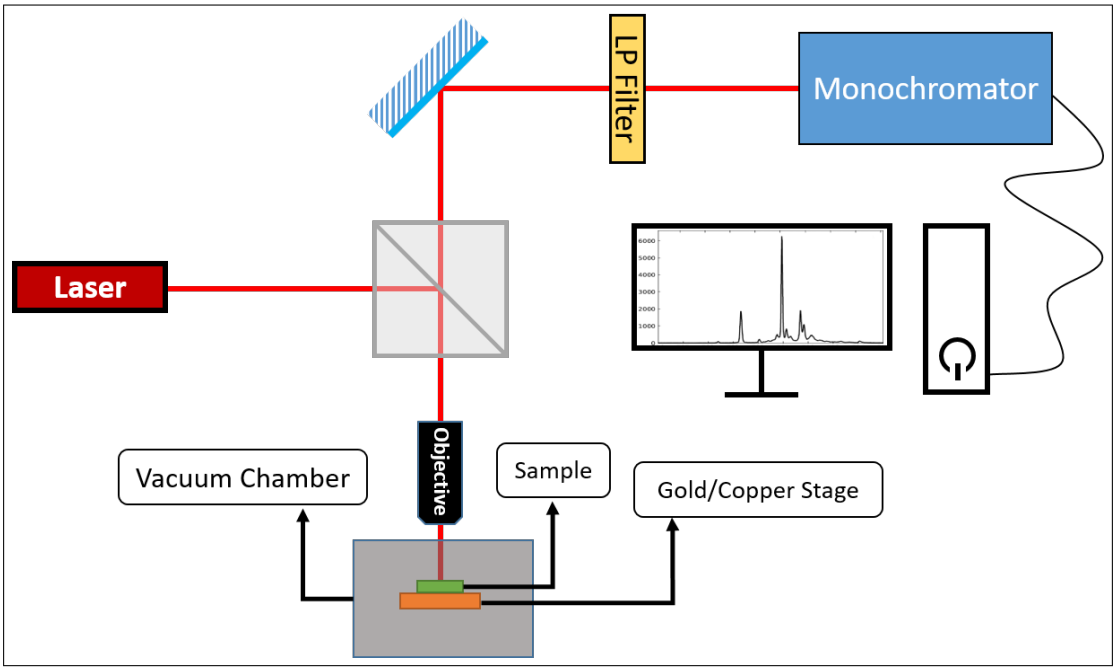


Figure 1.15: Schematic diagram of photoluminescence optical setup. Long pass (LP) filter, filters the laser and the QD emission is sent to the monochromator. The BS is 10:90 (10% Reflection, 90% Transmission).

case site-controlled pyramidal QDs) with high spatial resolution. See Figure 1.15.

1.6.2 Polarization-Resolved Spectroscopy

Polarization resolved spectroscopy needed to be implemented to observe the fine structure splitting, considering that small FSS are beyond the resolution of the detection systems. For example, the maximum resolution of our monochromators with 1800 grooves per millimeter grating is 20μeV, however QDs have FSS of orders of few μeV's. As mentioned above, the FSS is reflected in the polarization of the different transitions (see Figure 1.9). If the FSS is small enough, the observed peak is the overlapped V and H polarizations, see Figure 1.16. In the upper inset, it shows the overlap of V and H polarizations. By using a linear polarizer, when it is aligned vertically, the H polarization is minimized and the overall peak shifts

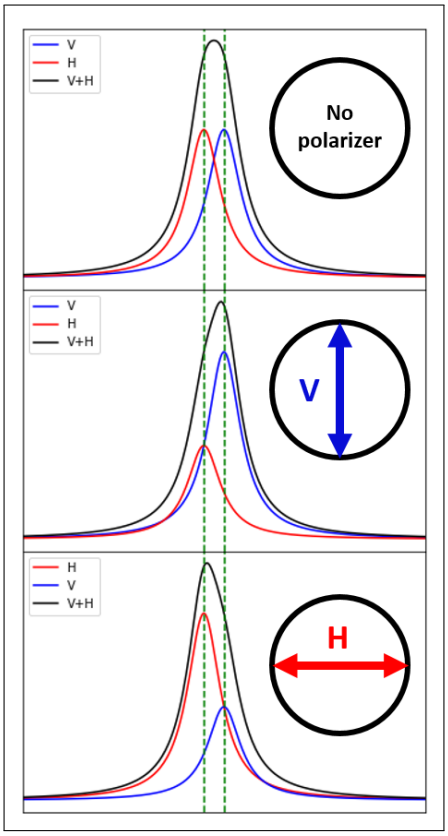


Figure 1.16: Polarization resolved spectroscopy. The upper most inset indicates the overlapped V and H polarizations when there is no polarization optics on the way. By introducing a linear polarizer, once it is vertically aligned, the H polarization is suppressed and the overall peak moves toward the vertical polarization as indicated in the middle inset. The opposite will happen when the polarizer is horizontal (the bottom inset).

towards the vertical polarization as shown in the middle inset. The opposite effect will occur when the polarizer is aligned horizontally. The measurement is recorded for one complete round of the polarizer. The recorded data is then analyzed. By tracking the displacement of the peak value of the overlapped curve (black curve), a sinusoidal curve is made. The domain of this sinusoidal curve indicates the amount of fine structure splitting.

1.6.3 Time-Resolved Spectroscopy

This method implements single photon counting modules to measure the lifetime of exciton (X) and biexciton (XX) and second order correlation function $g^{(2)}(\tau)$. But why do we utilize this method? Time-resolved measurements are performed in the QD community for quantum information and quantum dot applications for several reasons:

Quantum coherence characterization: Time-resolved measurements allow researchers to study the coherence properties of quantum dots. Coherence refers to the ability of a quantum system to maintain and control quantum states without excessive decoherence. By analyzing the dynamics of carrier recombination and relaxation processes in quantum dots, researchers can assess the coherence times and understand the factors affecting coherence, such as phonon interactions, dephasing, and environmental effects.

Exciton and biexciton dynamics: Time-resolved measurements provide insights into the exciton and biexciton dynamics, including exciton formation, radiative and non-radiative decay processes, and exciton-exciton interactions. These dynamics are crucial for understanding and manipulating the optical properties of quantum dots, which indeed are essential for applications such as single-photon sources and quantum information processing.

Carrier capture and relaxation: Quantum dots have discrete energy levels, leading to efficient carrier capture and long carrier lifetimes. Time-resolved measurements help in understanding the carrier capture processes, carrier relaxation mechanisms, and carrier dynamics within the quantum dot structure. This knowledge is vital for optimizing the efficiency of quantum dot-based devices, such as lasers, detectors, and quantum dot solar cells.

In general, for quantum information applications, by investigating the lifetimes, coherence properties, and gate operations of qubits, one can assess their suitability

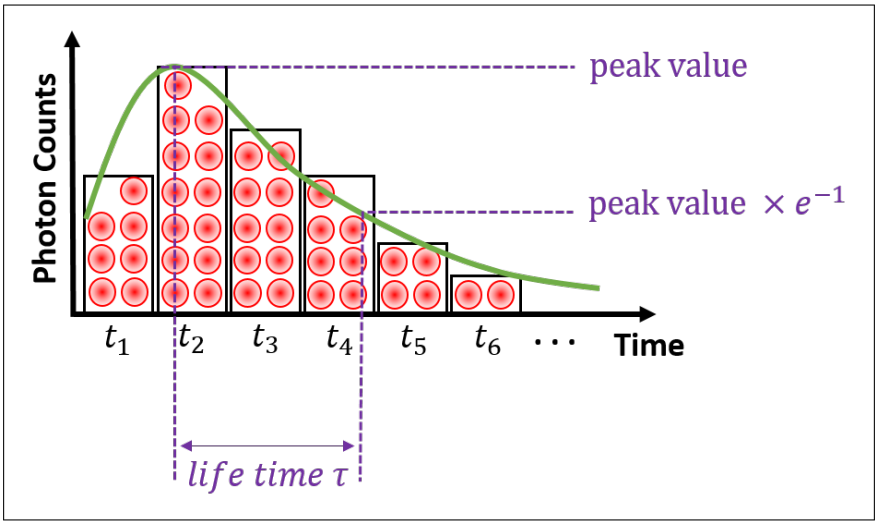


Figure 1.17: Time resolved spectroscopy. A method used to measure the emission life time of different excitonic transitions.

for quantum information applications and identify methods for enhancing their performance.

Life-Time

The idea is rather simple. There are two detectors, one triggers the timer to start and the second stops the timer. The elapsed time is regarded as the lifetime of the transition under study. For XX, the start is the laser signal and the stop is the signal from the , e.g., APD (Avalanche Photo Diode) once it detects a single XX photon. For X, the start would be the XX signal and the stop the X signal. This is because the X transition will recombine after the XX transition has taken place. Because the recombination is spontaneous, it varies with time at each recombination. The best way to measure the average lifetime is to build a statistics, create a histogram. Then an exponential fit will determine the lifetime. Histogram is made by integrating the number of photons arrived in each time bin $(t_i, i = 1, 2, 3, ...)$ after the timer has been started. By convention, after the fitting, the time by which the peak value drops by $1/e$ is considered as the lifetime. See

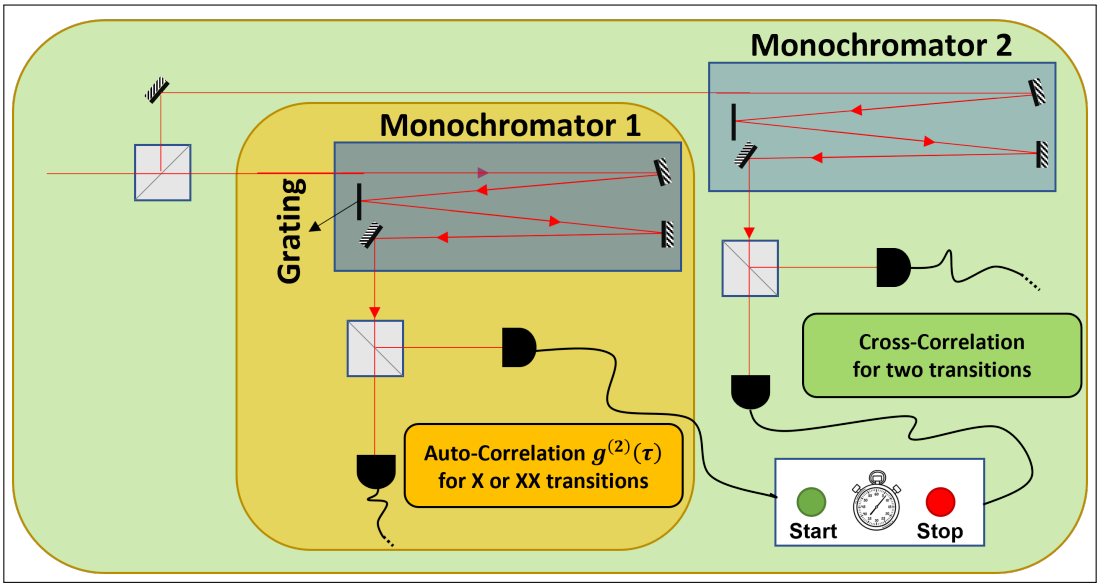


Figure 1.18: Time resolved spectroscopy. Auto-Correlation measurement to measure second order correlation function value $g^{(2)}(\tau)$ for one transition (X or XX) and Cross-Correlation measurement to measure X lifetime or observing cascade.

Figure 1.17.

Second Order Correlation Fucntion $g^{(2)}(\tau)$

The second order correlation function is a figure of merit to show how good the photon source is generating single photons. Correlation measurements were conducted in a classical Hanbury Brown and Twiss (HBT) setup (Figure 1.18). An auto-correlation curve can be obtained by filtering an appropriate excitonic transition using a monochromator. The filtered light is then split by a nonpolarizing 50:50 beamsplitter and detected by two avalanche photo diodes (APD), which act as single photon detectors. One APD initiates the photon counting module, while the other, delayed, stops it. The resulting histogram of time intervals between the start and stop signals mimics the second order correlation function. Cross-correlations can be measured by splitting the photoluminescence using a nonpolarizing 50:50

beamsplitter and directing it to two different monochromators, which pass appropriate excitonic transitions of different wavelengths. The resulting $g^{(2)}(\tau)$ can then be measured in the same manner as in auto-correlation measurements. If polarization-resolved measurements are required, a polarizer or polarizing beamsplitters can be placed in front of the APDs. Our setup is equipped with four APDs, allowing for four curves to be measured simultaneously.

1.7 Summary and Conclusion

In summary, we introduced some basic concepts necessary to understand the next chapters. We started by the essence of quantum information, we introduced some possible candidates as carriers of quantum information, and by picking up the semiconductor QD, we detailed the physics and challenges arising with this system as single photon and entangled photon pair source. Eventually, we briefed most important characterization techniques including μPL (micro-photoluminescence), polarization-resolved spectroscopy and time resolved spectroscopy. In the next chapters, we will use these material and techniques to have a better understanding of our special type of QDs called "*Site-Controlled Pyramidal QDs*".

Bibliography

[1] P. Kok and B. W. Lovett, *Introduction to Optical Quantum Information Processing*. Cambridge University Press, 2010.

[2] M. A. Nielsen and I. L. Chuang, *Quantum Computation and Quantum Information*. Cambridge University Press, 2000.

[3] J. S. Bell, "On the Einstein Podolsky Rosen paradox," *Physics*, vol. 1, no. 3, pp. 195–200, 1964.

[4] R. LaPierre, *Single Photon State*, pp. 49–55. Cham: Springer International Publishing, 2022.

[5] M. D. Eisaman, J. Fan, A. Migdall, and S. V. Polyakov, "Invited review article: Single-photon sources and detectors," *Review of Scientific Instruments*, vol. 82, no. 7, p. 071101, 2011.

[6] R. Boyd and D. Prato, *Nonlinear Optics*. Elsevier Science, 2008.

[7] L. Mandel and E. Wolf, *Optical Coherence and Quantum Optics*. Cambridge University Press, 1995.

[8] Y. H. Shih and C. O. Alley, "New type of einstein-podolsky-rosen-bohm experiment using pairs of light quanta produced by optical parametric down conversion," *Phys. Rev. Lett.*, vol. 61, pp. 2921–2924, Dec 1988.

[9] Z. Y. Ou and L. Mandel, "Violation of bell's inequality and classical probability in a two-photon correlation experiment," *Phys. Rev. Lett.*, vol. 61, pp. 50–53, Jul 1988.

[10] G. Weihs and A. Zeilinger, "Photon statistics at beam-splitters: an essential tool in quantum information and teleportation," *Coherence and Statistics of Photons and Atoms*, pp. 262–288, 2001.

[11] J. E. Sharping, M. Fiorentino, and P. Kumar, "Observation of twin-beam-type quantum correlation in optical fiber," *Opt. Lett.*, vol. 26, pp. 367–369, Mar 2001.

[12] M. Fiorentino, P. Voss, J. Sharping, and P. Kumar, "All-fiber photon-pair source for quantum communications," *IEEE Photonics Technology Letters*, vol. 14, no. 7, pp. 983–985, 2002.

[13] X. Li, P. L. Voss, J. E. Sharping, and P. Kumar, "Optical-fiber source of polarization-entangled photons in the 1550 nm telecom band," *Phys. Rev. Lett.*, vol. 94, p. 053601, Feb 2005.

[14] J. G. Rarity, J. Fulconis, J. Duligall, W. J. Wadsworth, and P. S. J. Russell, "Photonic crystal fiber source of correlated photon pairs," *Opt. Express*, vol. 13, pp. 534–544, Jan 2005.

[15] J. Fan, A. Dogariu, and L. J. Wang, "Generation of correlated photon pairs in a microstructure fiber," *Opt. Lett.*, vol. 30, pp. 1530–1532, Jun 2005.

[16] J. Fan, A. Migdall, and L. J. Wang, "Efficient generation of correlated photon pairs in a microstructure fiber," *Opt. Lett.*, vol. 30, pp. 3368–3370, Dec 2005.

[17] J. Fan and A. Migdall, "Phase-sensitive four-wave mixing and raman suppression in a microstructure fiber with dual laser pumps," *Opt. Lett.*, vol. 31, pp. 2771–2773, Sep 2006.

[18] S. J. Freedman and J. F. Clauser, "Experimental test of local hidden-variable theories," *Phys. Rev. Lett.*, vol. 28, pp. 938–941, Apr 1972.

[19] E. S. Fry and R. C. Thompson, "Experimental test of local hidden-variable theories," *Phys. Rev. Lett.*, vol. 37, pp. 465–468, Aug 1976.

[20] A. Aspect, P. Grangier, and G. Roger, "Experimental tests of realistic local theories via bell's theorem," *Phys. Rev. Lett.*, vol. 47, pp. 460–463, Aug 1981.

[21] M. Hennrich, T. Legero, A. Kuhn, and G. Rempe, "Photon statistics of a non-stationary periodically driven single-photon source," *New Journal of Physics*, vol. 6, p. 86, jul 2004.

[22] M. Hijlkema, B. Weber, H. P. Specht, S. C. Webster, A. Kuhn, and G. Rempe, "A single-photon server with just one atom," *Nature Physics*, vol. 3, pp. 253–255, Apr 2007.

[23] A. Kuhn, M. Hennrich, and G. Rempe, "Deterministic single-photon source for distributed quantum networking," *Phys. Rev. Lett.*, vol. 89, p. 067901, Jul 2002.

[24] T. Wilk, S. C. Webster, H. P. Specht, G. Rempe, and A. Kuhn, "Polarization-controlled single photons," *Phys. Rev. Lett.*, vol. 98, p. 063601, Feb 2007.

[25] B. Dayan, A. S. Parkins, T. Aoki, E. P. Ostby, K. J. Vahala, and H. J. Kimble, "A photon turnstile dynamically regulated by one atom," *Science*, vol. 319, no. 5866, pp. 1062–1065, 2008.

[26] T. Aoki, A. S. Parkins, D. J. Alton, C. A. Regal, B. Dayan, E. Ostby, K. J. Vahala, and H. J. Kimble, "Efficient routing of single photons by one atom and a microtoroidal cavity," *Phys. Rev. Lett.*, vol. 102, p. 083601, Feb 2009.

[27] C. Brunel, B. Lounis, P. Tamarat, and M. Orrit, "Triggered source of single photons based on controlled single molecule fluorescence," *Phys. Rev. Lett.*, vol. 83, pp. 2722–2725, Oct 1999.

[28] S. C. Kitson, P. Jonsson, J. G. Rarity, and P. R. Tapster, "Intensity fluctuation spectroscopy of small numbers of dye molecules in a microcavity," *Phys. Rev. A*, vol. 58, pp. 620–627, Jul 1998.

[29] C. Maurer, C. Becher, C. Russo, J. Eschner, and R. Blatt, "A single-photon source based on a single ca+ ion," *New Journal of Physics*, vol. 6, p. 94, jul 2004.

[30] M. Keller, B. Lange, K. Hayasaka, W. Lange, and H. Walther, "Continuous generation of single photons with controlled waveform in an ion-trap cavity system," *Nature*, vol. 431, pp. 1075–1078, Oct 2004.

[31] J. D. Arias Espinoza, K. Groenland, M. Mazzanti, K. Schoutens, and R. Gerritsma, "High-fidelity method for a single-step n-bit toffoli gate in trapped ions," *Phys. Rev. A*, vol. 103, p. 052437, May 2021.

[32] X. Wang, A. Sørensen, and K. Mølmer, "Multibit gates for quantum computing," *Phys. Rev. Lett.*, vol. 86, pp. 3907–3910, Apr 2001.

[33] O. Katz, M. Cetina, and C. Monroe, "n-body interactions between trapped ion qubits via spin-dependent squeezing," *Phys. Rev. Lett.*, vol. 129, p. 063603, Aug 2022.

[34] C. Kurtsiefer, S. Mayer, P. Zarda, and H. Weinfurter, "Stable solid-state source of single photons," *Phys. Rev. Lett.*, vol. 85, pp. 290–293, Jul 2000.

[35] R. Brouri, A. Beveratos, J.-P. Poizat, and P. Grangier, "Photon antibunching in the fluorescence of individual color centers in diamond," *Opt. Lett.*, vol. 25, pp. 1294–1296, Sep 2000.

[36] E. Pelucchi, "On the multifaceted journey for the invention of epitaxial quantum dots," *Progress in Crystal Growth and Characterization of Materials*, vol. 69, no. 2, p. 100603, 2023.

[37] H. Kroemer, "A proposed class of hetero-junction injection lasers," *Proceedings of the IEEE*, vol. 51, no. 12, pp. 1782–1783, 1963.

[38] V. N. Lutskii, "Quantum size effect—present state and perspectives of experimental investigations," *physica status solidi (a)*, vol. 1, no. 2, pp. 199–220, 1970.

[39] R. Dingle, W. Wiegmann, and C. H. Henry, "Quantum states of confined carriers in very thin al$_x$ga$_{1-x}$As-gaas-al$_x$ga$_{1-x}$As heterostructures," *Phys. Rev. Lett.*, vol. 33, pp. 827–830, Sep 1974.

[40] R. Dingle, *Confined carrier quantum states in ultrathin semiconductor heterostructures*, pp. 21–48. Berlin, Heidelberg: Springer Berlin Heidelberg, 1975.

[41] A. Consortini and B. R. Frieden, "Quantum-mechanical solution for the simple harmonic oscillator in a box," *Il Nuovo Cimento B Series 11*, vol. 35, pp. 153–164, Oct. 1976.

[42] A. Cho and J. Arthur, "Molecular beam epitaxy," *Progress in Solid State Chemistry*, vol. 10, pp. 157–191, 1975.

[43] R. D. Dupuis, "Metalorganic chemical vapor deposition of iii-v semiconductors," *Science*, vol. 226, no. 4675, pp. 623–629, 1984.

[44] K. v. Klitzing, G. Dorda, and M. Pepper, "New method for high-accuracy determination of the fine-structure constant based on quantized hall resistance," *Phys. Rev. Lett.*, vol. 45, pp. 494–497, Aug 1980.

[45] Y. Ota, "Silicon molecular beam epitaxy," *Thin Solid Films*, vol. 106, no. 1, pp. 1–136, 1983.

[46] J. R. Arthur, "Molecular beam epitaxy," *Surface Science*, vol. 500, no. 1, pp. 189–217, 2002.

[47] C. A. Wang, "Early history of movpe reactor development," *Journal of Crystal Growth*, vol. 506, pp. 190–200, 2019.

[48] G. Binnig, C. F. Quate, and C. Gerber, "Atomic force microscope," *Phys. Rev. Lett.*, vol. 56, pp. 930–933, Mar 1986.

[49] Y. Arakawa and H. Sakaki, "Multidimensional quantum well laser and temperature dependence of its threshold current," *Applied Physics Letters*, vol. 40, pp. 939–941, 06 1982.

[50] P. M. Petroff, A. C. Gossard, R. A. Logan, and W. Wiegmann, "Toward quantum well wires: Fabrication and optical properties," *Applied Physics Letters*, vol. 41, pp. 635–638, 10 1982.

[51] K. Kash, A. Scherer, J. M. Worlock, H. G. Craighead, and M. C. Tamargo, "Optical spectroscopy of ultrasmall structures etched from quantum wells," *Applied Physics Letters*, vol. 49, pp. 1043–1045, 10 1986.

[52] J. Cibert, P. M. Petroff, G. J. Dolan, S. J. Pearton, A. C. Gossard, and J. H. English, "Optically detected carrier confinement to one and zero dimension in GaAs quantum well wires and boxes," *Applied Physics Letters*, vol. 49, pp. 1275–1277, 11 1986.

[53] H. Temkin, G. J. Dolan, M. B. Panish, and S. N. G. Chu, "Low-temperature photoluminescence from InGaAs/InP quantum wires and boxes," *Applied Physics Letters*, vol. 50, pp. 413–415, 02 1987.

[54] Y. Miyamoto, M. Cao, Y. Shingai, K. Furuya, Y. Suematsu, K. G. Ravikumar, and S. Arai, "Light emission from quantum-box structure by current injection," *Japanese Journal of Applied Physics*, vol. 26, p. L225, apr 1987.

[55] G. W. Bryant, "Excitons in quantum boxes: Correlation effects and quantum confinement," *Phys. Rev. B*, vol. 37, pp. 8763–8772, May 1988.

[56] D. Gershoni, H. Temkin, G. J. Dolan, J. Dunsmuir, S. N. G. Chu, and M. B. Panish, "Effects of two-dimensional confinement on the optical properties of InGaAs/InP quantum wire structures," *Applied Physics Letters*, vol. 53, pp. 995–997, 09 1988.

[57] S. R. Andrews, H. Arnot, P. K. Rees, T. M. Kerr, and S. P. Beaumont, "Photoluminescence studies of free-standing quantum boxes," *Journal of Applied Physics*, vol. 67, pp. 3472–3480, 04 1990.

[58] I. Tan, Y. Chang, R. Mirin, E. Hu, J. Merz, T. Yasuda, and Y. Segawa, "Observation of increased photoluminescence decay time in strain-induced quantum-well dots," *Applied Physics Letters*, vol. 62, pp. 1376–1378, 03 1993.

[59] E. Bauer, "Phänomenologische theorie der kristallabscheidung an oberflächen. i," *Zeitschrift für Kristallographie-Crystalline Materials*, vol. 110, no. 1-6, pp. 372–394, 1958.

[60] E. Bauer, "Phänomenologische theorie der kristallabscheidung an oberflächen. ii," *Zeitschrift für Kristallographie-Crystalline Materials*, vol. 110, no. 1-6, pp. 395–43, 1958.

[61] M. Gurioli, Z. Wang, A. Rastelli, T. Kuroda, and S. Sanguinetti, "Droplet epitaxy of semiconductor nanostructures for quantum photonic devices," *Nature Materials*, vol. 18, pp. 799–810, Aug 2019.

[62] M. Abbarchi, F. Troiani, C. Mastrandrea, G. Goldoni, T. Kuroda, T. Mano, K. Sakoda, N. Koguchi, S. Sanguinetti, A. Vinattieri, and M. Gurioli, "Spectral diffusion and line broadening in single self-assembled gaas/algaas quantum dot photoluminescence," *Applied Physics Letters*, vol. 93, no. 16, p. 162101, 2008.

[63] Z. M. Wang, K. Holmes, Y. I. Mazur, K. A. Ramsey, and G. J. Salamo, "Self-organization of quantum-dot pairs by high-temperature droplet epitaxy," *Nanoscale Research Letters*, vol. 1, p. 57, Jul 2006.

[64] O. Benson, C. Santori, M. Pelton, and Y. Yamamoto, "Regulated and entangled photons from a single quantum dot," *Phys. Rev. Lett.*, vol. 84, pp. 2513–2516, Mar 2000.

[65] R. S. Knox, *Introduction to Exciton Physics*, pp. 183–245. Boston, MA: Springer US, 1983.

[66] M. Fox, *Quantum Optics: An Introduction*. Oxford Master Series in Physics, OUP Oxford, 2006.

[67] M. Bayer, G. Ortner, O. Stern, A. Kuther, A. A. Gorbunov, A. Forchel, P. Hawrylak, S. Fafard, K. Hinzer, T. L. Reinecke, S. N. Walck, J. P. Reithmaier, F. Klopf, and F. Schäfer, "Fine structure of neutral and charged excitons in self-assembled in(ga)as/(al)gaas quantum dots," *Phys. Rev. B*, vol. 65, p. 195315, May 2002.

[68] D. Gammon, A. L. Efros, T. A. Kennedy, M. Rosen, D. S. Katzer, D. Park, S. W. Brown, V. L. Korenev, and I. A. Merkulov, "Electron and nuclear spin interactions in the optical spectra of single gaas quantum dots," *Phys. Rev. Lett.*, vol. 86, pp. 5176–5179, May 2001.

[69] H. W. van Kesteren, E. C. Cosman, W. A. J. A. van der Poel, and C. T. Foxon, "Fine structure of excitons in type-ii gaas/alas quantum wells," *Phys. Rev. B*, vol. 41, pp. 5283–5292, Mar 1990.

[70] K. F. Karlsson, M. A. Dupertuis, D. Y. Oberli, E. Pelucchi, A. Rudra, P. O. Holtz, and E. Kapon, "Fine structure of exciton complexes in high-symmetry quantum dots: Effects of symmetry breaking and symmetry elevation," *Phys. Rev. B*, vol. 81, p. 161307, Apr 2010.

[71] M. A. Dupertuis, K. F. Karlsson, D. Y. Oberli, E. Pelucchi, A. Rudra, P. O. Holtz, and E. Kapon, "Symmetries and the polarized optical spectra of exciton complexes in quantum dots," *Phys. Rev. Lett.*, vol. 107, p. 127403, Sep 2011.

[72] M. T. Rakher, L. Ma, M. Davanço, O. Slattery, X. Tang, and K. Srinivasan, "Simultaneous wavelength translation and amplitude modulation of single photons from a quantum dot," *Phys. Rev. Lett.*, vol. 107, p. 083602, Aug 2011.

[73] M. V. Durnev, M. M. Glazov, E. L. Ivchenko, M. Jo, T. Mano, T. Kuroda, K. Sakoda, S. Kunz, G. Sallen, L. Bouet, X. Marie, D. Lagarde, T. Amand, and B. Urbaszek, "Magnetic field induced valence band mixing in [111] grown semiconductor quantum dots," *Phys. Rev. B*, vol. 87, p. 085315, Feb 2013.

[74] D. Fattal, K. Inoue, J. Vučković, C. Santori, G. S. Solomon, and Y. Yamamoto, "Entanglement formation and violation of bell's inequality with a semiconductor single photon source," *Phys. Rev. Lett.*, vol. 92, p. 037903, Jan 2004.

[75] H. Jayakumar, A. Predojević, T. Kauten, T. Huber, G. S. Solomon, and G. Weihs, "Time-bin entangled photons from a quantum dot," *Nature Communications*, vol. 5, p. 4251, Jun 2014.

[76] D. Gammon, E. S. Snow, B. V. Shanabrook, D. S. Katzer, and D. Park, "Fine structure splitting in the optical spectra of single gaas quantum dots," *Phys. Rev. Lett.*, vol. 76, pp. 3005–3008, Apr 1996.

[77] R. M. Stevenson, R. M. Thompson, A. J. Shields, I. Farrer, B. E. Kardynal, D. A. Ritchie, and M. Pepper, "Quantum dots as a photon source for passive quantum key encoding," *Phys. Rev. B*, vol. 66, p. 081302, Aug 2002.

[78] R. Seguin, A. Schliwa, S. Rodt, K. Pötschke, U. W. Pohl, and D. Bimberg, "Size-dependent fine-structure splitting in self-organized InAs/GaAs quantum dots," *Phys. Rev. Lett.*, vol. 95, p. 257402, Dec 2005.

[79] V. Mlinar and A. Zunger, "Effect of atomic-scale randomness on the optical polarization of semiconductor quantum dots," *Phys. Rev. B*, vol. 79, p. 115416, Mar 2009.

[80] V. Mlinar and A. Zunger, "Internal electronic structure and fine structure of multiexcitons in semiconductor quantum dots," *Phys. Rev. B*, vol. 80, p. 205311, Nov 2009.

[81] R. M. Stevenson, A. J. Hudson, A. J. Bennett, R. J. Young, C. A. Nicoll, D. A. Ritchie, and A. J. Shields, "Evolution of entanglement between distinguishable light states," *Phys. Rev. Lett.*, vol. 101, p. 170501, Oct 2008.

[82] G. Biasiol and E. Kapon, "Mechanisms of self-ordering of quantum nanostructures grown on nonplanar surfaces," *Phys. Rev. Lett.*, vol. 81, pp. 2962–2965, Oct 1998.

[83] A. Hartmann, L. Loubies, F. Reinhardt, and E. Kapon, "Self-limiting growth of quantum dot heterostructures on nonplanar 111b substrates," *Applied Physics Letters*, vol. 71, no. 10, pp. 1314–1316, 1997.

Chapter 2

InGaAs QDs

2.1 The Anti-Binding Biexciton

Historically, the typical first approach to excite a QD to the biexciton state has been of non-resonant nature (optical or electrical excitation of the QD barriers)—a process that is incoherent, noisy, and largely inefficient due to the probabilistic population of different types of excitonic complexes, overall degrading the properties of quantum light emitters. Recent advancements in experimental settings marked a paradigm change toward resonant excitation methods to maximize QD benefits, especially valuable if combined with a QD site-control capability as in this thesis. By exploiting resonant methods, population inversion of exciton and biexciton states can be achieved, via for example Rabi oscillations [1,2], adiabatic rapid passage [3,4] and, later proposed and demonstrated, robust schemes utilizing phonon dressed states [5–7]. Irrespective of being a coherent or an incoherent phonon-assisted process, two-photon excitation is becoming a standard initialization process for the biexciton state in experiments and applications requiring a high quality pair of polarization-entangled photons. Near unity initialization fidelity [8], spectral purity [9], near perfect single photon emission [10], and others, sometimes in combination with recent integrated photonics advancements, are all critical outcomes of these

approaches. Experimentally, the two-photon excitation scheme can be realized because of the non-degeneracy of the exciton and biexciton states arising from the interplay of Coulomb interactions and "zero" dimensional geometrical constrictions [11]. The energy difference $\Delta E_B = E_X - E_{XX}$ between the exciton E_X and biexciton E_{XX} is generally referred to as the binding energy of the biexciton complex. In III–V epitaxial QDs, the ΔE_B value is typically within the range of a few meV. While coherent two-photon excitation (TPE) fulfills the energy conservation requirement $2E_{Laser} = E_X + E_{XX}$, the laser photon energy E_{Laser} will be detuned from the exciton by $-\Delta E_B/2$ (Figure 2.1a). Thus, picosecond pulses satisfying the TPE condition can relatively easily address the biexciton state without, for example, the need for cross-polarization filtering to suppress the laser light, which would compromise the polarization state, source intensity, purity, and deterministic initialization. Noteworthy, the majority of recent reports found in the literature deal with the so-called binding biexciton case ($\Delta E_B > 0$). In a basic picture, higher order excitonic complexes in bulk, two- and one dimensional structures are always binding, as the binding energy is the result of Coulomb interactions and stable complexes can appear only at lower energy [12]. On the other hand, in zero-dimensional structures, geometrical constraints limit the space available for the charge carriers to redistribute due to Coulomb interaction [11, 13]. In specific cases, this can give rise to higher order complexes, so-called antibinding biexcitons, with $\Delta E_B < 0$. Such states have been observed in a number of cases [13–18]; however, no exhaustive experimental study concentrating on the specifications of the antibinding state resonant initialization had been reported before our group work.

To address an antibinding biexciton by a resonant two-photon excitation, the laser energy has to be detuned positively from an exciton by $\Delta E_B/2$. As we will show later, this can lead to very different QD population dynamics, which, unfortunately,

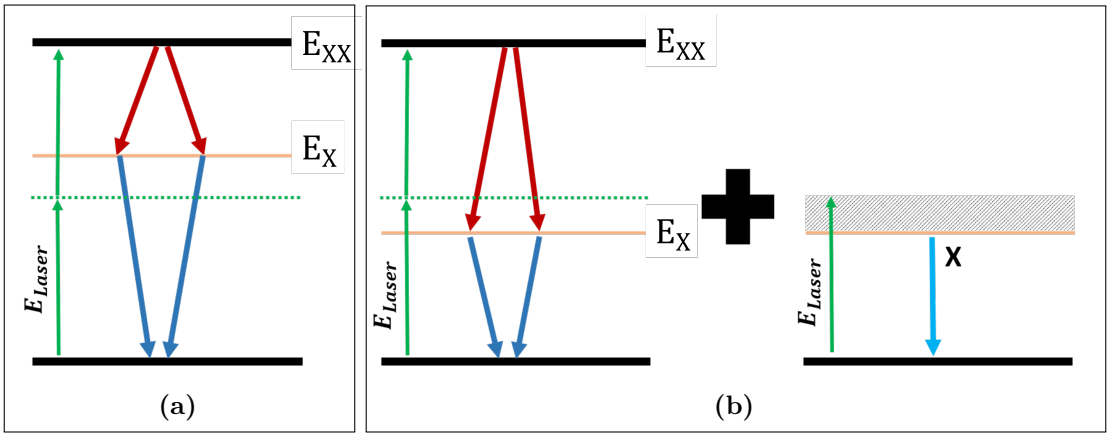


Figure 2.1: Two-photon excitation schema in QDs with different types of biexcitons (XX). **(a)** A binding biexciton two-photon excitation (TPE). **(b)** An antibinding biexciton TPE competing with the phonon-assisted exciton (X) population.

might not necessarily produce a favorable outcome for QDs with an antibinding biexciton in the contest of quantum information processing. Schematically, this population and recombination complexity is outlined in Figure 2.1b . As it can be seen in the the figure, in parallel to the expected two-photon excitation of a biexciton, conditions to excite an exciton state through the interaction with acoustic phonons can occur, i.e. a single photon can give some of its energy to acoustic phonons and utilize the rest to excite only the exciton state. A systematic experimental evidence of this complex dynamics is detailed in the following. As a case study, we have selected an $In_{0.25}Ga_{0.75}As/GaAs$ site-controlled pyramidal QD system. All single QDs from this QD family exceptionally possess antibinding biexcitons [19], making them an interesting playground for fundamental research of resonant excitation phenomena. Noteworthy, when two or more identical single $In_{0.25}Ga_{0.75}As/GaAs$ QDs are stacked with a nominal separator of $\leq$ 2nm, they form interacting or coupled-QD complexes with very different energetic structures [20]. Some of them are single QD-like, with a binding or even degenerate biexciton [21]; however, due to small binding energy (0.53 ± 0.47meV) and higher fine structure splitting values,

these QDs are less attractive candidates for resonant TPE experiments.

2.2 Experimetal Conditions

The QDs have been prepared by metalorganic vapor phase epitaxy (MOVPE) on (111)B-oriented GaAs substrates pre-patterned with 7.5μm tetrahedrons ensuring site control with the precision of a few nanometers—arguably an important advantage over self-assembled QD systems. $In_xGa_{1-x}As$ QDs with a nominal indium content of 0.25 were confined by GaAs. The most notable and attractive feature of these QDs is their high symmetry. An intrinsically highly symmetric (C_{3V} in group theory terms) carrier confinement potential, theoretically foreseen for all (111) direction grown QDs [22, 23] ensures a record density of QDs emitting polarization-entangled photon pairs under non-resonant optical [24] and electrical [25] excitation. QDs have been characterized in a micro-photoluminescence setup at 8 K in a closed-cycle helium cryocooler. Fourier transform limited 10 ps pulses have been pulse-shaped in a 4f (f = 0.5m) configuration with a portable tunable-width slit. The base 80 MHz 120 fs pulse width emission was from a tunable Ti:Sapphire laser. The laser emission was filtered with a series of 3 volume Bragg gratings utilized as narrow-band (0.3 nm) notch filters. Spectra have been taken by a CCD paired with a 1 m length monochromator with a 950 mm groove density ruled diffraction grating. The second-order correlation measurements [15] were taken by filtering exciton and biexciton transitions with two identical monochromators and utilizing single-photon avalanche photo detectors with dark counts of around 40 per second.

2.3 Experimental Results

In this section, we will describe the experimental results built upon the above mentioned theories and experimental conditions.

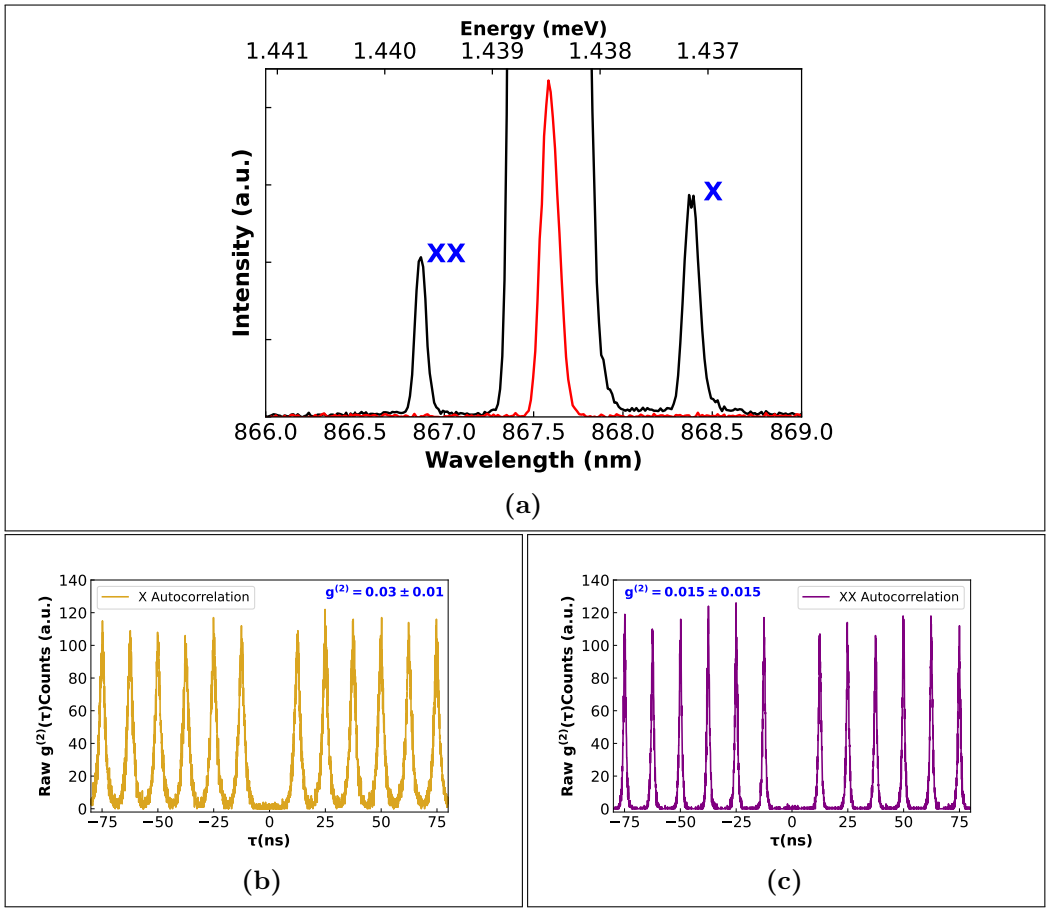


Figure 2.2: **(a)** The spectrum under TPE excitation with 10 ps pulses (red curve). **(b)** and **(c)** show the second order auto-correlation curves of the exciton (X) and biexciton (XX) transitions.

2.3.1 Two Photon Resonant Excitation (TPE)

Figure 2.2a shows a QD spectrum (ΔE_B=-2.5meV) obtained under two-photon excitation tuned resonantly to the biexciton state. The observation of the biexciton peak confirmed the possibility to excite QDs with an antibinding state resonantly. Autocorrelation of both, an exciton and biexciton, transitions showed clear anti-bunching in the second order (intensity) correlation curves, confirming high-quality single-photon emission from both lines. The measured values of $g^{(2)}(0)$ in the representative case (Figure 2.2b and Figure 2.2c) were rather low, i.e., 0.03 ± 0.01

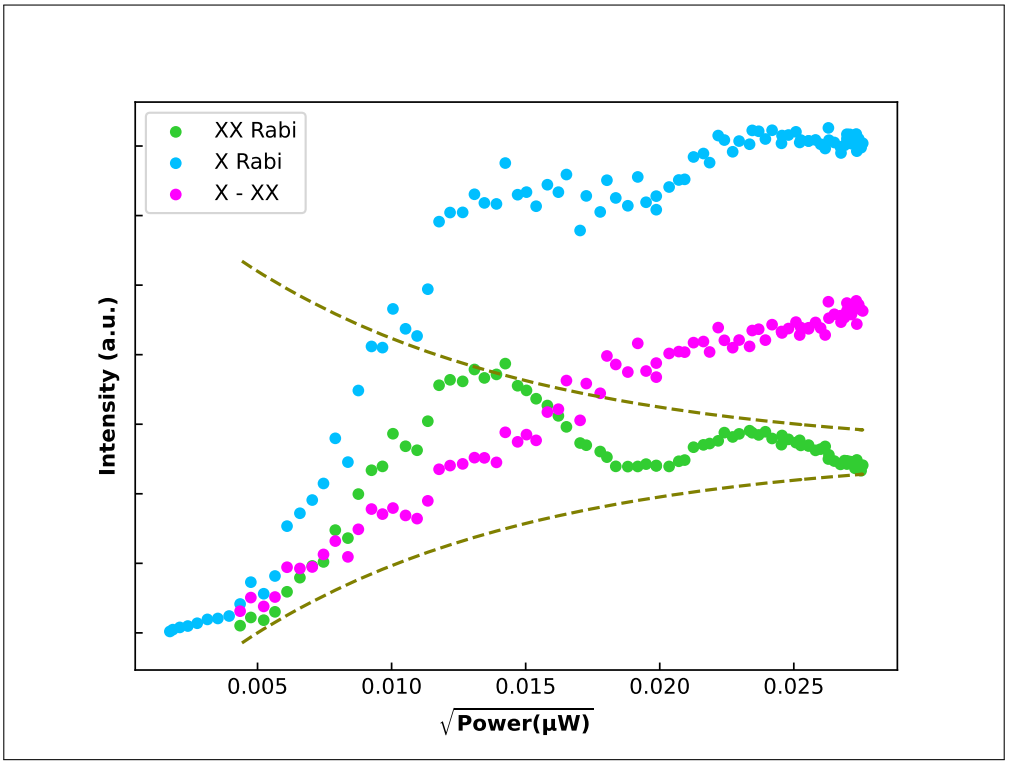


Figure 2.3: Excitation power dependence. The dashed lines are the envelopes of the damped Rabi oscillations. The X-XX curve is the difference between the exciton and biexciton intensity at the same excitation power. These are photoluminescence events occurring due to the phonon-assisted exciton population, which do not originate in the biexciton-exciton recombination cascade.The curves are represented not explicitly normalised to the dot population to allow an easier comparison of the different events. In an ideal case, the biexciton population maximum intensity would correspond to its 100 per cent occupancy

(X) and 0.015 ± 0.015 (XX).

2.3.2 Rabi Oscillations

Interestingly, we systematically observed clear asymmetries in the intensity of X and XX transitions, indicating substantially different population probabilities of the two states—a rather unexpected result for a state recombining in a cascade event.

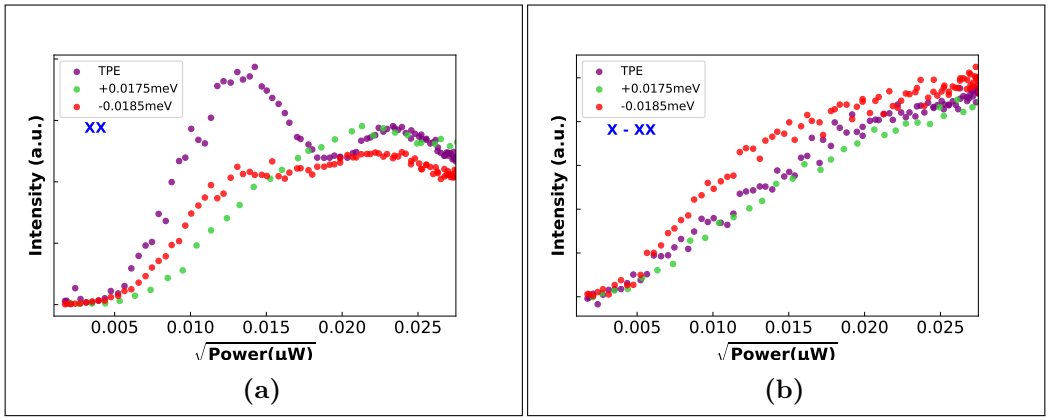


Figure 2.4: Power dependence of the biexciton and phonon-assisted exciton emission under different laser energy tuning conditions.

To understand the origins, we took the excitation power-dependent measurements presented in Figure 2.3. Characteristic Rabi oscillations of the excited level (XX) population were observed proving the coherent nature of the process. We attribute the damping to typical dephasing mechanisms, such as dephasing due to phonons at high excitation power. As damping processes typically stabilize the population around 0.5, we estimate that at a π area pulse, the maximum achieved population probability of the biexciton state is 0.65, where the remaining 0.35 population is because of the phonon-assisted exciton initialization discussed below. Small laser energy detuning of +0.175 meV and -0.185 meV was sufficient to eliminate the coherent population and shift it toward a phonon assisted excitation of the biexciton state process. As can be seen from Figure 2.4, the coherent nature of the state initialization characterized by Rabi oscillations is compromised, and the biexciton initialization, in analogy to the exciton case, is expected to be induced via phonons [26, 27], X-XX intensity changes can be attributed to different phonon density distribution.

The exciton, on the other hand, showed a different dependence. While a small oscillation correlated with the biexciton one was observed, an overall emission inten-

sity growth was obtained in the whole power range. This can be predicted in view of the complex mechanism expected for populating an antibinding biexciton case. Specifically, two phenomena are contributing to the intensity of the exciton—(1) photons coming from the biexciton recombination cascade and (2) photons coming from the exciton state that is excited non-resonantly and incoherently [6] through the acoustic phonon bath. The measured intensity is the integrated signal of both. Clear antibunching in the second-order correlation curve suggests that both are taking place during different excitation cycles. To discriminate the contribution of each, we assume, for simplicity, that the exciton population from the cascade is equal to the population of the biexciton. The subtracted result would represent the phonon-assisted X population showing monotonic growth. This is in good agreement with theoretically expected and experimentally observed results for an exciton-only excitation [5, 6]. To achieve high population values, this incoherent population process through a phonon-dressed state requires achieving a trade-off between the laser electric field strength and the state preparation time defined by the laser pulse length [27]. This scheme can provide a very robust way of state preparation once realized. The general principle applies for both, the exciton and biexciton, states. Figure 2.5 shows the phonon-assisted population as a function of laser detuning.

2.3.3 Auto-correlation

The second-order auto-correlation measurements evidently reveal that the two QD excitation scenarios are competing and do not occur within the same excitation cycle ($g_X^{(2)}(0) = 0.03 \pm 0.01$). It is an expected result as, with a probability dependent on the excitation conditions, a QD is excited either to the exciton or biexciton state—the population of one state blocks the population of the other. Provided that both processes can occur within the timescale of the laser pulse length in

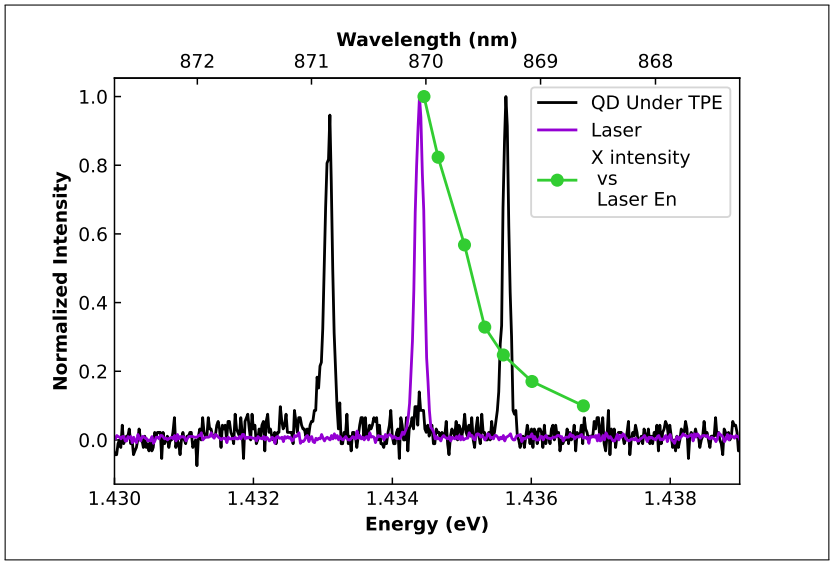


Figure 2.5: The exciton intensity dependence as a function of a laser pulse energy detuning. The spectrum is linearly polarized in a way to transmit photons originating from the biexciton recombination cascade only.

general, re-excitation of a QD becomes unlikely and results in low $g^{(2)}(0)$ values of the exciton state. While such a two-channel excitation-recombination mechanism creates deterministic state preparation issues, it does not prevent the detection of photons originated solely during the biexciton recombination cascade. These photons are of primary interest due to the expected polarization entanglement. To measure polarization entanglement of these pairs of photons, the biexciton photon was used to herald the exciton photon originated in the recombination cascade. By correlating them, second-order cross correlation curves were obtained. Twelve polarization-resolved measurements have been made to obtain full sets of two-photon polarization states in linear, diagonal, and circular bases (Figure 2.6). Every individual curve has been integrated for the same duration, i.e. 10 min, to ensure a valid data processing procedure as the raw detection events triggered only by the same excitation pulse have been considered (±6 ns range). Raw detection counts (given in Figure 2.6) were used as the two-photon polarization state intensity.

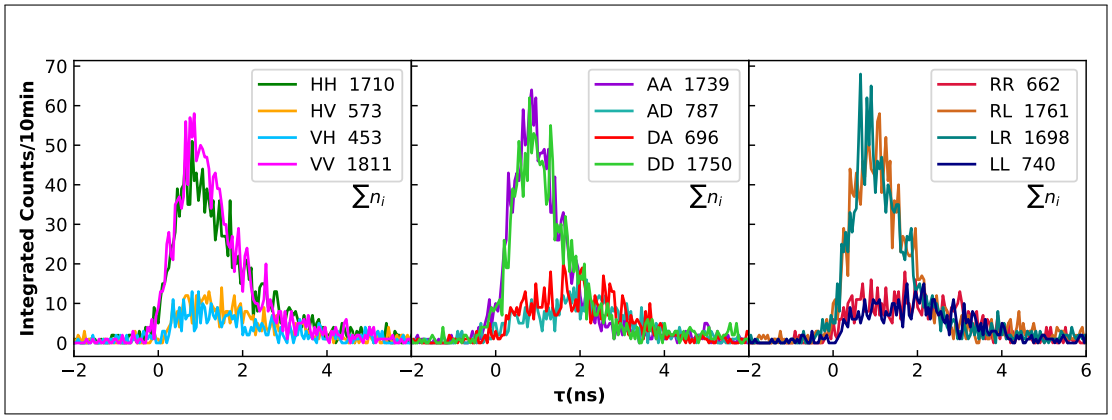


Figure 2.6: Polarization entanglement between the photons emitted during the biexciton-exciton recombination cascade. Full measurements in linear, diagonal, and circular polarization bases. The fine-structure splitting of the representative QD is $0.4 \pm 0.4 \mu eV$.

Figure 2.7a shows linear polarization analysis of the exciton and biexciton transition. As we discuss in [28], exciton photons created by phonon-assisted excitation are strongly polarized as the laser polarization state is directly mapped onto the spin state of the exciton. Being strongly polarized, phonon-assisted events invalidate the conventional normalization procedure to calculate the second-order correlation function value as an intensity of the projected two-photon polarization state. For example, Figure 2.7b shows a comparison of correlation curves between horizontally and vertically co-polarized biexciton and exciton photons. While the $g^{(2)}(0)$ peak is composed of events originating only from the biexciton and exciton recombination cascade, the side (uncorrelated) peaks arise due to contributions from all the events. As shown, horizontally polarized exciton photons originating from phonon-assisted excitation paths increase the side peak intensity nearly twice. Conventionally, when the source is not polarized, the two-photon polarization state intensity is obtained by normalizing the $g^{(2)}(0)$ peak using an average value of the side peak integrated intensity. However, this method is only valid when the source is not-polarized.

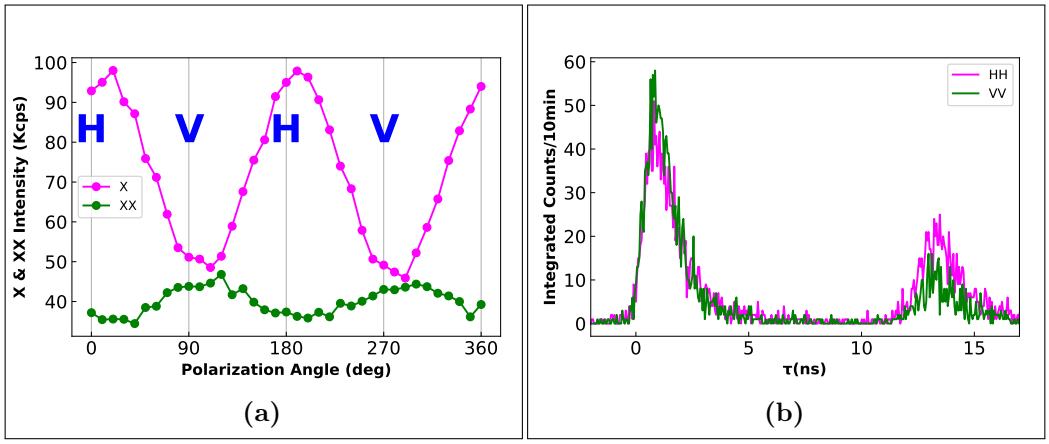


Figure 2.7: Polarization-resolved $g^{(2)}(\tau)$ **(a)** Linear polarization analysis of exciton and biexciton transitions. **(b)** Comparison of correlation curves between horizontally and vertically co-polarized biexciton and exciton photons.

Table 2.1

P.B.	$g^{(2)}(0)$	$\sum n_i$	P.B.	$g^{(2)}(0)$	$\sum n_i$	P.B.	$g^{(2)}(0)$	$\sum n_i$
HH	1.77	1710	**DD**	2.47	1750	**RR**	0.94	622
HV	0.92	573	**DA**	0.95	696	**RL**	1.82	1761
VV	3.65	1811	**AA**	1.89	1739	**LL**	0.81	740
VH	0.53	453	**AD**	1.04	787	**LR**	2.22	1698
Sum	6.87	4547		6.35	4972		5.79	4821

Table 2.1: Two-photon polarization state intensity: $g^{(2)}(0)$ vs raw counts.

To overcome this issue, every individual curve has been integrated for the same duration, i.e. 10 minutes, and raw detection counts of the $g^{(2)}(0)$ peak were used as the two-photon polarization state intensity. The comparison of the two-photon polarization state intensity obtained by the two methods is shown in the Table 2.1.

The biexciton-exciton photon pair entanglement has been estimated by calculating the fidelity to the expected, maximally entangled Bell's state $\frac{1}{\sqrt{2}}(|HH\rangle + |VV\rangle)$:

$$f = \frac{1}{4}(1 + S_{33} + S_{11} - S_{22} + S_{30} + S_{03}) \tag{2.1}$$

where S_{ii} are the two-photon Stokes parameters [29]. If the QD source is ideal, non-polarized, $S_{30} = S_{03} = 0$, and S_{33}, S_{11} and S_{22} conventionally represent degrees of correlation in linear, diagonal, and circular bases, respectively [30]. In our representative case, we obtained $S_{33} = 0.549$, $S_{11} = 0.403$, $S_{22} = 0.435$, $S_{30} = 0.004$ and $S_{03} = 0.049$, yielding the fidelity value of $f = 0.586 \pm 0.004$ The value exceeding 0.5 is considered a clear indicator of entanglement ($f \in [0, 1]$), even if the absolute fidelity value is far from some recently achieved records [31]. The fidelity threshold $f > 0.5$ stems from the separability of two states. Fidelity to specific state, in general, is defined as $f = \langle\Psi|\,\rho\,|\Psi\rangle$, Ψ being a pure state and ρ being the density matrix of a state. When comparing a given state ρ with a pure state (e.g. Bell state), if the given state is separable/classical mixture (knowing the state of one qubit gives no information about the state of the other), the fidelity won't exceed 0.5. For example if we consider density matrix made of two separable states $|HH\rangle$ and $|VV\rangle$ as below described, the fidelity to the entangled state $\frac{1}{\sqrt{2}}(|HH\rangle + |VV\rangle)$ will only reach 0.5.

$$\rho_{\text{Total}} = \frac{1}{2}(\rho_1 + \rho_2) = \frac{1}{2}\Big(|HH\rangle\langle HH| + |VV\rangle\langle VV|\Big)$$
$$f = \frac{1}{2}\Big(\langle HH| + \langle VV|\Big)\rho\Big(|HH\rangle + |VV\rangle\Big) = 0.5 \tag{2.2}$$

The main entanglement degradation reason can be attributed to the usual cross-dephasing events that destroy the recombination cascade coherence. Indeed, a QD with a very small fine-structure splitting ($0.4 \pm 0.4\mu$eV) and pure single photon emission, ideally, should emit pairs with a higher degree of entanglement. However, we systematically observed that these QDs under resonant excitation, in contrast to other types of QDs, maintain a relatively slow (0.78 ns ± 0.04 ns in this specific case) exciton lifetime (will be detailed in the following), which is sufficient to increase a cross-dephasing probability substantially [32].

The intrinsic lifetimes of the biexciton and exciton were extracted from the second order correlation measurements, by correlating two APD signals (the conventional Hanbury Brown-Twiss arrangement) and deconvoluting the corresponding state population function. The extracted biexciton lifetime was found to be 0.44 ns ± 0.03 ns in the representative case studied. As the state is created coherently by the laser, we deconvoluted the measured instrument response function (IRF) – using the autocorrelation signal of the 10 ps pulse laser – from the correlation curve of the laser and the biexciton photons (Figure 2.8(a)). The intrinsic exciton lifetime, on the other hand, cannot be extracted using similar correlations. While typically a lifetime trace is defined as a histogram of correlated events between a fast electric laser synchronisation signal (or an optical laser signal like in our case) and the transition of interest, such measurement not necessarily can directly provide the intrinsic lifetime of the state. In our case, the measured trace is the result of a convolution between the biexciton decay function and the exciton decay. After deconvoluting the biexciton state, we extracted an exciton lifetime of 0.77 ns ± 0.04 ns (Figure 2.8(b)). However, in this particular case, extra care has to be taken because, due to the presence of phonon-assisted events, the exciton population function is either from the laser or from the biexciton decay. To rule out the contribution of phonon-assisted events, the exciton lifetime can be reliably extracted from the $g^{(2)}(0)$ peak of the correlation curve obtained between the biexciton and exciton cascade. The $g^{(2)}(0)$ peak is composed of correlation events originating only from the biexciton-exciton recombination cascade events, and it is only convoluted with the IRF (Figure 2.8(c)). After the deconvolution procedure, we obtained the exciton lifetime of 0.78 ns, close enough to our previous result. One of the most prominent decoherence mechanisms can be attributed to processing-induced defect states within the bandgap, which can be excited even with the laser tuned to the TPE resonance. The presence of such charge trapping states and destructive

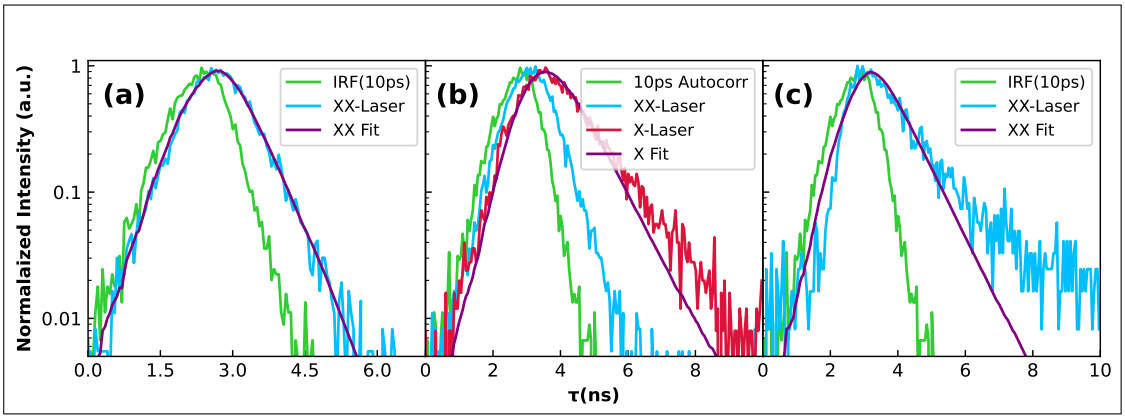


Figure 2.8: Lifetime extraction. **(a)** The biexciton-laser correlation; $\tau_{xx} = 0.44\text{ns} \pm 0.03\text{ns}$. **(b)** Correlations with the laser signal; $\tau_x = 0.77\text{ns} \pm 0.04\text{ns}$. **(c)** Exciton lifetime from the biexciton-exciton recombination cascade, i.e. the $g^{(2)}(0)$ peak; $\tau_x = 0.78\text{ns} \pm 0.04\text{ns}$.

effects on optical properties of QDs from the same sample have been demonstrated previously [19]. In agreement with this, a significant linewidth broadening— by spectral wandering—of the exciton (160μeV) and biexciton (117μeV) in the here discussed representative case even under TPE proves the existence of a dynamically charged QD environment. Moreover, and in general, under non-resonant excitation conditions, these trapping states are also the main reason for poor single photon emission, linewidth broadening, and QD charging. Thus, results obtained under non-resonant excitation appeared of little interest in the context of this work, and they were not taken for comparison.

Systematic polarization-resolved measurements revealed that the polarization states of photons emitted due to direct phonon-assisted excitation are strongly dependent on the polarization state of the laser. While being the matter of a broader dedicated study in the future, our preliminary observations suggest that the laser polarization state can be mapped on the polarization state of the exciton photon depending on the QD's energetic structure. A demonstration of the phenomenon using the same representative QD as it is shown in Figure 2.9. TPE is typically

performed using a linearly polarized laser to overcome Pauli exclusion principle (in the following, we show that the biexciton excitation channel can be effectively suppressed, as expected, with circularly co-polarized photons). Such excitation can efficiently excite the conventional biexciton state, which then recombines in a cascade. The XX curve in Figure 2.9 represents these events. The distribution of linear polarization components here has been analyzed by rotating a half-waveplate placed in front of a fixed polarizer at the entrance of the monochromator. Small modulation in the XX intensity is characteristic of this QD and is in good agreement with the two-photon Stokes parameters' measurements, showing that this QD source is slightly polarized. We tentatively attribute this polarization dependence to a weak mixing of heavy and light holes [33], which can vary in different QDs. The intensity of X events exceeding XX can be assigned to the phonon-assisted initialization of the exciton state (which will refer to as X-XX, i.e., X minus XX). In the case depicted in Figure 2.9, these events are fully linearly polarized. The analysed laser intensity is also plotted to show that the polarization state of X-XX photons is nearly identical to the laser's one. The second-order auto-correlation measurement of the X transition [the antibunching $g^{(2)}(\tau)$ curve shown in the inset of Figure 2.9] clearly confirmed that the source is fully described by a subPoissonian statistics, and it is not laser-related. By rotating the laser polarization by 45 (not shown), the X-XX maximum also shifted, with a just slightly different phase offset from the one visible in Figure 2.9, confirming the existence of a correlation function between the polarization states of the laser and X photons created by phonon-assisted excitation.

We checked also another issue – the suppression of the biexciton recombination cascade which should be achieved utilising circularly polarized excitation light (Figure 2.10b). Because of transition selection rules (which are similar to atomistic ones between P and S states), TPE processes of the biexciton by circularly co-

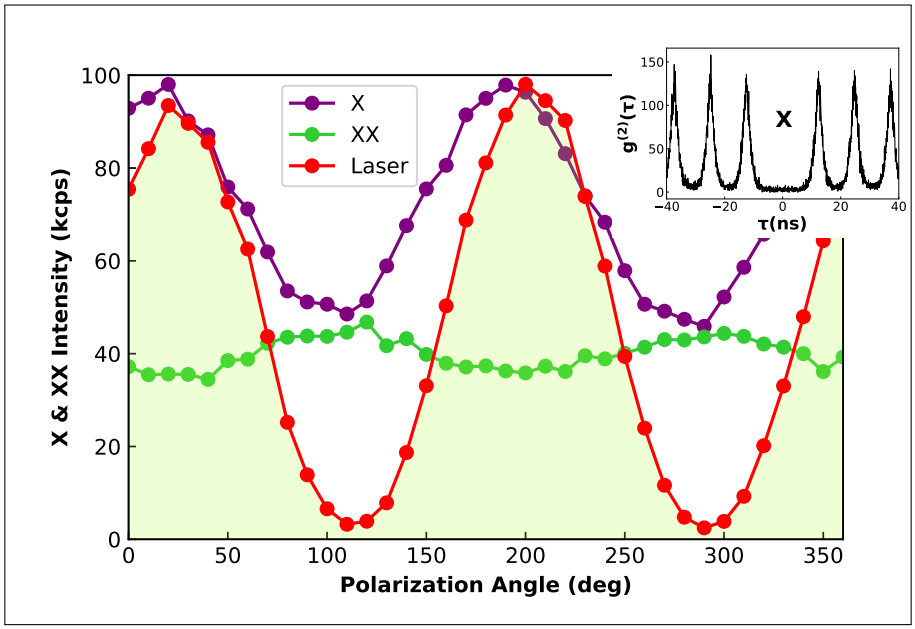


Figure 2.9: Linear polarization analysis of the detected light originating from the laser, exciton, and biexciton.The inset shows an antibunching curve collected from the exciton transition.

polarized photons are fundamentally forbidden. We indeed observe a strong suppression of the biexciton state. The experimentally observed weak signal from the biexciton in Figure 2.10b can be attributed to a non-perfect preparation of the laser polarization state. Otherwise, in an ideal case, the laser light couples only to the exciton state. As the electron-phonon interaction is spin independent, the polarization state of the laser is initially mapped on the Bloch sphere of the exciton, which, in the presence of a fine-structure splitting, starts to precess. Figure 2.10a shows linear polarization behaviour for the exciton photons. The non-uniform distribution of linear polarization components indicates that the polarization state of the ensemble of photons is not purely circularly polarized due to the FSS of a few μeV in that specific dot.

While it might seem that an antibinding biexciton is a fundamental limitation in the resonant TPE approach, as true deterministic generation of non-classical

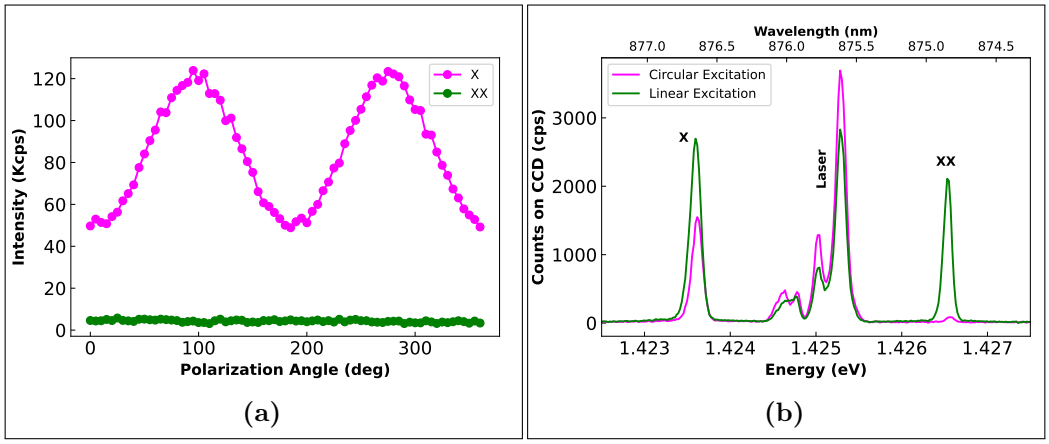


Figure 2.10: **(a)** QD photoluminescence under circularly polarized TPE showing strong suppression of the biexciton recombination cascade. Here a different QD was used than the one discussed in the main text. **(b)** Comparison of non-polarized spectra obtained under circularly and linearly polarized laser light tuned to the TPE resonance (π pulse area for the biexciton transition).

light becomes compromised, it is worth pointing to a single reported case in the literature [34], which suggests that under certain conditions, the TPE process actually can be the only excitation phenomenon (no phonon-assisted excitons) despite an antibinding biexciton. It is possible indeed that the TPE process is strongly affected by QD coupling to a cavity or it is highly dependent on the excitation conditions; as in Ref [34], the authors do not discuss nor observe any issue with the excitonic configuration. A known phenomenon of a strongly reduced excitation power needed to populate cavity-coupled QDs has been observed in the same type of device (200 times reduction in comparison to QDs in a slab) [35]. It is possible that a weak laser field strength, which, in general, is driving an exciton coupling to the acoustic phonon bath and is not sufficient to populate the exciton state efficiently during the few picoseconds of the excitation. To achieve a significant phonon-assisted exciton state population with a weak laser field, long preparation times (pulse duration), far exceeding the demonstrated very short lifetime (66 ps) of the biexciton, would be required [27, 36]. That kind of microcavity-based device

driven by short (a few ps) pulses, in principle, is expected to be robust against phonon-assisted excitation under TPE conditions. Experimental evidence, even though with a binding biexciton, shows that a reduced laser pulse length (from 13ps to 7ps) does not affect the state population by resonant TPE; however, short pulses are less efficient in the phonon-induced biexciton state population [37]. We, unfortunately, could not reliably verify this in our experiment due to a rather small binding energy (2 meV) and the high excitation powers needed, which were causing problems due to stray laser light.

2.4 Summary and Conclusions

In summary, we have demonstrated the population of site-controlled pyramidal QD biexciton states by two-photon excitation. High-quality single photon emission and good polarization entanglement between the photons emitted through the biexciton recombination cascade were measured. In all the presented cases, we have been dealing with antibinding biexcitons. We showed that this specific fine-structure QD configuration leads to a complex excitation recombination scenario. It was found that the laser tuned close to a two-photon resonance could populate the exciton state through the acoustic phonon side band. The latter excitation is less significant at low excitation powers, specifically at the exact resonance condition with a π area pulse. However, as the two phenomena are competing, the true deterministic photon emission is compromised, at least in our $In_{0.25}Ga_{0.75}As$ QD system. On the other hand, there is no obvious reason why this phenomenon should not be observed in the other types of epitaxial QDs under similar and thus at the moment typical, excitation conditions. The scientific community members aiming to utilize QDs with antibinding biexcitons should be taking into account the findings presented in this work. To exploit the full potential of our

highly symmetric site-controlled QDs, a different resonant excitation approach or conditions might be needed. Among possible candidates are phonon-assisted two-photon excitation energetically tuned above the biexciton transition [27] (the feasibility of this experiment is shown in Figure 2.5) and a variation of dichromatic wavelength excitation [38]. Also, a comprehensive study of different excitation conditions, such as the pulse length, pulse area, and effect of a microcavity, could provide the solution to the compromised deterministic biexciton initialization. A here highlighted case presented by Wang et al. [34] is in agreement with the theory of phonon-assisted state preparation both suggesting that the phonon-induced population can be suppressed or minimized by designing devices that can be driven by low power and short (a few picoseconds) pulses. Finally, we observed strong correlations between polarization states of the laser and the exciton populated directly with phonon assistance. Our preliminary findings show that the laser state can be mapped on the exciton photon and will be the subject of further studies.

Bibliography

[1] A. Zrenner, E. Beham, S. Stufler, F. Findeis, M. Bichler, and G. Abstreiter, "Coherent properties of a two-level system based on a quantum-dot photodiode," *Nature*, vol. 418, pp. 612–614, Aug. 2002.

[2] S. Stufler, P. Machnikowski, P. Ester, M. Bichler, V. M. Axt, T. Kuhn, and A. Zrenner, "Two-photon rabi oscillations in a single $In_xGa_{1-x}As$/GaAs quantum dot," *Phys. Rev. B*, vol. 73, p. 125304, Mar 2006.

[3] C.-M. Simon, T. Belhadj, B. Chatel, T. Amand, P. Renucci, A. Lemaitre, O. Krebs, P. A. Dalgarno, R. J. Warburton, X. Marie, and B. Urbaszek, "Robust quantum dot exciton generation via adiabatic passage with frequency-swept optical pulses," *Phys. Rev. Lett.*, vol. 106, p. 166801, Apr 2011.

[4] T. Kaldewey, S. Lüker, A. V. Kuhlmann, S. R. Valentin, A. Ludwig, A. D. Wieck, D. E. Reiter, T. Kuhn, and R. J. Warburton, "Coherent and robust high-fidelity generation of a biexciton in a quantum dot by rapid adiabatic passage," *Phys. Rev. B*, vol. 95, p. 161302, Apr 2017.

[5] M. Glässl, A. M. Barth, and V. M. Axt, "Proposed robust and high-fidelity preparation of excitons and biexcitons in semiconductor quantum dots making active use of phonons," *Phys. Rev. Lett.*, vol. 110, p. 147401, Apr 2013.

[6] J. H. Quilter, A. J. Brash, F. Liu, M. Glässl, A. M. Barth, V. M. Axt, A. J. Ramsay, M. S. Skolnick, and A. M. Fox, "Phonon-assisted population inversion of a single InGaAs/GaAs quantum dot by pulsed laser excitation," *Phys. Rev. Lett.*, vol. 114, p. 137401, Mar 2015.

[7] P.-L. Ardelt, L. Hanschke, K. A. Fischer, K. Müller, A. Kleinkauf, M. Koller, A. Bechtold, T. Simmet, J. Wierzbowski, H. Riedl, G. Abstreiter, and J. J. Finley, "Dissipative preparation of the exciton and biexciton in self-assembled quantum dots on picosecond time scales," *Phys. Rev. B*, vol. 90, p. 241404, Dec 2014.

[8] M. Müller, S. Bounouar, K. D. Jöns, M. Glässl, and P. Michler, "On-demand generation of indistinguishable polarization-entangled photon pairs," *Nature Photonics*, vol. 8, pp. 224–228, Mar. 2014.

[9] E. Schöll, L. Hanschke, L. Schweickert, K. D. Zeuner, M. Reindl, S. F. Covre da Silva, T. Lettner, R. Trotta, J. J. Finley, K. Müller, A. Rastelli, V. Zwiller, and K. D. Jöns, "Resonance fluorescence of gaas quantum dots with near-unity photon indistinguishability," *Nano Letters*, vol. 19, no. 4, pp. 2404–2410, 2019.

[10] L. Schweickert, K. D. Jöns, K. D. Zeuner, S. F. Covre da Silva, H. Huang, T. Lettner, M. Reindl, J. Zichi, R. Trotta, A. Rastelli, and V. Zwiller, "On-demand generation of background-free single photons from a solid-state source," *Applied Physics Letters*, vol. 112, no. 9, p. 093106, 2018.

[11] A. Schliwa, M. Winkelnkemper, and D. Bimberg, "Few-particle energies versus geometry and composition of InGaAs/GaAs self-organized quantum dots," *Phys. Rev. B*, vol. 79, p. 075443, Feb 2009.

[12] S. Rodt, A. Schliwa, R. Heitz, V. Türck, O. Stier, R. Sellin, M. Strassburg, U. Pohl, and D. Bimberg, "Few-particle effects in self-organized quantum dots," *physica status solidi (b)*, vol. 234, no. 1, pp. 354–367, 2002.

[13] S. Rodt, R. Heitz, A. Schliwa, R. L. Sellin, F. Guffarth, and D. Bimberg, "Repulsive exciton-exciton interaction in quantum dots," *Phys. Rev. B*, vol. 68, p. 035331, Jul 2003.

[14] L. Landin, M. S. Miller, M.-E. Pistol, C. E. Pryor, and L. Samuelson, "Optical studies of individual inas quantum dots in gaas: Few-particle effects," *Science*, vol. 280, no. 5361, pp. 262–264, 1998.

[15] E. Moreau, I. Robert, L. Manin, V. Thierry-Mieg, J. M. Gérard, and I. Abram, "Quantum cascade of photons in semiconductor quantum dots," *Phys. Rev. Lett.*, vol. 87, p. 183601, Oct 2001.

[16] Z. Yuan, B. E. Kardynal, R. M. Stevenson, A. J. Shields, C. J. Lobo, K. Cooper, N. S. Beattie, D. A. Ritchie, and M. Pepper, "Electrically driven single-photon source," *Science*, vol. 295, no. 5552, pp. 102–105, 2002.

[17] J. Claudon, J. Bleuse, N. S. Malik, M. Bazin, P. Jaffrennou, N. Gregersen, C. Sauvan, P. Lalanne, and J.-M. Gérard, "A highly efficient single-photon source based on a quantum dot in a photonic nanowire," *Nature Photonics*, vol. 4, pp. 174–177, Mar. 2010.

[18] T. Heindel, A. Thoma, M. von Helversen, M. Schmidt, A. Schlehahn, M. Gschrey, P. Schnauber, J. H. Schulze, A. Strittmatter, J. Beyer, S. Rodt, A. Carmele, A. Knorr, and S. Reitzenstein, "A bright triggered twin-photon source in the solid state," *Nature Communications*, vol. 8, p. 14870, Apr. 2017.

[19] G. Juska, E. Murray, V. Dimastrodonato, T. H. Chung, S. T. Moroni, A. Gocalinska, and E. Pelucchi, "Conditions for entangled photon emission from (111)b site-controlled pyramidal quantum dots," *Journal of Applied Physics*, vol. 117, no. 13, p. 134302, 2015.

[20] S. T. Moroni, T. H. Chung, G. Juska, A. Gocalinska, and E. Pelucchi, "Statistical study of stacked/coupled site-controlled pyramidal quantum dots and their excitonic properties," *Applied Physics Letters*, vol. 111, no. 8, p. 083103, 2017.

[21] "Vanishing biexciton binding energy from stacked, movpe grown, site-controlled pyramidal quantum dots for twin photon generation," *Journal of Crystal Growth*, vol. 506, pp. 36–39, 2019.

[22] T. Kuroda, T. Mano, N. Ha, H. Nakajima, H. Kumano, B. Urbaszek, M. Jo, M. Abbarchi, Y. Sakuma, K. Sakoda, I. Suemune, X. Marie, and T. Amand, "Symmetric quantum dots as efficient sources of highly entangled photons: Violation of bell's inequality without spectral and temporal filtering," *Phys. Rev. B*, vol. 88, p. 041306, Jul 2013.

[23] M. A. M. Versteegh, M. E. Reimer, K. D. Jöns, D. Dalacu, P. J. Poole, A. Gulinatti, A. Giudice, and V. Zwiller, "Observation of strongly entangled photon pairs from a nanowire quantum dot," *Nature Communications*, vol. 5, p. 5298, Dec. 2014.

[24] G. Juska, V. Dimastrodonato, L. O. Mereni, A. Gocalinska, and E. Pelucchi, "Towards quantum-dot arrays of entangled photon emitters," *Nature Photonics*, vol. 7, pp. 527–531, July 2013.

[25] T. H. Chung, G. Juska, S. T. Moroni, A. Pescaglini, A. Gocalinska, and E. Pelucchi, "Selective carrier injection into patterned arrays of pyramidal quantum dots for entangled photon light-emitting diodes," *Nature Photonics*, vol. 10, pp. 782–787, Dec. 2016.

[26] M. Reindl, K. D. Jöns, D. Huber, C. Schimpf, Y. Huo, V. Zwiller, A. Rastelli, and R. Trotta, "Phonon-assisted two-photon interference from remote quantum emitters," *Nano Letters*, vol. 17, no. 7, pp. 4090–4095, 2017. PMID: 28557459.

[27] A. M. Barth, S. Lüker, A. Vagov, D. E. Reiter, T. Kuhn, and V. M. Axt, "Fast and selective phonon-assisted state preparation of a quantum dot by adiabatic undressing," *Phys. Rev. B*, vol. 94, p. 045306, Jul 2016.

[28] G. Juska, I. Ranjbar Jahromi, F. Mattana, S. Varo, V. Dimastrodonato, and E. Pelucchi, "Biexciton initialization by two-photon excitation in site-controlled quantum dots: The complexity of the antibinding state case," *Applied Physics Letters*, vol. 117, no. 13, p. 134001, 2020.

[29] J. Altepeter, E. Jeffrey, and P. Kwiat, "Photonic state tomography," vol. 52 of *Advances In Atomic, Molecular, and Optical Physics*, pp. 105–159, Academic Press, 2005.

[30] A. J. Shields, R. M. Stevenson, and R. J. Young, *Entangled Photon Generation by Quantum Dots*, pp. 227–265. Berlin, Heidelberg: Springer Berlin Heidelberg, 2009.

[31] D. Huber, M. Reindl, S. F. Covre da Silva, C. Schimpf, J. Martín-Sánchez, H. Huang, G. Piredda, J. Edlinger, A. Rastelli, and R. Trotta, "Strain-tunable gaas quantum dot: A nearly dephasing-free source of entangled photon pairs on demand," *Phys. Rev. Lett.*, vol. 121, p. 033902, Jul 2018.

[32] A. J. Hudson, R. M. Stevenson, A. J. Bennett, R. J. Young, C. A. Nicoll, P. Atkinson, K. Cooper, D. A. Ritchie, and A. J. Shields, "Coherence of an entangled exciton-photon state," *Phys. Rev. Lett.*, vol. 99, p. 266802, Dec 2007.

[33] K. F. Karlsson, V. Troncale, D. Y. Oberli, A. Malko, E. Pelucchi, A. Rudra, and E. Kapon, "Optical polarization anisotropy and hole states in pyramidal quantum dots," *Applied Physics Letters*, vol. 89, no. 25, p. 251113, 2006.

[34] H. Wang, H. Hu, T.-H. Chung, J. Qin, X. Yang, J.-P. Li, R.-Z. Liu, H.-S. Zhong, Y.-M. He, X. Ding, Y.-H. Deng, Q. Dai, Y.-H. Huo, S. Höfling, C.-Y. Lu, and J.-W. Pan, "On-demand semiconductor source of entangled photons which simultaneously has high fidelity, efficiency, and indistinguishability," *Phys. Rev. Lett.*, vol. 122, p. 113602, Mar 2019.

[35] J. Liu, R. Su, Y. Wei, B. Yao, S. F. Silva, Y. Yu, J. Iles-Smith, K. Srinivasan, A. Rastelli, J. Li, and et al., "A solid-state source of strongly entangled photon pairs with high brightness and indistinguishability," *Nature Nanotechnology*, vol. 14, no. 6, p. 586–593, 2019.

[36] C. Gustin and S. Hughes, "Efficient pulse-excitation techniques for single photon sources from quantum dots in optical cavities," *Advanced Quantum Technologies*, vol. 3, no. 2, p. 1900073, 2019.

[37] S. Bounouar, M. Müller, A. M. Barth, M. Glässl, V. M. Axt, and P. Michler, "Phonon-assisted robust and deterministic two-photon biexciton preparation in a quantum dot," *Phys. Rev. B*, vol. 91, p. 161302, Apr 2015.

[38] S. Boyle, A. Ramsay, A. Fox, and M. Skolnick, "Two-color two-photon rabi oscillation of biexciton in single inas/gaas quantum dot," *Physica E: Low-dimensional Systems and Nanostructures*, vol. 42, no. 10, pp. 2485–2488, 2010. 14th International Conference on Modulated Semiconductor Structures.

Chapter 3

GaAs QDs

3.1 The Binding Biexciton

In the previous chapter we discussed the anti-binding XX in which the XX energy (E_{XX}) is higher than X energy (E_X). We showed that in this condition the TPE is not efficient due to the competing phonon assisted excitation of X state, a least for dots which are not inserted into cavities. This, however, is not the case in GaAs QDs, as we will detail in the following. They posses a binding ($E_X > E_{XX}$) excitonic complex, see Figure 3.1a, which makes the TPE more efficient [1, 2]. Historically GaAs QDs were among the first few configurations to be studied in the context of research in quantum technologies using semiconductor QDs. Due to a complex emission profile stemming from the above band excitation scheme (the only available scheme at the time), the XX-X transitions were embedded in a complex pattern as shown in Figure 3.1b. This made it hard to pinpoint XX-X transitions among many others. Later, thanks to the development of new excitation schemes, in particular TPE, and availability of better detectors (and marginally the associated better resolution), the GaAs QDs came back in interest as they are brighter (the carrier lifetime in GaAs quantum dots can be shorter, resulting in a faster radiative recombination that enhances the brightness under

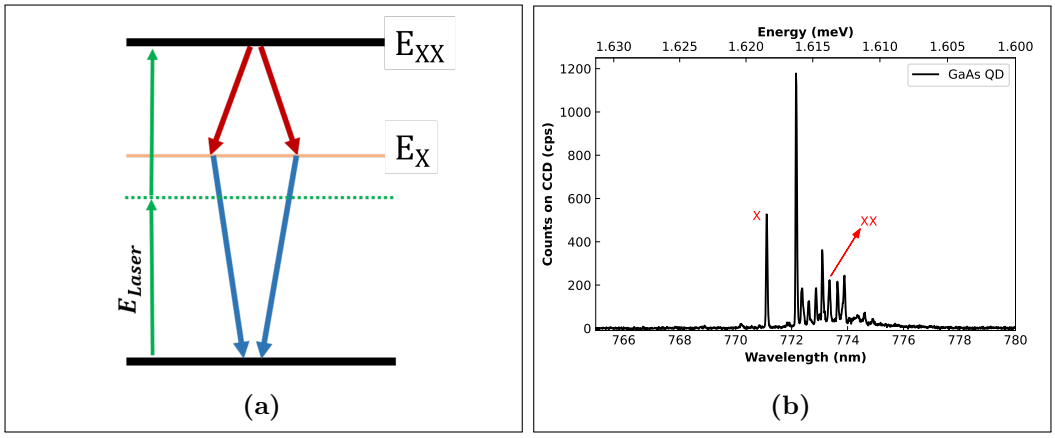


Figure 3.1: **(a)** A schematic diagram showing that binding biexciton, due to absence of phonon assisted exciton state excitation, is more efficient than antibinding biexciton **(b)** A typical GaAs QD spectrum. The XX transition is embedded among many other transitions once none-resonantly excited.

non-resonant pumping conditions), shorter in life time, less broad and, once resonantly pumped, a clear X-XX transition can be observed. For instance, the recently developed GaAs droplet epitaxy-based GaAs dots show similar excitonic patterns when above barrier excitation is exploited but have shown very clear excitonic patterns and short lifetimes when resonantly excited [3, 4]. These features, combined with the high structural symmetry of droplet etched dots, have led to the recent demonstrations of on-demand quantum teleportation and entanglement swapping with quantum emitters [5, 6]. Along with the interest back to the GaAs QD family, pure [7], one-demand, indistinguishable [8], entangled [9] and bright [10] GaAs QD photon sources were reported.

In general, different growth techniques have been devised for QDs including Stranski-Krastanov, droplet epitaxy and recently developed local droplet etching mostly relying on molecular beam epitaxy (MBE) method. And also generally speaking, none of the above mentioned state-of-the-art QD structures can easily and simultaneously check all requirements for quantum information processing and

integration with photonic chips. Site-control and spectral uniformity are often left untackled, for one. Effectively, also both the exciton and biexciton uniformity would be of paramount importance in an advanced quantum information device design with multiple sources of entangled photons [11]. In the case of $In_xGa_{1-x}As$ site-controlled pyramidal QDs, although a remarkable uniformity of neutral exciton states was observed, it is largely unmatched with the internal spectral uniformity of individual QDs [12] (we will compare and discuss with GaAs QDs in the following text to clarify better). These points motivated us to revamp the (pyramidal) GaAs QD system and provide a new generation of site-controlled pyramidal QDs. In our survey, we studied different dot configurations. We changed the QD and barrier thicknesses, alloy composition of barriers and different barrier designs (monolayer and superlattice structure). In the following, we will dissect each step of our survey. In section two, we first start with the growth considerations, different nanostructures appearing during the growth and their effect on the optical properties of QDs. This will help to justify each design strategy and eventually in section three we will discuss the corresponding experimental results of each design.

3.2 Growth

3.2.1 Growth Model

As guidance, we provide a summary of epitaxial growth on non-planar surfaces, and specifically, tetrahedral recesses. Growth on non-planar surfaces has several consequences. Among the most prominent ones are the formation of a self-limiting profile (a base for a quantum dot (QD) seeding), and alloy segregation effects. They define QD's geometry and confinement conditions, and can be substantially different than the nominal values defined for (100) planar surfaces. The model estimating the effective GaAs QD and $Al_xGa_{1-x}As$ confinement barrier properties

has been published elsewhere [13] and it is summarized below.

The model uses an inverted truncated cone retaining the essence of pattern that is the different growth rate at lateral facets and base reaching the so called "self-limiting" profile. A GaAs QD forms on this $Al_xGa_{1-x}As$ profile. In Figure 3.2a, the values of base diameter as a function of Aluminum (Al) content are shown in both experimental (red squares) and theoretical (solid blue line). Ga adatoms diffuse over longer distances than Al, so a higher Ga concentration can be expected to diffuse from the sidewalls toward the basal plane, whereupon the atoms can be promptly incorporated. This leads to an increased growth rate on the bottom facet, which is accompanied by a widening of the self-limiting profile as shown in the inset of Figure 3.2a. In part (b) of Figure 3.2 the effective and nominal Al content at the bottom of the pyramid are shown. This area is Ga enriched and forms the region called a vertical quantum wire (VQWr). This alloy contributes mostly to the confinement of a QD and so altering the symmetry and FSS. In Figure 3.2c there is an experimental evidence of the growth model showing that an increase in Al content can cause narrowing of the base and the marked VQWrs are formed along the vertical axis of the pyramid during the decomposition of $Al_xGa_{1-x}As$ due to Ga segregation for x= 0.2, 0.4 and 0.65 in layers 2a, 3a and 4a respectively.

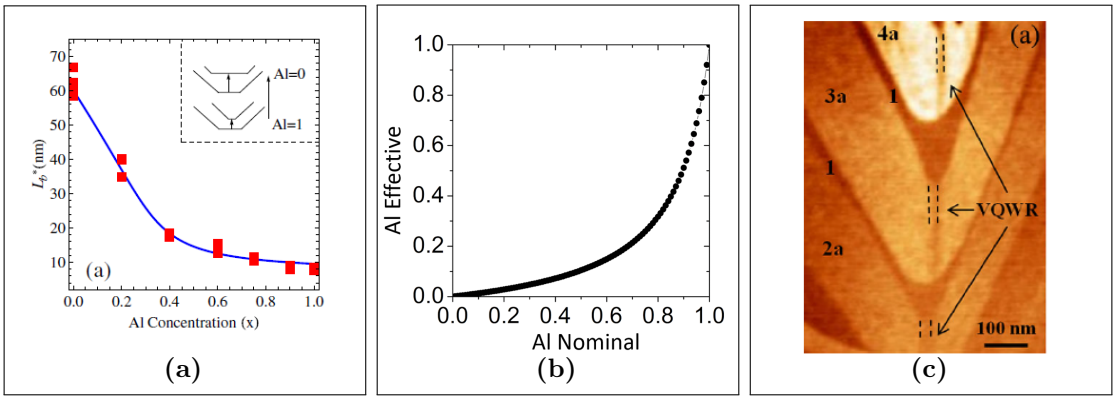


Figure 3.2: Growth model used to calculate the effect of Al content in self-limiting profile width during epitaxial growth over inverted tetrahedral pyramidal recesses. Images **(a)** and **(c)** are reproduced from V. Dimastrodonato et al, Phys. Rev. Lett. 2012, 108, 256102 with the permission of the American Physical Society Publishing

3.2.2 Sample Fabrication and Growth Configurations

QDs were grown by MOVPE on (111)B oriented GaAs substrates pre-patterned with either 7.5μm or 10μm pitch tetrahedrons. A general QD formation scheme is shown in Figure 3.3. A stack of epitaxial layers with a different functionality was grown. The key functional layers defining the QD properties are the confinement barriers and the active QD layer. Based on the barriers' composition and structure, two different approaches have been studied. In the first one, the barriers are composed of 10-100 nm thickness $Al_xGa_{1-x}As$, where the nominal Aluminum content has been set between 0.45 and 1, i.e. pure AlAs. In the second one, a superlattice composed of 25 (0.2 nm period) or 50 (0.1 nm period) AlAs/GaAs pairs was grown. We highlight that effective growth rates are known to be very different from nominal ones, a few times higher, as a function of recess and growth parameters. At this stage, we cannot provide exact structural measurements due to the complexity of microscopy studies in this system [14]. It should be highlighted that the growth on non-planar substrates is driven by anisotropic precursor decomposition (higher decomposition on (111)A facets than on (111)B

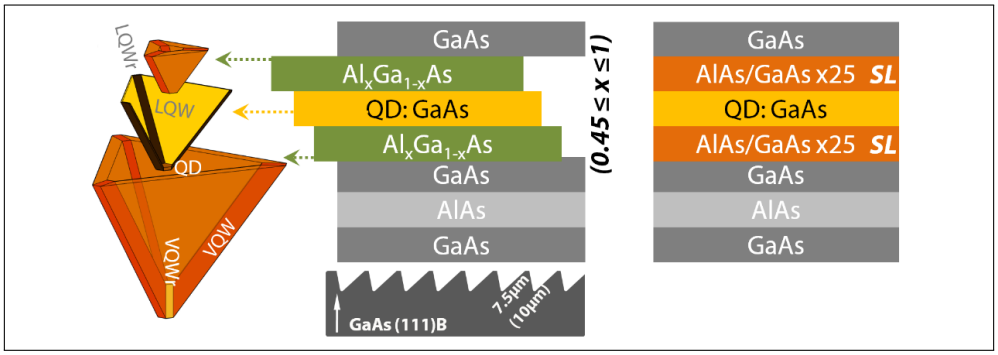


Figure 3.3: Schematics of the QD structure design. The sketch presents a complex ensemble of nanostructuring forming inside the pyramidal recesses. The epitaxial layer stacks show a generic QD layers' structure with two different designs for the confinement barriers: $Al_xGa_{1-x}As$ and Ga/Al digital alloy superlattice.

and consequential group III deposition anisotropies) which, together with mass-transfer effects, cause the formation of a complex ensemble of structures within the pyramidal recesses . Schematically these structures are sketched in Figure 3.3. Due to a longer Gallium diffusion length during AlGaAs deposition, several Gallium enriched regions develop: Three vertical quantum wells (VQW) and a vertical quantum wire (VQWr) along the central axis of the pyramid. The VQWr has the strongest effect on a QD confinement potential as the structure with the dominant contact area. The real Al concentration in a VQWr can be calculated from growth modeling as described above and summarized in Table 3.1b. The deposition of the GaAs QD active layer forms 3 different types of structures: 3 lateral quantum wells (LQWs), 3 lateral quantum wires (LQWr) and the QD located at the bottom of the recess. The nominal thickness of this layer has been set between 0.07 and 1nm for different samples.

We now give a short summary of growth configuration for different samples studied in this research. In Table 3.1a, the typical structure of multilayer epitaxial growth of GaAs/AlGaAs QDs is shown and the highlighted parameters are those being tuned in order to investigate the corresponding effect on emission profile.

Table 3.1a ($GaAs/Al_xGa_{1-x}As$)				
#	**Layer**	**Material**	**Al Concentration (%)**	**Thickness (nm)**
1	Buffer	GaAs		160
2	Etch Stop	AlAs		60
3	Contact	GaAs		50
4	Barrier1	$Al_xGa_{1-x}As$	**x**	100
5	QD	GaAs		**h**
6	Barrier2	$Al_xGa_{1-x}As$	**x**	70
7	Cap	GaAs		70

Table 3.1b ($GaAs/Al_xGa_{1-x}As$)						
Sample No	**1**	**2**	**3**	**4**	**5**	**6**
QD nominal thickness **h**(nm)	1	0.5	0.5	0.3	0.15	0.07
Nominal Al concentration **x**(%)	45	70	60	70	70	70
VQWr Al concentration **x**(%)	8	21	14	21	21	21

Table 3.1: A typical structure of multilayer epitaxial growth of GaAs/AlGaAs QDs. The colored parameters, are sumarized in Table 3.1b.A summary of different values of highlighted parameters of Table 3.1a for different samples

The growth direction is from Buffer (first epitaxially grown on pyramidal recesses) to Cap (the last layer grown). In Table 3.1b, there is a summary of different values of highlighted parameters of Table 3.1a for different samples.

As previously mentioned, different strategies were implemented to correct the FSS and also monitor the corresponding effects of tunings on the PL spectra. To this, we also grew GaAs/superlattice (GaAs/AlAs) and GaAs/AlAs structure. Generally, FSS stems from symmetry breaking of confinement potential of QD. As mentioned before, the VQWr has the dominant contact area with the QD and so alters the symmetry of confinement potential. VQWr is formed due to Ga segregation during

Table 3.2a (GaAs/superlattice)				
#	**Layer**	**Material**	**Al Concentration (%)**	**Thickness (nm)**
1	Buffer	GaAs		60
2	Etch Stop	AlAs		40
3	Contact	GaAs		100
4	Barrier1	$Al_xGa_{1-x}As$	55	70
5	Barrier2	$Al_xGa_{1-x}As$	45	90
6	Superlattice	GaAs/AlAs		10
7	QD	GaAs		**h**
8	Superlattice	GaAs/AlAs		10
9	Barrier1	$Al_xGa_{1-x}As$	45	60
10	Barrier2	$Al_xGa_{1-x}As$	55	90
11	Cap	GaAs		1

Table 3.2b (GaAs/superlattice)				
Sample No	**1**	**2**	**3**	**4**
QD nominal thickness **h**(nm)	0.65	0.85	0.65	0.85
Superlattice properties	25x T=0.2nm	25x T=0.2nm	25x T=0.1nm	25x T=0.1nm

Table 3.2: The multilayer structure of GaAs/Superlattice (GaAs/AlAs) QD. The highlighted parameters are summarized in Table 3.2b.A summary of different values of highlighted parameters of Table 3.2a for different samples.

the AlGaAs deposition. To avoid such a segregation, we replace the ternary AlGaAs barrier with binary materials such as GaAs/AlAs superlattice or pure AlAs. In Table 3.2a, the multilayer structure of GaAs/Superlattice (GaAs/AlAs) QD is shown and the corresponding values of highlighted parameters are summarized in Table 3.2b for different samples. The last sample studied in this article is GaAs/AlAs QD with the epitaxial growth structure summarized in Table 3.3.

Table 3.3 GaAs/AlAs				
#	**Layer**	**Material**	**Al Concentration (%)**	**Thickness (nm)**
1	Buffer	GaAs		60
2	Etch Stop	AlAs		40
3	Contact	GaAs		100
4	Barrier1	$Al_xGa_{1-x}As$	55	70
5	Barrier2	$Al_xGa_{1-x}As$	45	90
6	AlAs	AlAs		10
7	QD	GaAs		1
8	AlAs	AlAs		10
9	Barrier1	$Al_xGa_{1-x}As$	45	60
10	Barrier2	$Al_xGa_{1-x}As$	55	70
11	Cap	GaAs		1

Table 3.3: The multilayer structure of GaAs/AlAs QD.

3.3 Experimental Conditions

The micro-photoluminescence spectra were recorded at cryogenic temperatures $\sim$ 10K in a helium closed cycle cryostat under 635nm continuous-wave laser excitation. The QD was excited using a NA=0.42 microscope objective. The emission was in general collected in a backscattering configuration. The resonant TPE has been performed using a 0.81 NA objective and a tunable pulsed Ti:sapphire laser with 80 MHz repetition rate and a spectral width reduced to approximately 0.1nm by means of a 4f pulse shaper. The laser light reflected by the sample was removed using two volume Bragg grating notch filters with a bandwidth of 0.4nm. Intensity autocorrelation measurements were collected in a Hanbury Brown–Twiss setup equipped with a pair of single photon counting detectors with 65% nominal efficiency and a time resolution of approximately 400ps. Instead, for time-resolved photoluminescence, a silicon avalanche photodiode with a time jittering slightly

below 200ps was employed.

As the emission intensity of as-grown GaAs QD is weak due to multiple internal reflections impeding light extraction, a standard post-growth processing (wet back-etching) was applied to boost the light extraction efficiency. Depending on a sample, a typical light collection efficiency of a few percent at the first lens of the set-up was obtained.

The FSS was obtained with the optical setup configuration as described in subsection 1.4.2. Polarization resolved spectroscopy was done for a series of ≈ 30 QDs on each sample and averages were taken over the collected data with standard deviations indicated in plots in subsection 3.4.2.

3.4 Experimental Results

In this section, we will discuss the experimental results we achieved for spectral uniformity of excitonic complex, FSS correction, polarization-entanglement distribution and two-photon resonant excitation (TPE) respectively.

3.4.1 Spectral Uniformity of Excitonic Complex

As summarized in Table 3.1-Table 3.3, different samples with different configurations were studied. The statistics build upon these are summarized in the following. In Figure 3.4a the distribution of binding energy ΔE_{XX} for different QD thicknesses and Al content in $Al_xGa_{1-x}As$ barrier is plotted vs exciton energy. By observing this plot, a clear uniformity in the binding energy of different samples is indicated. As an other indication, in Figure 3.4b, the X vs XX energy is showing a linear relation between the exciton and biexciton transitions indicating a relatively constant value for binding energy for individual samples (we caution the reader that scatter points are not actually sitting perfectly on a line; they appear so rather as an artefact

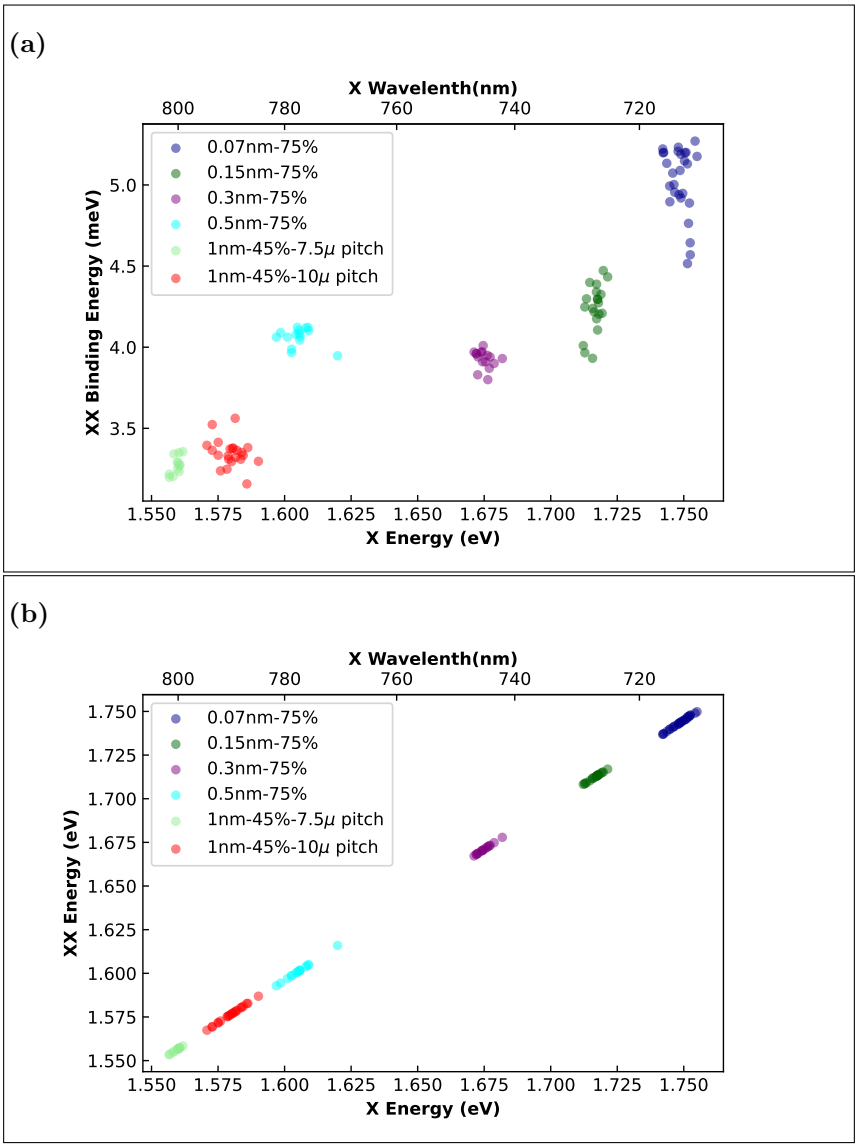


Figure 3.4: Distribution of Binding Energy for different samples. In plot legends the numbers are QD thickness and Al content in the $Al_xGa_{1-x}As$ barrier.**(a)** The scatter distribution of Binding energy for selected different QD thicknesses and Al contents.**(b)** the XX vs X transitions in selected cases showing a well linear relation

from scaling when plotting X energy vs XX). As it can be seen from both plots, the QD emission energy (wavelength) is increased (blue shifted) by decreasing the QD nominal thickness and increasing the AL content in $Al_xGa_{1-x}As$ barrier. By

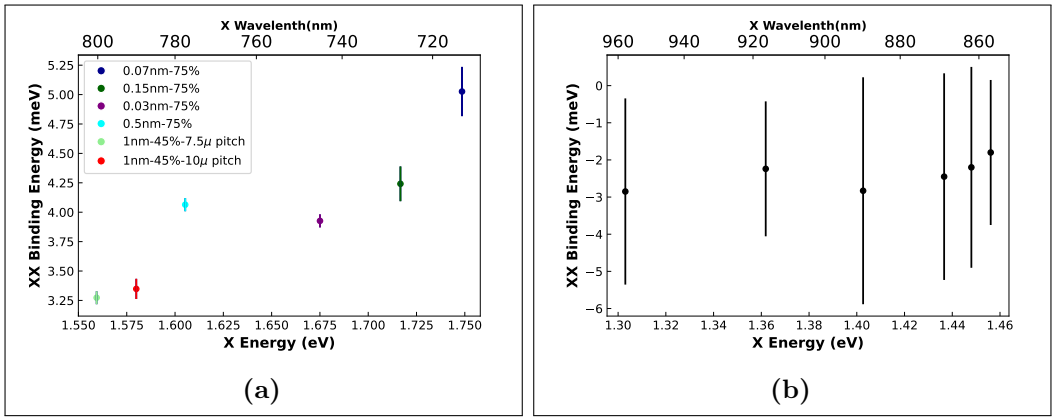


Figure 3.5: Distribution of Binding Energy for different samples. In plot legend the numbers are QD thickness and Al content in the $Al_xGa_{1-x}As$ barrier.**(a)** Distribution of averaged binding energy for different QD thicknesses and Al contents.**(b)** Distribution of binding $In_xGa_{1-x}As$ QDs counterpart. By comparing the standard deviations, GaAs are more uniform than InGaAs QDs.

increasing the Al, one moves from GaAs to AlAs which makes a higher bandgap energy. This is in agreement with the observation of QD blue shifting. This uniformity is in variance to their $In_xGa_{1-x}As$ QD counterparts where, although a remarkable spectral uniformity of the neutral exciton state of large pitch pyramids (7.5 to 12.5μm) is observed, the biexciton binding energy fluctuates individually in respect to the exciton emission line. The biexciton binding energy ΔE_{xx} fluctuates independently from the excitonic line position within the values of the distribution with a full-width half-maximum (FWHMΔE_{xx}) of 2.4meV or more. This is shown in Figure 3.5 where the error bars are the standard deviations from the average value of binding energy for GaAs (Figure 3.5a) and $In_xGa_{1-x}As$ (Figure 3.5b) QDs respectively.

3.4.2 Fine Structure Splitting Correction

As we discuss below, the QD symmetry optimization approaches are essential to ensure high quality of entanglement. The resonant TPE scheme was effective in

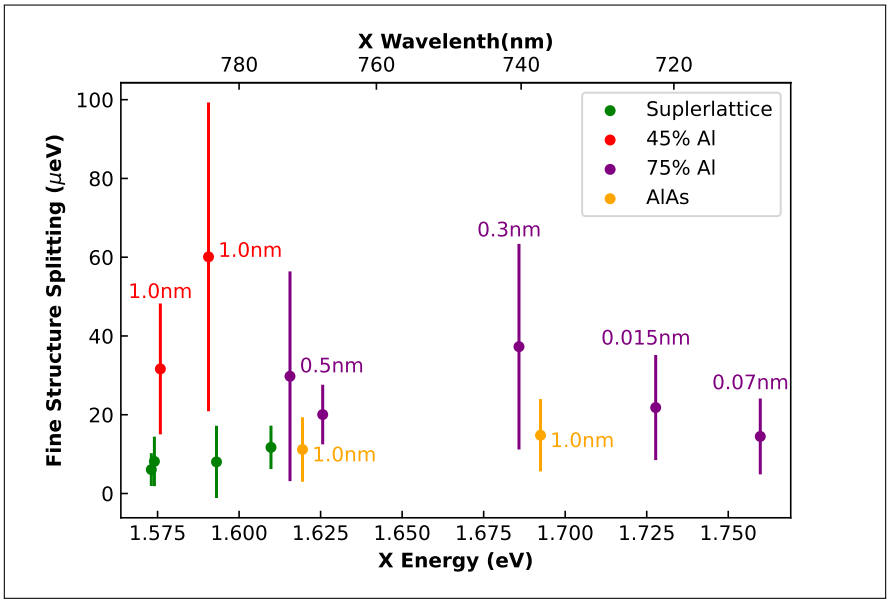


Figure 3.6: Average fine-structure splitting of GaAs QDs with different designs: nominal thickness and/or confinement barrier type. See Figure 3.3 and tables with the summary of the full epitaxial structure in Table 3.1-Table 3.3. Percentages in the legend refer to the AlGaAs nominal barrier Al content.

a majority of tested QDs from the specific studied sample; however, in none of the cases, we could measure polarization entanglement between the biexciton and exciton due to a non-vanishing FSS. Such a broad distribution of large FSS values isat odds with the generally accepted picture of (111) oriented QDs as intrinsically highly symmetric [15]. By several different QD fabrication approaches, it was demonstrated that (111) oriented QDs indeed have smaller FSS values [12, 16, 17] than conventional Stranski-Krastanov QDs, but they rarely all have sufficiently small FSS values for an efficient bright entangled photon emission. For example, in our state-of the-art result, samples with an average exciton FSS equal to ≈3 μeV, can be recreated only in a narrow emission energy range of ≈ 25 meV [18]. Several internal and external perturbations are possibly affecting the symmetry of carrier confinement potential. As previously mentioned, VQWr is presumably among the most dominant one.

As discussed in Table 3.1-Table 3.3, we used three main approaches to reduce the FSS. First, increasing the AL content in $Al_xGa_{1-x}As$ barrier. QDs with pure AlAs confinement barriers (only 10 nm thick in these samples on top of an AlGaAs barrier) had the smallest FSS with an average value of 11±8 μeV—a reduction that we attribute to reduced alloy disorder effects. Indeed, in AlAs barriers, alloy disorder should be absent; thus, the residual FSS is most likely caused by a different phenomenon, while we cannot exclude that thicker AlAs layers would help more. It is also highly possible that small structural asymmetries are more effective due to a smaller QD base. However, without the QD morphological characterization, this statement is speculative at this stage.

Second, we systematically altered the QD thickness (nominally 0.035–0.5nm) confined by $Al_{0.75}Ga_{0.25}As$ barriers ($\approx Al_{0.26}Ga_{0.74}As$ in a VQWr). We observed the FSS and its distribution reduction trend within thinner QDs (Fig. 3). QDs with a nominal thickness of 0.07nm were characterized by an average FSS of 14±10 μeV. A very similar trend has been observed within the $In_{0.25}Ga_{0.75}As$ QD counterparts, where the most symmetric QDs were the thinnest with the ground states approaching the top of the confinement barriers. Carrier wavefunctions' leakage to the barriers, which reduces electron-hole exchange interaction and thus fine-structure splitting could explain the observed FSS reduction trends. We do not show results from the thinnest 0.035nm QDs as we could not identify X and XX transitions due to a very weak or absent intensity of the biexciton and actually a small FSS of all the observed peaks.

Finally, we adopted a third, and the most promising, strategy—a QD confinement by GaAs/AlAs superlattices. 20 periods of nominal 0.1 or 0.2 nm thickness were grown on both sides of a QD. The aim of introducing a digital alloy superlattice was to minimize alloy disorder effects (without expecting any zeroing obviously in view of always present interface disorder effects) occurring within the conventional

$Al_xGa_{1-x}As$. Such a digital alloy superlattice of GaAs/AlAs is expected to act as an effective $Al_{0.5}Ga_{0.5}As$ barrier providing confinement for a QD, however, without alloy disorder effects. By introducing this design, we systematically could reduce the FSS values below 15 μeV, with the best average value of 6±4 μeV in QDs with 0.85 nm as nominal thickness. In Figure 3.6 the resulting FSS values are indicated.

3.4.3 Polarization-Entanglement Distribution

Quantum entanglement of the polarization states of an exciton and biexciton has been demonstrated using a 0.85 nm thickness GaAs QD confined by 0.2 nm period AlAs/GaAs superlattice. This sample had an average FSS value of 6±4 μeV. The spectrum of a representative QD is shown in Figure 3.7a The measured FSS value was <1 μeV as depicted in Figure 3.7b The data were collected under non-resonant excitation conditions.

We used fidelity to the expected maximally entangled state, i.e. the Bell's state $|\psi\rangle = \frac{1}{\sqrt{2}}(|HH\rangle + |VV\rangle)$, as a figure of merit to evaluate the entanglement. 6 curves in total in linear, diagonal and circular bases were taken. See Figure 3.8. Characteristic correlations between linearly co-polarized and anticorrelation between circularly polarized photons were observed. Each curve was integrated for 10 mins. Raw counts of $g^{(2)}(0)$ peak integrated in the range of ±2.5 ns were used (given in the graphs) to calculate the fidelity. The obtained value of 0.59±0.1 exceeds the classical limit of 0.5 clearly indicating non-classical correlations.

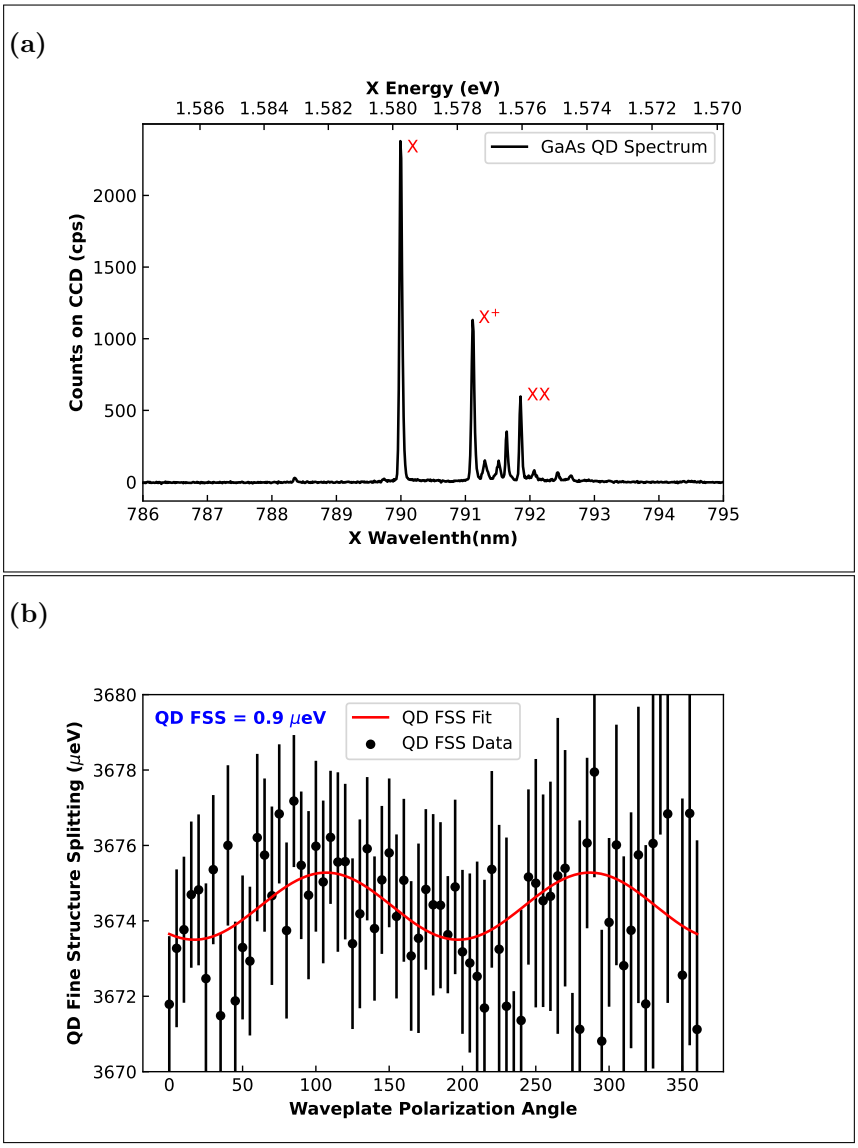


Figure 3.7: **(a)** The spectrum of the QD upon which the polarization entanglement was measured.**(b)** The measured FSS for the QD representative for entanglement measurements.

3.4.4 Two-Photon Resonant Excitation (TPE)

The characteristic uniform energetic order of the excitonic spectral features, specifically a binding biexciton ($E_X > E_{XX}$), was found to be especially advantageous. A few meV binding energy ($\Delta E_{XX} = E_{XX} - E_X$) allowed a relatively easy implemen-

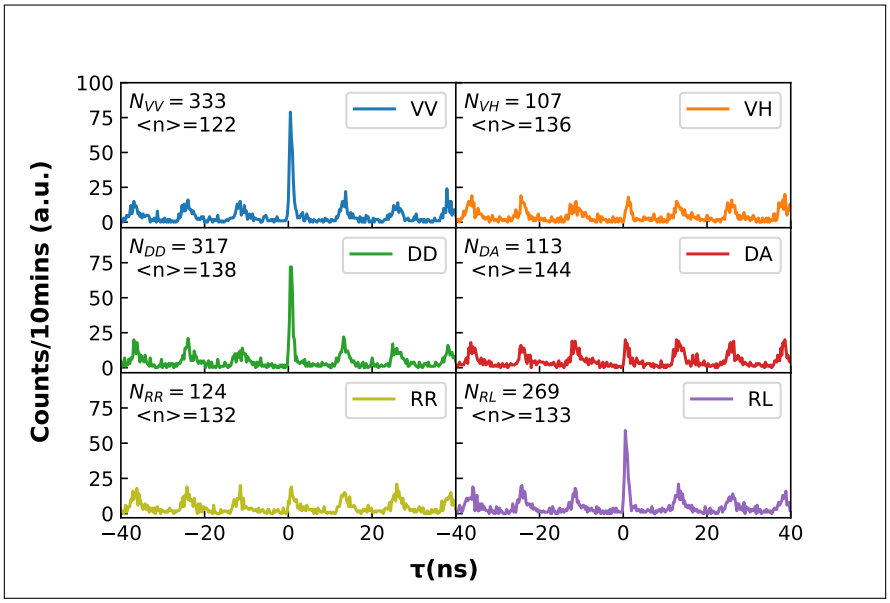


Figure 3.8: Six curves in linear, diagonal and circular bases were taken. As we can see, correlations between linearly co-polarized and anti-correlations between circularly polarized photons are observed.

tation of a resonant two-photon excitation of the biexciton state. The spectrum of a representative GaAs/$Al_{0.45}Ga_{0.55}As$ QD under non-resonant continuous-wave 633nm excitation is shown in the top graph of Figure 3.9a. The presence of other transitions than the exciton and biexciton and a typically low intensity of the biexciton line are strong drawbacks degrading the performance of a deterministic entangled photon source. Under resonant TPE excitation (Figure 3.9a, bottom graph), the QD is effectively coherently addressed, resulting in an emission originating mostly from the biexciton recombination cascade. A low intensity transition close to XX is attributed to one of the charged complexes—as a result of a random QD charging from the vicinity. The coherent nature of the excitation process is well represented by Rabi oscillations of both, the exciton and biexciton, up to a pulse area of 7π (Figure 3.9b). Figure 3.9c shows an autocorrelation curve of the X transition. The calculated $g^{(2)}(0)$ value of 0.028 ± 0.003 ($\pm$3ns range) confirms single photon emission. Figure 3.9d shows the obtained lifetime decays

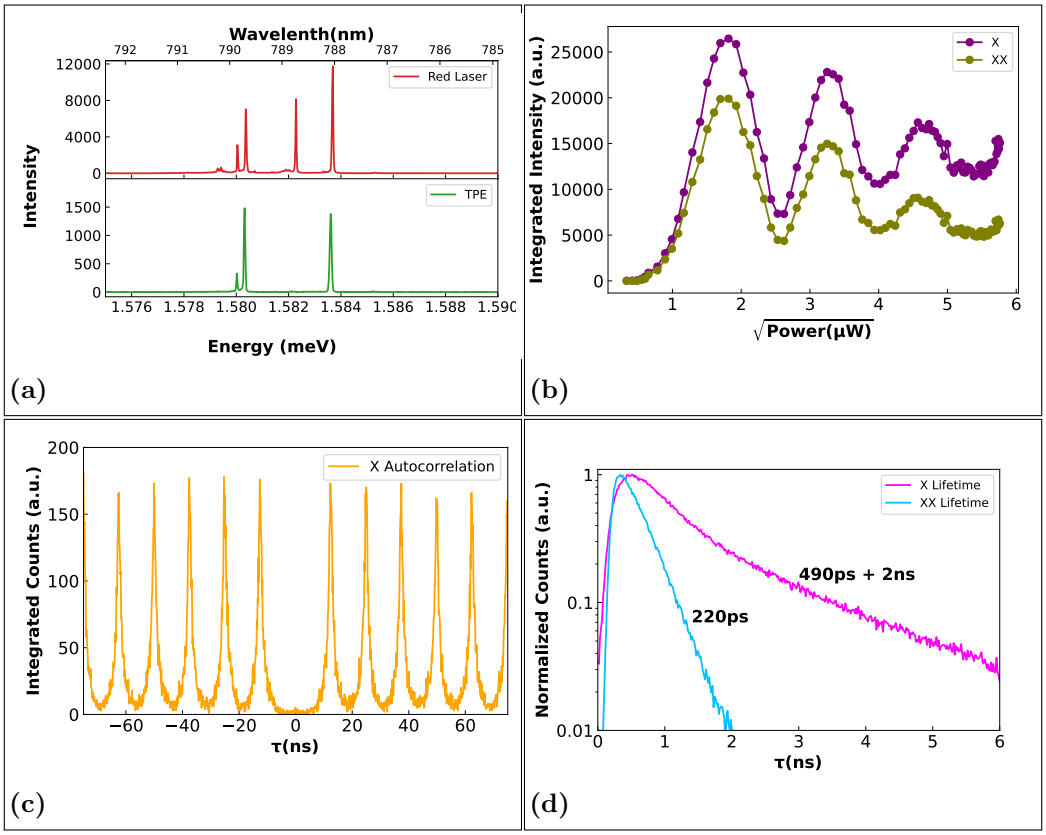


Figure 3.9: **(a)** Spectra of a GaAs/$Al_{0.45}Ga_{0.55}As$ QD under non-resonant (top) and resonant (bottom) excitation.**(b)** Rabi oscillations.**(c)** An auto-correlation curve of the X transition demonstrating single photon emission with $g^{(2)}(0) = 0.028 \pm 0.003$ ($\pm$3ns range).**(d)** The lifetime decays of the exciton and biexciton.

of the exciton and biexciton. The XX lifetime was found to be 220 ps. The X kinetics was found to be more complicated—a biexponential decay with the lifetime constants of 490ps and 2ns. Similarly, slow recombination dynamics related to the effects of a solid-state environment that resemble a well-known QD blinking mechanism has been observed from GaAs QDs [19]. While the origin of the slow decay is not clear and cannot be explained at this stage by a simple on/off QD blinking model, we would like to stress that the presented results nicely serve as a-proof-of-principle demonstrating the possibility to populate the biexciton state

by the resonant TPE and overcome issues arising in the counterpart $In_{0.25}Ga_{0.75}As$ QDs due to an antibinding biexciton.

3.5 Summary and Conclusions

In summary, we have presented a design and systematic study of GaAs site-controlled pyramidal QDs possessing properties highly promising for advanced quantum optics applications. A remarkable state-of-the-art spectral (excitonic pattern) uniformity between individual QDs has been demonstrated as a signature of the overall morphological uniformity. The characteristic feature, a binding biexciton, of all GaAs QDs was found to be advantageous to overcome complications related to an antibinding biexciton in the counterpart $In_{0.25}Ga_{0.75}As$ QDs for resonant two-photon excitation of the biexciton state. Such TPE ability has been demonstrated. We presented several routes to minimize the fine-structure splitting in the QDs. The approach based on a GaAs/AlAs digital alloy superlattice as the confinement barrier was found to be the most promising one even if more work is needed to further reduce the residual FSS.

Bibliography

[1] D. Huber, M. Reindl, S. F. Covre da Silva, C. Schimpf, J. Martín-Sánchez, H. Huang, G. Piredda, J. Edlinger, A. Rastelli, and R. Trotta, "Strain-tunable gaas quantum dot: A nearly dephasing-free source of entangled photon pairs on demand," *Phys. Rev. Lett.*, vol. 121, p. 033902, Jul 2018.

[2] M. Müller, S. Bounouar, K. D. Jöns, M. Glässl, and P. Michler, "On-demand generation of indistinguishable polarization-entangled photon pairs," *Nature Photonics*, vol. 8, pp. 224–228, Mar. 2014.

[3] D. Huber, M. Reindl, Y. Huo, H. Huang, J. S. Wildmann, O. G. Schmidt, A. Rastelli, and R. Trotta, "Highly indistinguishable and strongly entangled photons from symmetric GaAs quantum dots," *Nature Communications*, vol. 8, p. 15506, Aug. 2017.

[4] F. Basso Basset, S. Bietti, M. Reindl, L. Esposito, A. Fedorov, D. Huber, A. Rastelli, E. Bonera, R. Trotta, and S. Sanguinetti, "High-yield fabrication of entangled photon emitters for hybrid quantum networking using high-temperature droplet epitaxy," *Nano Letters*, vol. 18, no. 1, pp. 505–512, 2018. PMID: 29239186.

[5] F. Basso Basset, M. B. Rota, C. Schimpf, D. Tedeschi, K. D. Zeuner, S. F. Covre da Silva, M. Reindl, V. Zwiller, K. D. Jöns, A. Rastelli, and R. Trotta, "Entanglement swapping with photons generated on demand by a quantum dot," *Phys. Rev. Lett.*, vol. 123, p. 160501, Oct 2019.

[6] M. Reindl, D. Huber, C. Schimpf, S. F. C. da Silva, M. B. Rota, H. Huang, V. Zwiller, K. D. Jöns, A. Rastelli, and R. Trotta, "All-photonic quantum teleportation using on-demand solid-state quantum emitters," *Science Advances*, vol. 4, no. 12, p. eaau1255, 2018.

[7] M. Gurioli, Z. Wang, A. Rastelli, T. Kuroda, and S. Sanguinetti, "Droplet epitaxy of semiconductor nanostructures for quantum photonic devices," *Nature Materials*, vol. 18, no. 8, p. 799–810, 2019.

[8] E. Schöll, L. Hanschke, L. Schweickert, K. D. Zeuner, M. Reindl, S. F. Covre da Silva, T. Lettner, R. Trotta, J. J. Finley, K. Müller, A. Rastelli, V. Zwiller, and K. D. Jöns, "Resonance fluorescence of gaas quantum dots with near-unity photon indistinguishability," *Nano Letters*, vol. 19, no. 4, pp. 2404–2410, 2019.

[9] N. Akopian, N. H. Lindner, E. Poem, Y. Berlatzky, J. Avron, D. Gershoni, B. D. Gerardot, and P. M. Petroff, "Entangled photon pairs from semiconductor quantum dots," *Phys. Rev. Lett.*, vol. 96, p. 130501, Apr 2006.

[10] J. Liu, R. Su, Y. Wei, B. Yao, S. F. Silva, Y. Yu, J. Iles-Smith, K. Srinivasan, A. Rastelli, J. Li, and et al., "A solid-state source of strongly entangled photon pairs with high brightness and indistinguishability," *Nature Nanotechnology*, vol. 14, no. 6, p. 586–593, 2019.

[11] M. Reindl, K. D. Jöns, D. Huber, C. Schimpf, Y. Huo, V. Zwiller, A. Rastelli, and R. Trotta, "Phonon-assisted two-photon interference from remote quantum emitters," *Nano Letters*, vol. 17, no. 7, pp. 4090–4095, 2017. PMID: 28557459.

[12] G. Juska, V. Dimastrodonato, L. O. Mereni, A. Gocalinska, and E. Pelucchi, "Towards quantum-dot arrays of entangled photon emitters," *Nature Photonics*, vol. 7, pp. 527–531, July 2013.

[13] V. Dimastrodonato, E. Pelucchi, and D. D. Vvedensky, "Self-limiting evolution of seeded quantum wires and dots on patterned substrates," *Phys. Rev. Lett.*, vol. 108, p. 256102, Jun 2012.

[14] K. Holsgrove, T. O'Reilly, S. Varo, A. Gocalinska, G. Juska, D. Kepaptsoglou, E. Pelucchi, and M. Arredondo, "Towards 3d characterisation of site-controlled ingaas pyramidal qds at the nanoscale," *Journal of Materials Science*, Aug. 2022.

[15] A. Schliwa, M. Winkelnkemper, A. Lochmann, E. Stock, and D. Bimberg, "In(ga)as/gaas quantum dots grown on a (111) surface as ideal sources of entangled photon pairs," *Phys. Rev. B*, vol. 80, p. 161307, Oct 2009.

[16] T. Kuroda, T. Mano, N. Ha, H. Nakajima, H. Kumano, B. Urbaszek, M. Jo, M. Abbarchi, Y. Sakuma, K. Sakoda, I. Suemune, X. Marie, and T. Amand, "Symmetric quantum dots as efficient sources of highly entangled photons: Violation of bell's inequality without spectral and temporal filtering," *Phys. Rev. B*, vol. 88, p. 041306, Jul 2013.

[17] M. A. M. Versteegh, M. E. Reimer, K. D. Jöns, D. Dalacu, P. J. Poole, A. Gulinatti, A. Giudice, and V. Zwiller, "Observation of strongly entangled photon pairs from a nanowire quantum dot," *Nature Communications*, vol. 5, p. 5298, Dec. 2014.

[18] G. Juska, E. Murray, V. Dimastrodonato, T. H. Chung, S. T. Moroni, A. Gocalinska, and E. Pelucchi, "Conditions for entangled photon emission from (111)b site-controlled pyramidal quantum dots," *Journal of Applied Physics*, vol. 117, no. 13, p. 134302, 2015.

[19] J.-P. Jahn, M. Munsch, L. Béguin, A. V. Kuhlmann, M. Renggli, Y. Huo, F. Ding, R. Trotta, M. Reindl, O. G. Schmidt, A. Rastelli, P. Treutlein, and

R. J. Warburton, "An artificial rb atom in a semiconductor with lifetime-limited linewidth," *Phys. Rev. B*, vol. 92, p. 245439, Dec 2015.

University College Cork, Ireland
Coláiste na hOllscoile Corcaigh

CORA
Cork Open Research Archive
Cartlann Taighde Oscailte Chorcaí

Ranjbar Jahromi, I. 2023. Evaluation and properties of site-controlled pyramidal quantum dots for quantum information processing. PhD Thesis, University College Cork.

Please note that Chapter 4 (pp. 93-116) is unavailable due to a request by the author.

CORA Cork Open Research Archive http://cora.ucc.ie

Chapter 5

Summary and Conclusions

5.1 Summary

In summary, in this PhD work, we studied and evaluated properties of a special family of QDs for quantum information processing.

In the first chapter (chapter 1), we briefed basic ideas behind quantum information, the essence of quantum information processing and it's potential superiority to classical information processing. Then we took photons as the candidate for carrying quantum information. Different polarization entangled photon and single photon sources were discussed. A special type of this sources are semiconductor QDs. We reviewed the challenges arising during the implementation of such sources. We finally explained the "*Site-Controlled Pyramidal QDs*" as a unique type of QDs that we work on in our EPN group at Tyndall National Institute.

In the following chapters, we started evaluating specific configurations of site-

controlled QDs. In chapter 2, we studied InGaAs/GaAs QDs. We showed that resonant initialization of such sources is possible although possessing an anti-binding biexcitonic complex. We explained the reason for the TPE not being efficient as the anti-binding nature leads to phonon-assisted recombination of the X states. This phenomenon limits the biexciton recombination rate. We demonstrated the presence of entanglement in the resonantly excited QD.

In the third chapter (chapter 3), we systematically studied a new generation of site controlled QDs that has been left untackled for a long time. In this study, the GaAs/AlGaAs QDs were studied. The FSS is a detrimental factor to the quality of entanglement. Different strategies was implemented to reduce the FSS. From changing the alloy composition and QD thickness to the structure design such as using superlattice structure to isolate the QDs from the Ga enriched structures (VQWr) acting as the extra charge feed to the QD and breaking the symmetry of the confining potential of QDs. We showed that due to its binding excitonic nature, it is more responsive (compared to InGaAs anti-binding QDs) under the TPE excitation scheme.

In chapter 4, charging of QDs was studied. The goal is to leave the QD neutral with only two distinct transitions X and XX. Doping the vicinity of QD with iron was selected to be the main strategy. That is because Iron historically is chosen as a dopant making defects that act as charge traps. We showed that the iron doping could actually enhance QD neutralization. This method was selected as growth related strategy for charge correction. An other approach was post-growth which the sample was put on a PMN-PT piezo crystal. An applied voltage was translated to mechanical strain on the QD crystal structure, via the piezo crystal, which could significantly alter the charging of the QD. As a result, we demonstrated that in both strategies (Iron doping and external strain), by suppressing the positive trion transition, the superlattice QD was responsive under TPE scheme. Resonant

excitation of superlattice QDs had failed prior to any of these methods.

5.2 Future Works

Although a tremendous amount of work has been performed on site-controlled pyramidal QDs (Sc-PQDs) over the last 20 years, there is a need to further improve their performances, and there are many opportunities available for further enhancement of this unique system. In general all QD systems presently investigated are still not mature enough, as a technology, to be inserted at scale into photonic structures capable of quantum computation. Small demonstrators exist, but we are still far from the level of quality and reproducibility needed for practical applications. Nevertheless progress has been impressive, and the scientific community is constantly surprising the pessimists. Specifically for PQDs, below are some of the area for improvement to name an important few:

Enhanced Coherence and Stability: Future research can focus on improving the coherence and stability of SC-PQDs. This involves investigating strategies to minimize decoherence mechanisms, such as phonon interactions and charge fluctuations. Techniques like strain engineering, interface modifications, and encapsulation/surface passivation can be explored to enhance coherence times and stability, making SC-PQDs more suitable for quantum information applications.

Scalable Fabrication Techniques: To realize large-scale quantum information processing systems, scalable fabrication techniques for SC-PQDs are essential. Future works can explore innovative approaches to efficiently produce arrays of SC-PQDs with higher uniformity and controlled positioning. Techniques like advanced lithography and advanced pattern (template)-assisted growth (e.g. where the pattern geometry is used to influence the epitaxial outcome quality and uniformity) can be investigated to achieve high-throughput fabrication of SC-PQD arrays.

Integration with Photonic Structures: Integrating SC-PQDs with photonic structures is crucial for efficient light-matter interactions and information transfer. Future research can focus on developing techniques for precisely coupling SC-PQDs with waveguides, microcavities, and photonic circuits. This integration will enable enhanced photon extraction efficiency, controlled photon emission properties, and on-chip manipulation of quantum information.

Cluster States: SC-PQDs can be integrated into a larger system to contribute to the creation of cluster states. In general, by using SC-PQDs as individual qubits and controlling their interactions and entanglement with neighboring qubits, it is possible to build up the desired cluster state. The controlled positioning of SC-PQDs allows for precise arrangement and connectivity of qubits, which is crucial for constructing the required entanglement pattern. Moreover, PWQDs have a unique control of QD formation, and growth and control of pure molecular states are possible, including special designs with common excited state between two separated dots as required by some proposals in the literature [1]. This is a rather unique property of PQDs compared to other self-assembled systems, and will be investigated.

It's worth noting that the specific implementation of SC-PQDs for cluster state quantum computing would require additional considerations and techniques to ensure the necessary entanglement generation, gate operations, and measurements. However, the controlled positioning and tailored properties of SC-PQDs make them a promising candidate for contributing to the creation of cluster states in certain quantum computing architectures.

Quantum Dot Entanglement: Future works can explore methods to create more entangled state versions using SC-PQDs. Investigating entanglement generation between multiple SC-PQDs and exploring entanglement swapping techniques can pave the way for scalable quantum networks and will find applications to

quantum information processing and quantum internet. This research can lead to the development of entangled photon sources based on SC-PQDs, enabling long-distance quantum communication and quantum teleportation.

Quantum Dot Quantum Repeaters: Closely linked to the entanglement swapping paragraph, quantum dot quantum repeaters hold promise for long-distance quantum communication. Future research can explore the feasibility of using SC-PQDs as building blocks for quantum repeater nodes. Investigating techniques to extend the coherence and entanglement distribution over long distances

Quantum Dot Spin Qubits: Exploring the potential of SC-PQDs for spin qubits is another exciting avenue for future research, which has been till now been left untouched. Investigating the coherence properties and manipulation techniques of spin states in SC-PQDs can lead to the realization of robust spin qubits. This research can contribute to the development of solid-state spin-based quantum computing architectures, leveraging the advantages of SC-PQDs, such as controlled positioning and scalability.

Hybrid Quantum Systems: Integrating SC-PQDs with other quantum systems, such as superconducting qubits or atomic systems, offers opportunities for hybrid quantum systems. Future research could focus on exotic hybridizing SC-PQDs with complementary quantum technologies to harness the strengths of each system. This can lead to enhanced quantum coherence, novel quantum operations, and the exploration of new quantum phenomena.

Error Correction and Fault-Tolerant Quantum Computing: All the mentioned development will go in parallel to other technological developments linked to full operating systems. Future works can address the challenges of error correction and fault-tolerant quantum computing when SC-PQDs are involved. Investigating error detection and correction codes specifically tailored for SC-PQDs can improve the reliability and fault tolerance of quantum information processing

systems. Developing robust error mitigation techniques, such as quantum error correction protocols and error-protected gates, will be crucial for realizing fault-tolerant quantum computing with SC-PQDs.

Bibliography

[1] S. E. Economou, N. Lindner, and T. Rudolph, "Optically generated 2-dimensional photonic cluster state from coupled quantum dots," *Phys. Rev. Lett.*, vol. 105, p. 093601, Aug 2010.